STRESS INTENSITY SOLUTIONS OF THERMALLY INDUCED CRACKS IN A COMBUSTOR LINER HOT SPOT USING FINITE ELEMENT ANALYSIS

A Dissertation
Presented to
The Academic Faculty

by

Donald W. Rhymer

In Partial Fulfillment
of the Requirements for the Degree
Doctor of Philosophy in the
School of Mechanical Engineering

Georgia Institute of Technology
December 2005

STRESS INTENSITY SOLUTIONS OF THERMALLY INDUCED CRACKS IN A COMBUSTOR LINER HOT SPOT USING FINITE ELEMENT ANALYSIS

Approved by:

Dr. W. Steven Johnson, Advisor
School of Mechanical Engineering
Georgia Institute of Technology

Dr. Rami Haj-Ali
School of Civil and Environmental Engineering
Georgia Institute of Technology

Dr. Richard W. Neu
School of Mechanical Engineering
Georgia Institute of Technology

Dr. Lawrence M. Butkus, LtCol, USAF
Engineering Directorate / Flight Systems Engineering Division
Aeronautical Systems Center, WPAFB, OH

Dr. Min Zhou
School of Mechanical Engineering
Georgia Institute of Technology

Date Approved: October 13, 2005

To my two children, Jared and Helen, who were both born while working on this dissertation, and to my lovely and faithful wife, Dawn. Seeing each of you smile when I came home each day were gifts of the Lord.

ACKNOWLEDGEMENTS

"For from Him and to Him and through Him are all things. To Him be the glory forever. Amen." Romans 11: 36 This verse closes one of the greatest treatises of truth found in Scripture, and the Apostle Paul gives appropriate credit. We are all, on our best days, but stewards of what the Almighty has given. For me not to thank Him, who saved me and sent His Son for me, would not only be foolish, but inaccurate. SOLI DEO GLORIA

I wish to thank my dear wife, Dawn. Though she doesn't regret a day of it, she gave up the potential to work on her own career in order to help me raise a family. Any wife that stays at home to care for, nurture, and guide children fulfills one of the highest callings to society and the Lord. She had the more draining, albeit more rewarding, day-to-day walk of this assignment.

Dr. Steve Johnson is not only renown for his work in mechanics of materials research, but I have found him to be one of the best in preparing students to improve both their oral and written communication. So besides his faithful support, guidance, and friendship, I owe a great deal to his perseverance in helping me "just say it!"

This work was done in cooperation with both Pratt & Whitney Company (contract no. 20195) and the Air Force Research Lab (contract no. FA 8650-04-C5202). The technical monitors for the Pratt & Whitney contract were Rick Pettit and Ripudaman Singh and they have been great guides and sounding boards for this work and deserve many thanks. Also at Pratt & Whitney, Keith Kersey, Jim Dierberger, and Gerald Kulhowvick, have given me very important support in blister testing, background information, and ANSYS help, respectively.

The technical monitor of the Air Force Research Lab contract was Dr. Jeff Calcaterra. In this work, fellow graduate student Mike Solimando was helpful in conducting experimental testing.

Doctoral candidate Ryan Krauss will one day, I'm sure, lead research in structural dynamics; but until then his resume at least includes 1) great qualifying exam study partner and 2) even better prayer and accountability partner..

Lt.Col. Larry Butkus has been, not only a committee member, but a professional mentor and military model. I join an ever growing group of people in the Air Force, academia, and beyond who respect and admire him.

Shelby Highsmith, Jr. is to be thanked for being a great sounding board for discussing fatigue and fracture mechanics theory. When he does graduate, he will be an asset to the world of mechanics of materials research.

Lastly, to my local family (for now two assignments) the people at Heritage Church, led by Pastors Steve Martin and Hank Rast, have my sincere love and appreciation. They were one of the important reasons why a return to Georgia Tech was not only an option, but a must. Every person, and thus every church, brings their own falleness to the world, and so no church is perfect. However I have never seen biblical Christianity taught and lived better than any local body I've known.

TABLE OF CONTENTS

Page

LIST OF TABLES

Page

LIST OF FIGURES

Page

LIST OF SYMBOLS

a	crack length
da	crack growth increment
da/dN	fatigue crack growth rate per cycle
E	Young's Modulus
K	stress intensity
ΔK	stress intensity range
K_o	initial stress intensity at given crack length
K_{+5}	stress intensity at given crack length after 5 additional cycles
K_c	fracture toughness
K_{eff}	effective stress intensity
K_{th}	stress intensity at threshold
K_{op}	stress intensity when crack is first fully open
N	cycle count
N_f	final number of cycles for fatigue failure
P	load
P_{max}	maximum load
P_{min}	minimum load
ΔP	load range
R	stress ratio
σ	stress
$\Delta\sigma$	stress amplitude

LIST OF ABBREVIATIONS

ASM	American Society of Materials
BFV	ANSYS FEA command “Body Force Volume”
CCI	closed crack integral
CT	compact tension
CTOA	crack tip opening angle
CTOD	crack tip opening displacement
DCCI	decomposed crack closure integral
EPFM	elastic-plastic fracture mechanics
FCG	fatigue crack growth
FEA	finite element analysis
FKN	ANSYS FEA command for contact pair stiffness
FTOLN	ANSYS FEA command for contact gauss pt penetration tolerance
HoST	Hot Section Technology
J	J-integral value
LCF	low cycle fatigue
LEFM	linear elastic fracture mechanics
MCCI	modified crack closure integral
NASA	National Aeronautics and Space Administration
NL GEOM	ANSYS command for “Nonlinear Geometry” effects
SIF	stress intensity factor
SRP	strain range partitioning
TMF	thermomechanical fatigue
TMF-IP	in-phase thermomechanical fatigue

TMF-OP	out-of-phase thermomechanical fatigue
UCCI	unified crack closure integral
VCE	virtual crack extension

SUMMARY

Developing stress intensity solutions for thermal-strain induced cracking in hot spots is the chief goal of this research. Using finite element analysis (FEA) to model the stress state and crack stress intensities resulting from thermal gradients (a.k.a hot spots), a model is needed to represent and predict this cracking and eventual crack arrest in combustor liners in turbine engines. Specifically, this research investigates: 1) the constitutive properties (both temperature and time-dependent properties) of the B-1900+Hf alloy used in the liner, 2) the buckled, out-of-plane response of a thin plate of the material due to build up of thermally induced compressive stresses, 3) the thermal cycling of hot spot that produces a hardening stress field, and 4) the thermally induced crack growth not represented by classic thermo-mechanical fatigue (TMF). The FEA program used to model each of these properties is ANSYS 7.1. Experimental data is used to validate models of each of the areas.

With the max hot spot temperature at 1093° C (2000° F) of a 1.5 mm thick, 82.55 mm diameter circular plate of B-1900+Hf, annular buckling and bending stresses result during each thermal cycle and drive the crack initiation and propagation. A finite element analysis (FEA) model, using ANSYS 7.1, has been developed which models the buckling and bending induced by the gradient and represents the stress intensity at simulated crack lengths across the hot spot upon cool down of each thermal cycle. With the stress intensity values, and using published da/dN vs. K_{eff} data, the number of cycles needed to extend the crack at distinct distances is estimated.

The constitutive and cyclic responses of the model are validated by comparing the out-of-plane displacement over twelve thermal cycles with the same data recorded via a B-1900+Hf specimen thermally cycled using an oxy-propane burner rig. The model approximates the out-of-plane response within 5% error at heat-up after twelve cycles and a difference in the final displacement of 0.185 mm out of 3.4 mm. Furthermore, the number of thermal cycles

modeled for a crack to grow from 5 to 17 mm is compared to the experimental results. In determining the number of cycles until the crack arrests, the model estimates the number of cycles within 5 when compared to the actual 462 experimental cycles run. While the K vs. a curve used for this estimation indicates a relatively high would-be K_{th} value, the model shows that repeated cycles at the same crack length would produce a lower more accurate K level at the length that the crack arrests.

CHAPTER 1: INTRODUCTION

During the life of a turbine engine, the combustor liner, made from the nickel-based superalloy B-1900+Hf, has two main means of keeping cool (below ~ 982 °C / 1800 °F). First, it possesses a ceramic-based thermal barrier coating, designed to dissipate the heat away from the base metal. Second, the liner is perforated with film cooling holes which pull cooling (bypass) air into the liner, thus forming a thin barrier or "film" along the liner walls, further insulating the liner from mainstream heat. Figure 1.1 shows the flow behavior of a typical combustor liner with cooling holes. Both the ceramic coating and the hole-produced cooling film become ineffective at certain locations of the liner where the fuel-oxygen mix becomes excessively rich, creating hotter areas in the mainstream. These hotter regions cause the thermal barrier coating to spall away and the cool film air to "scrub away" and get burned with the mainstream.

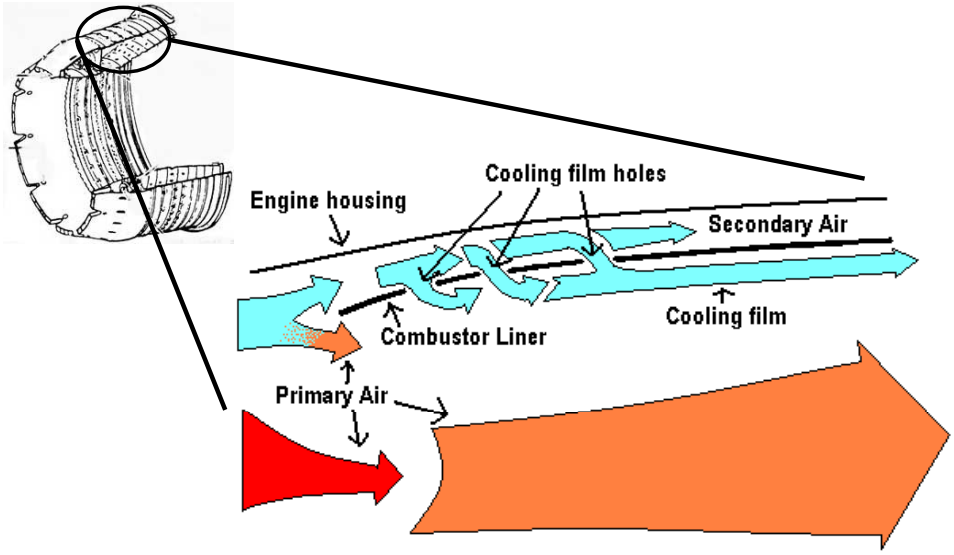

Figure 1.1 Schematic of typical combustor liner with function of cooling holes

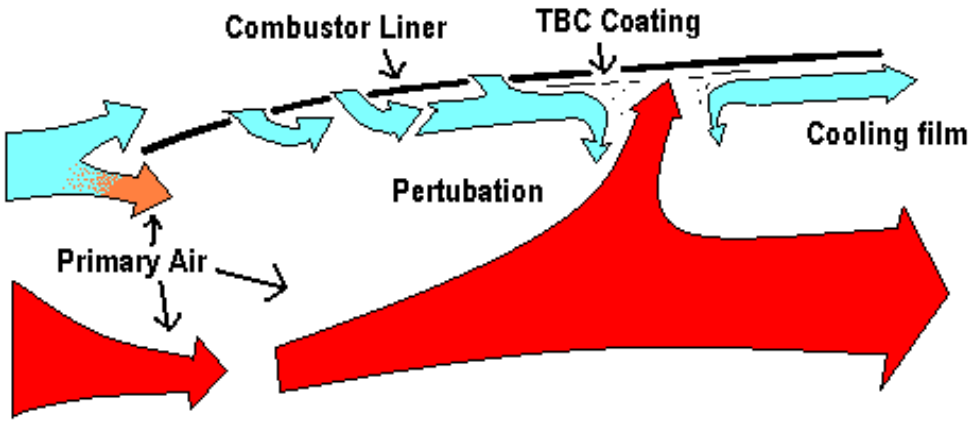

Figure 1.2 Schematic of the development of hot spots in a typical combustor liner caused by airflow perturbations

These conditions result in a much hotter (~1093 °C / 2000 °F) liner wall in certain locations (i.e. “hot spots”). As the liner wall becomes locally hotter than the surrounding metal, extreme thermally induced strains are introduced. With repeated engine firings during its lifetime, thermomechanical fatigue and subsequent thermal cracking results. The crack propagates across the hot spot until it and subsequent branches self-arrest once they reach relatively cooler metal where the thermal gradient dissipates.

Developing stress intensity solutions for thermal-strain induced cracking in these hot spots is the chief goal of this research. How these intensities vary throughout the hot spot as the crack grows will be investigated, specifically with regard to possible crack arrest as the thermal gradient and resulting thermal strains dissipate. Modeling of the stress intensity solutions of the resulting fatigue crack will be performed using the finite element program ANSYS and will include material and structural nonlinearities (plasticity and buckling, respectively).

Quantifying the state of stress and fatigue crack growth in a thermal environment is a complex and challenging problem. Characterizing both, when the thermal environment involves a changing thermal gradient only adds to the

complexity. But this complexity needs to be understood. By accurately assessing the damage state in turbine engines, one can more accurately predict the severity of that damage and thereby develop procedures for repair and replacement at the appropriate time in its life and with more certainty. This more damage tolerant approach makes engines more cost-effective. Current engine specifications require combustor assemblies to be removed based on an overly conservative fatigue life estimate. Existing thermomechanical fatigue (TMF) life approximations using a strain-life methodology are incapable of defining the stress intensity, and much of the current TMF research is too general for thermal gradient applications. Moreover, the nature of a cyclically heated, localized region of higher than average temperatures (i.e. “hot spot”) creates an evolving, hardening yield surface, a transient thermal gradient, time-dependent behavior and thermal strain-induced cracking. As the pursuit for more damage tolerant and temperature resistant aerospace materials continues, non-critical cracking must be permitted but only so far as the nature of damage can be understood. A more detailed, exact analysis is required to characterize the stress intensity caused by a TMF induced crack propagating through a hardening plastic zone and a thermal gradient. An attempt to quantify such results can be modeled using the finite element analysis (FEA) program ANSYS to solve for the stress intensity at the crack tip throughout the hot spot and to a point of likely arrest.

This study will address many issues in order to accurately determine the stress intensity solution for thermal fatigue crack growth in a combustor liner. These issues are:

A. Creation of a constitutive model of B-1900+Hf that can be incorporated into ANSYS, to include both temperature- and time-dependent properties, using test data from published sources.

B. Determining the hardened, yield surface (shakedown) and mechanical response of the combustor liner hot spot before thermal fatigue crack initiation and growth.

C. Develop stress intensity solution for the crack at various locations from the center of and through the hot spot.

D. Predicting fatigue crack growth behavior and a crack length at which arrest is likely.

CHAPTER 2: BACKGROUND AND LITERATURE REVIEW

The primary goal of this investigation is to develop a model that accurately characterizes a crack resulting from the repeated hot spots in a thin plate of nickel-based superalloy. To date, there has not been comprehensive research published in open literature which addresses this specific problem. Despite its complex nature, however, when separating this problem into the general engineering issues that are germane to the application, one can find much published research that is pertinent.

For example, any material undergoing cyclic loading involves fatigue research. When heat is also cyclically applied, the study of both classical thermo-mechanical fatigue (TMF) research as well as thermal fatigue (without mechanically applied loads) is warranted. Hot spots involve a study of the effects of thermal gradients. Any study related to cracking concerns fracture mechanics and fatigue crack growth. Additionally, modeling each of these types of problems with FEA can be a research area itself. So once these contributing subjects have been identified, a survey of the previous research in each of these areas should be done before tackling the more specific problem. What follows is such a survey, to include 1) the foundations of plasticity and hardening in fatigue, 2) thermal fatigue and TMF research, 3) fracture mechanics and fatigue crack growth, and 4) modeling fracture in FEA.

2.1 Fatigue, Plasticity, and Hardening Foundations

Fatigue research is normally classified today by either a lifing approach (estimating the total cycles until fracture of a material for a range of cyclic stresses) or a fatigue crack growth/damage tolerance approach. The roots of lifing date back to the early 1900's, as Basquin[1] determined that the true, elastic stress amplitude ($\Delta\sigma/2$) of fatigue had a linear relationship on a log-log

scale with cycles-to-failure (N_f), thus defining the modern-day S-N curve. However, Basquin's relationship does not accurately quantify fatigue life when the material is cycled beyond the elastic range and plasticity results as it is stress-based. To incorporate a strain-based approach, Coffin [2] and Manson [3], independently of one another, developed a power-law function for plastic strain-life that plasticity in fatigue was characterized. Basquin's and the Coffin-Manson relationships are combined to form the total strain-life equation and are graphically shown in Figure 2.1 as the strain-life curve.

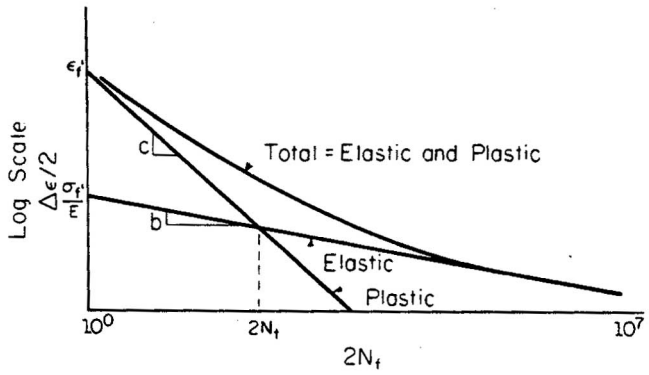

Figure 2.1 Total Strain-life Curve [4]

While this relationship represents the general trend of most metals and is still used as the baseline for strain-life relationships, the study of TMF requires a more detailed analysis of the specific damage mechanisms involved. Additionally, it is important to note that during the low-cycle fatigue (LCF) regime, plasticity is dominant. This determination of the dominant damage mode becomes crucial in determining the subsequent propagation and ultimate failure of the damage. In 1971, Manson, Halford, and Hirschberg [5] proposed strain-range partitioning (SRP) as a means of quantifying the specific damage mechanisms involved in strain-life determination. By assuming that each partition can model a specific damage type with a specific number of life cycles, a Palmgren [6]-Miner [7] type life prediction can be used.

The nature of plasticity and hardening have also been quantified, most notably through the use of the Ramberg-Osgood [8] relationship developed in 1943. Shown in Equation 2.2 in terms of stress, this model accounts for the initial elastic portion of the curve as well as the plastic portion. However quantified, the power law model reflects the typical behavior of most engineering metals under plastic deformation.

[2.1] $$\varepsilon = \frac{\sigma}{E} + H\left(\frac{\sigma}{E}\right)^{n}$$

However, when applied to fatigue, subsequent and cyclic yielding needs to be quantified by any model employed to describe plasticity. This effect has been quantified by one of three main models: isotropic hardening, kinematic hardening, or a combination of both. Both involve what is known as a yield surface. This surface is best described graphically as a circle surrounding the center of a multiaxial stress axis system. The circle indicates the point at which the material yields in any direction. In isotropic hardening, the yield surface "expands" uniformly in each direction, such that there is an ever-increasing yield strength, regardless of strain path. As Hill [9] describes, the yield surface is determined only by the final plastic state, regardless of the strain path. However, this model does not account for the Bauschinger [10] effect, whereby the subsequent reversed loading produces a decrease in absolute yield criteria. Kinematic hardening, suggested by Prager [11] does model this effect as the yield surface "translates" such that any yielding moves the yield surface without changing size or shape in strain space. Figure 2.2 graphically depicts the "movement" of each yield surface in strain space. However, most materials behave as a combination of both.

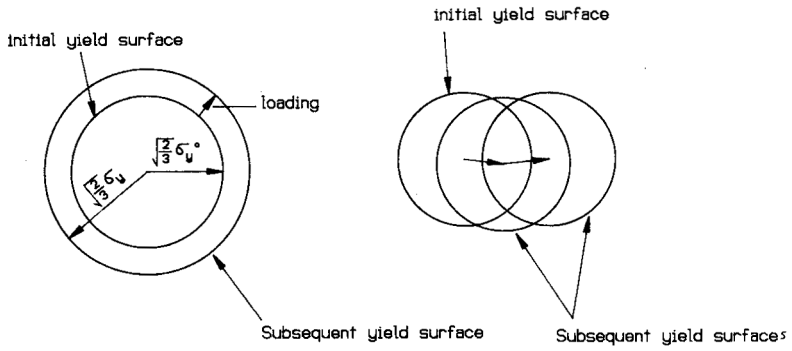

(a) Isotropic Hardening (b) Kinematic Hardening

Figure 2.2 Graphical depictions of Hardening Rules [12]

A two surface model was proposed by Dafalias and Popov [13] in 1976, which incorporated internal state variables of plasticity. The model uses two distinct yield surfaces (the initial yield and the bounding yield surface) and a continuous variation of the plastic modulus between the two. Nonlinear kinematic hardening was taken into account by Armstrong and Frederick [14] as well as Lemaitre and Chaboche [15] whereby Prager's [11] linear model is generalized to the nonlinear case. Most notably, the Chaboche model has been incorporated into ANSYS and ABAQUS finite element programs.

A theory known as endochronic theory was developed by Valanis [16] and further refined by Watanabe and Atluri [17]. This was the first plasticity theory that did not use a yield surface in its development, and proved more accurate for materials without an exactly defined yield stress (or proportional limit). Instead, it focuses on internal variables and irreversible thermodynamics that accompany deformation. A yield surface, however, could be constructed from the results. It should be noted that for each of these models, the validity is restricted to a low number of cycles, not high-cycle fatigue. The current research involves incorporating either kinematic or isotropic hardening with creep behavior in the ANSYS material model.

2.2 Thermal and Thermomechanical Fatigue Research

The study of thermal effects on mechanical behavior dates back to 1838 when J. Duhamel [18] published equations for thermal stresses resulting from non-uniform heating. In 1894, Winkelmann and Schott [19] investigated thermal shock in ceramics, linking thermal stresses to fracture, quantitatively, for the first time. But it wasn't until the 1930's that TMF of ductile engineering materials was documented. In 1935, Schmid and Boas [20] researched thermal strain-induced plasticity in crystals. Just three years later, Bollenrath and coworkers [21] published work on thermal shock in ductile metals. It is important to review the different areas of research accomplished in studying thermal effects on materials since the hot spot temperature can reach 1093 °C.

2.2.1 Classical TMF Research

Since 1935, researchers have been using and modifying many of the models developed by these researchers to predict the behavior of materials under TMF conditions. The nature of high temperature, strain-induced plasticity resulting in FCG, while being complex, has spawned many avenues of research to isolate, quantify, and ultimately predict TMF damage. Millenson and Manson [22] explained the cause of thermally induced cracking in welded turbine wheels as resulting from cyclic plastic strains. One modern area of research has been focused on the microstructural effects of materials on TMF. Sehitoglu [23] began trying to isolate the microstructural mechanisms operative in TMF. Later, he and Neu [24] conducted isothermal TMF in various atmospheres to quantify effects of oxidation-induced crack nucleation. They also observed transgranular cracking in TMF as well as intergranular cracking in creep conditions. Remy et al. [25] conducted extensive TMF work on the Inconel nickel-based superalloy, IN-100,

modeling interdendritic oxidation and quantifying its effect on fatigue crack growth for CT specimens.

However this area of “classical TMF” is chiefly based on the effects of alternating thermal loads with mechanical loads. These loads are normally applied in-phase (IP), whereby a specimen is put into tension when at high-temperature, or out-of-phase (OP) with high-temperatures applied when the specimen is at its low load. This research can be very useful and some classical TMF data acquired by Marchand et al. [26] on the material for this study has been used. However, the current investigation involves a more complex interaction of thermal and mechanical behavior than simply IP and OP TMF. Therefore, a survey of other areas of thermal research has been included and follows.

2.2.2 Thermal Shock and Thermal Fatigue

We define thermal fatigue as the effects of alternating temperatures on materials without applying mechanical loading, the resulting thermal strain alone produce the resulting critical stresses.The initial work [18-21] surveyed in the introduction of section 2.2 may be classified as being more foundational to thermal shock and thermal fatigue than to classical TMF. In fact, thermal shock, defined as the effects of sudden or rapid temperature changes on materials, is more closely linked to thermal fatigue, than TMF.

Glenny [27, 28] did some of the initial work in thermal shock and thermal fatigue by using what became known as fluidized beds. He did so using wedge-shaped specimens, which were immersed in such beds and the effects of the wedge produced thermal gradients and thermal cracking. Thermal fatigue resulted as Glenny alternated the immersion of the specimens into the beds. Rezai-Aria et al. [29, 30] also did work investigating specimen geometry on thermal fatigue. And most recently, researchers like Engler-Pinto [31] and Meyer-Olbersleben (along with Engler-Pinto and Rezai-Aria) [32] have continued this work.

2.2.3 Thermal Gradient Studies

The behavior of structures experiencing a hot spot involves the effects of thermal gradients in components. Thermal gradient analysis has been researched widely for pressure vessel technology, mainly involving modeling cylinders with axial loads. In such applications, higher temperatures exist on the inside wall of the cylinder with cooler temperatures on the outer wall.

Such work has been accomplished by applying heat by various methods. Wrapping induction coils around round specimens for heat applications has been the most common method [33, 34]. However, direct flame or burner rig-type heat sources have also been used. This direct flame testing [30, 35] technique normally allows for higher temperature application and lends itself to a more "thermal shock" style approach, while the induction coil heating has the benefit of being easier to control.

The area of thermal gradient study most applicable to the current work, however, involves that which produces a buckled plate. Instead of applying a thermal gradient through a somewhat thick material, the present investigation concerns the effects of a planar gradient on a relatively thin material. Thermal buckling of thin, axisymmetric plates has been modeled, normally with simply-supported restraints [36, 37]. Tani has obtained significant thermal buckling results using an initial deflection [38] as well as an elastic instability [39] to initiate the buckling behavior. However, there is little of this type of work that includes viscoplastic material properties.

There have been significant strides made in modeling creep and plasticity with thermal gradient applications, but they have been in the aforementioned pressure vessel area of research. Morjaria and Mukherjee [40] were some of the first to model transient thermal stresses for inelastic boundary value problems. More recently, viscoplasticity has been modeled in pressure vessel applications using the boundary element method developed by Providakis et al. [41]. Other creep modeling by Law et al. [42] has been accomplished using "Theta

projection" data for through-wall temperature gradients. Kim and colleagues [43] investigated the validity of the J-integral in thermal shock applications because of a constraint effect. So while much has been done in the study of thermal gradients and thermal shock, and there is precedent for modeling such loads in FEA, there is very little research in the viscoplastic effects of planar thermal gradients.

2.3 Fracture Mechanics and Fatigue Crack Growth

The ultimate failure in fatigue is always precipitated by fatigue cracking at some level. This cracking, also known as fatigue crack growth (FCG), has become a foundational area of study as it pertains to damage-tolerant design. Damage tolerance is a mechanistic philosophy and methodology whereby the remaining strength and/or life of a component is determined after measurable damage. According to this type of methodology, one deems a certain amount of damage to a component acceptable for use if it can be quantified at a non-critical stage. More specifically in regards to fracture mechanics and fatigue design, a certain known crack length, a, is acceptable up to a certain critical length, a_c. The origin of this study has its roots fracture mechanics and a review of the work done in this field along with FCG is very pertinent to this research. This section will survey this work to include Linear Elastic Fracture Mechanics (LEFM), Nonlinear Fracture Mechanics, and a section on how to model each of these areas using FEA. Because of its close relationship, contributions involving both fracture and FCG will be chronicled throughout each subsection.

2.3.1 LEFM

The study of fracture mechanics has its origins in linear elastic fracture mechanics (LEFM), whereby the amount of plastic deformation is minimal and located just ahead of the crack tip. Brittle fracture testing was first performed by

Inglis [44] in 1913 and was finally quantified by Griffith [45] in 1920 using the First Law of Thermodynamics and an energy balance in looking at the stress analysis of an elliptical hole. Later, Irwin [46] and Orowan [47] improved on Griffith's work by accounting for local plasticity, thereby representing cracking in metals more accurately. Westergaard [48], Dugdale [49], and others followed as modifications to LEFM continued in efforts to more rigorously account for the mechanics of cracked materials. However, it was Irwin who should get the credit for recognizing the significance of the effects of what we now know as K. This singularity in determining the stresses and displacements around the crack tip become known as the stress intensity factor and was foundational to the study of fracture and damage tolerant design. The stress intensity K is the most commonly accepted estimate of the crack-driving force.

However it was in 1960 when Paul Paris et al. [50] first applied LEFM to fatigue through the now well-known Paris Law (Eq. 2.2). When plotting a fatigue crack growth rate curve, it is common to plot the *log (da/dN)* versus *log (∆K)* and the result is a sigmoidal shape as seen in Figure 2.3. Paris offered a mathematical approximation of the linear portion of this curve in Region II known as the Paris Law as listed in Equation 2.2.

[2.2] $$\frac{da}{dN} = C(\Delta K)^m$$

C and n are material constants that are determined based on the fit of experimental data. Though not initially embraced by the engineering community, the law became the foundation for modern fatigue crack growth relationships and damage tolerance in fatigue and is still used today.

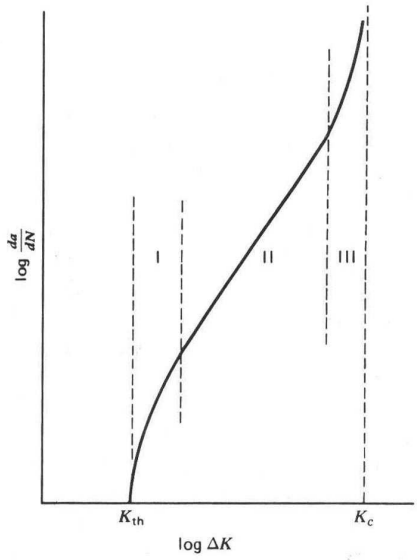

Figure 2.3 Typical FCG data as represented by *log da/dN* vs. *log ΔK* [51]

There have been many modifications to Paris' work, many of which depend upon the specific type of loading of the material. Forman et al. [52] incorporated the applied stress ratio, *R* and took into consideration Region III of the FCG curve, where crack growth is rapid as *K* approaches the fracture toughness of the material, K_c. The Forman equation is shown as Equation 2.3.

[2.3]
$$\frac{da}{dN} = \frac{C(\Delta K)^m}{(1-R)K_c - \Delta K}$$

But it was Walker [53] who is best known for his incorporation of R into FCG estimation. Based on two different aluminum alloys, Walker developed the Walker equation (Eq. 2.4), which modifies Forman's work using an additional exponent, *m*.

[2.4] $$\frac{da}{dN} = C\left[(1-R)^m K_{\max}\right]^n$$

Another modification accounted for the effects of plasticity (while still localized) by considering what has become known as crack closure. Due to the plastic zone that is created at the crack tip, an additional amount of material is now permanently deformed in tension. As the crack extends through that zone (which is now in the crack wake) this additional material closes the crack before the applied stress has reached its minimum. This crack closure results in a decreased ΔK, known as the "effective" stress intensity range, being ΔK_{eff}, which equals the difference between the maximum K and the K when the crack begins to open. The equation for ΔK_{eff} is shown in Equation 2.5.

[2.5] $$\Delta K_{eff} = K_{\max} - K_{op}$$

Elber [54, 55] was the first to truly quantify the effects of FCG due to crack closure. Though this area has been controversial, it has been modified much in the past few decades and is still used.

An additional method of determining stress intensity has been developed based on strain rather than stress. Used normally in high-temperature, TMF fatigue crack growth, this method approximates ΔK_ε by defining K_ε as a function of strain range instead of stress range. Shown in Equation 2.6, this method has been

[2.6] $$\Delta K_\varepsilon = \Delta\varepsilon\sqrt{\pi a}\cdot f(g)$$

used to develop a Paris-style relationship between ΔK_ε and da/dN and with some effectiveness. Both Rau [56] and Gemma [57] led colleagues in showing its validity in approximating TMF crack growth and Creep/TMF testing for MAR-

M200 and B-1900+Hf. Figure 2.4 shows this Paris-like behavior of B-1900+Hf (the material of interest for this study) under various Creep/TMF conditions as found by Gemma et al. [57]

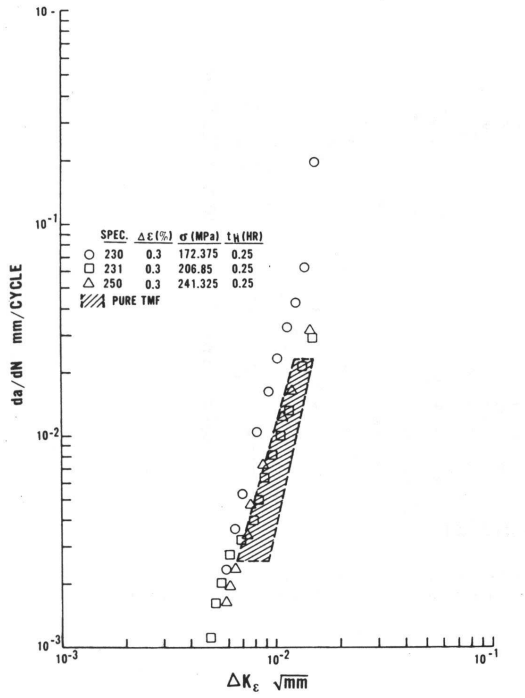

Figure 2.4 Creep/TMF test by Gemma et al. [57] for B-1900+Hf with stress applied at 927 C every 20th cycle for 15 min.

2.3.2 Nonlinear Fracture Mechanics

However, LEFM assumes plastic deformation is limited to a small area ahead of the crack tip. As has been illustrated in section 2.2, large-scale plasticity effects are inherent in most TMF tests, particularly in low-cycle fatigue (LCF).

In 1968 Rice [58] developed a path independent line integral around the cracked region to account for the energy release rate of a nonlinear elastic material. Known as the J-integral, this method was later proved to be applicable to what became elastic-plastic fracture mechanics (EPFM). Hutchinson [59] and

Rice and Rosengren [60] contributed by defining the state of stress in this plastic region as related to the J-integral. Dowling and Begley [61] applied the J-integral to FCG using A5338 steel through Eq. 2.7.

[2.7] $$\frac{da}{dN} = C(\Delta J)^n$$

However, other researchers were determining a means of quantifying the nature of the blunting of the crack tip due to plasticity during fatigue. In doing so, Dover [62] and McEvily [63] reported on what we now call the crack tip opening displacement (CTOD). Later, Shih [64] determined a relationship between the CTOD and the J-integral using the Hutchinson, Rice, and Rosengren relationships. Thus, the study of FCG through EPFM was truly born and the study of TMF under LCF conditions was transformed by these new developments in fatigue crack growth research.

Others, however developed micro-crack propagation models to include creep and/or plasticity, but without J-integrals. Skelton [65] developed a FCG approach dubbed the plastic strain range-based growth law, which effectively modifies the Coffin-Manson Law. Wareing [66] modified the Paris Law for FCG through a cavitated material, as induced by creep. And of course, a survey of the work in nonlinear fracture mechanics would not be complete without mentioning the accomplishments of Landes and Begley [67], and later Saxena [68], with their work correlating C* and C_t to crack data.

But, the J-integral is most commonly used to quantify nonlinear fracture. Further modifications have been made to extend the scope of the J-integral to more accurately represent the nature of FCG for the given TMF test environment and material. Blackburn's [69] J* and Kishimoto's (et al.) [70] J^ allowed for a wider range of loading and of materials' constitutive response. Extensive parametric studies were conducted by Orange [71] at NASA-Lewis in correlating these parameters, along with others, to different TMF environments for Inconel 718. Under NASA's HOST Program (HOt Section Technology), he showed that

among eight path-independent integrals, the J* and J^ proved to accurately predict FCG behavior of Inconel 718 in isothermal, thermomechanical, temperature gradient, and creep conditions. One other parameter of note, Atluri's (et al.) [72] T* proved to model all environments well, except time-dependent conditions. Kim and Van Stone [73] found that both J* and J^ parameters describe crack growth behavior well for elevated temperatures with a hold time for Alloy 718. They later found [74] that these integrals correlate well to FCG under isothermal conditions when the crack tip deformation has large-scale plasticity.

2.3.3 Modeling Fracture using FEA

While there has been much recent advancement in fracture mechanics and FCG research, progress in these areas has been closely linked to work in fracture modeling using FEA. While K has been understood experimentally since the 1950's, the advent of computational technology and FEA over the last few decades has been much of the driving force behind recent fracture analysis.

Stress intensity factors (SIFs) as determined from FEA have been historically classified as direct or indirect methods. In direct approaches, the FEA solution outputs the value itself. But because SIFs are functions of the individual loads and displacements around the crack tip, it is possible to derive those intensities, computationally, from the loads and displacements as found using FEA, which would be the indirect method. It is important to delineate the contributions made by both approaches to fracture modeling.

2.3.3.1 Direct Methods

Direct methods fall under two categories: 1) ones that employ singular elements surrounding the modeled crack tip, and 2) those using conventional elements without singularity. Figures 2.5 and 2.6 show examples of each.

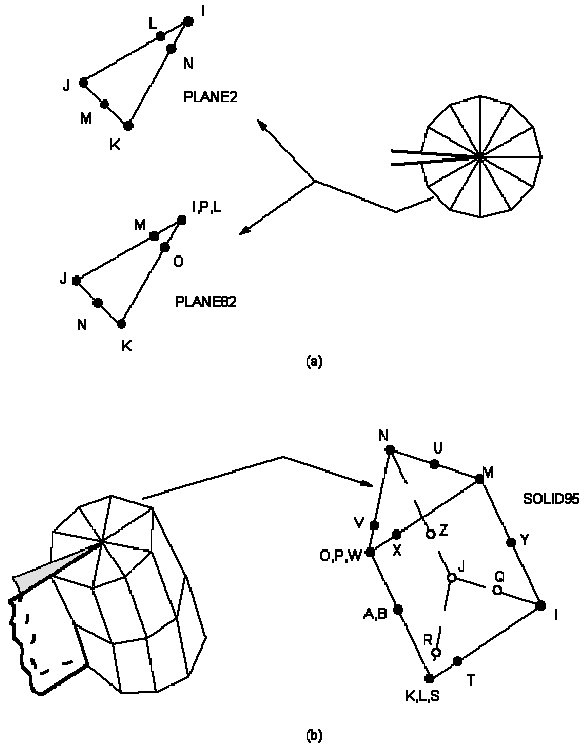

Figure 2.5 Singular elements as created in ANSYS modeling both a) 2-D and b) 3-D crack tips [75]

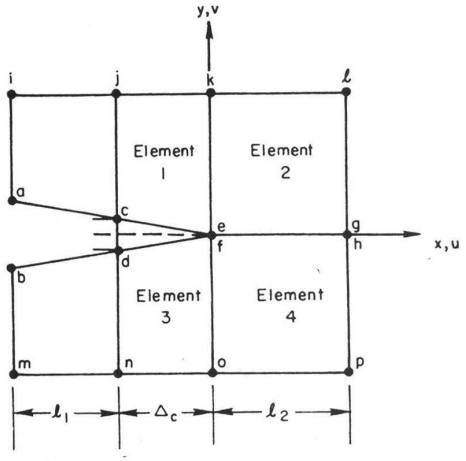

Figure 2.6 Conventional elements used in modeling a crack tip [76]

Much work has historically been done with the singular element method, whereby the singularity is obviously calculated directly. Various types of elements have been used to create this singular form as well. Triangular [77], quadrilateral [78], and polygonal [79] elements have all been shown to work well

for modeling stress intensities. Using conventional elements to directly compute SIFs involves extrapolating stresses and/or displacements to the crack tip using curve fitting.

2.3.3.2 Indirect Methods

This method was first theorized by Irwin [80], himself, through what is known as the crack closure integral (CCI). Gallagher [81], Rice and Tracy [82], and Jerram and Hellen [83] were the first to explain such a process. The basic idea involves two steps, the first of which quantifies the amount of energy in the prescribed crack position under loading. The second step is to approximate the stress intensity by quantifying the work required to close the crack with a unit force at nodes nearest the crack front. But it was Hellen [84] and Parks [85, 86] who first started to quantify what became known as virtual crack extension (VCE). This method is an indirect method, whereby the stress intensity is related to the rate of energy released by a "virtual" amount of crack growth. VCE is predicated on being able to, with one finite element mesh, calculate the energy difference between two nearby crack positions. Hellen's work [84] focused on the relationship of each fracture mode using K, while Parks [86] extended the work to the J-Integral approach.

The value of computing stress intensity for a given crack length in one analysis was applied to the initial CCI research by Rybicki and Kanninen [76]. Known as the modified crack closure integral (MCCI), they determined the strain-energy release rate by using a product of the crack tip forces and the crack face displacements at the nearest node to the crack tip. This method was accomplished with the basic shape functions of 2-D, 4-noded, quadratic elements. Singh et al. [87] extended this work to be independent of element shape functions with a universal CCI (UCCI). Singh, Patel, and Dattaguru [88] also improved on the MCCI with what they called decomposed CCI (DCCI), whereby the SIF could be estimated for 3-D 8-and 20-noded elements along the entire crack front. The equation for calculating the mean value of K of a crack

front using a 20-noded brick elements is shown in Eq. 2.8, where F's are forces at five nodes (subscripted with capital letters) in the element ahead of the crack tip, while the U's are displacements at five specific nodes (subscripted with lower-case letters) at the crack face.

$$[2.8] \quad K_m = \sqrt{E \frac{1}{6\Delta a}\left[(F_A + F_B + F_C)(4U_a + U_b + U_c) + (F_D + F_E)(2U_a - U_b - U_c + 3U_d + 3U_e)\right]}$$

Contributions have been made in the indirect approach by Sehitoglu [89] and Newman [90] regarding estimating SIFs for fatigue and elastic-plastic applications, respectively. Newman [91] also expanded his research to determine a fracture criterion to address not just single cracks, but widespread fatigue crack behavior. However, it is Newman's previous work [90] which became one of many publications of the 1980's and 1990's which began using CTOD as an important means of quantifying fracture mechanics, particularly for elastic-plastic applications.

As has been mentioned, CTOD has become an important means of quantifying the J-integral for elastic plastic fracture mechanics. The work of Carpenter et al. [92] offered comparisons of different methods for modeling J in 3-D applications to include plasticity. One of his colleagues, R. H. Dodds had already begun work with Wellman et al. [93] in determining a J value that quantified the stress intensity by CTOD that was comparable to experimental data. This relationship is shown as Equation 2.9, where σ_{flow} is merely the average of the yield and ultimate strengths of the material, while m is a stress state term. Figure 2.7 shows the correlation of this relationship to experimental 3-point bend specimen behavior of A-36 steel plates [94]. He went on to show that this relationship was valid for thicker A-36 specimens as well in his work with Sorem et al. [95] and others [96, 97]. Figure 2.8 shows the validity of this relationship using square 3-pt bend specimens.

[2.9] $$\tilde{J} = m \cdot CTOD \cdot \sigma_{flow}$$

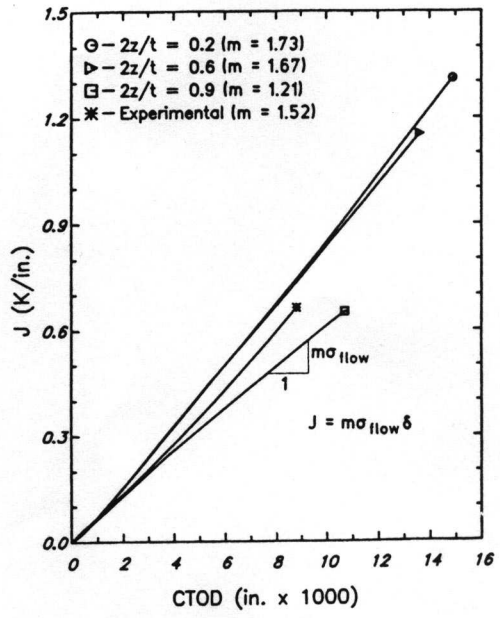

Figure 2.7 Correlation of CTOD to experimental J and J~ as found by Dodds et al. [94]

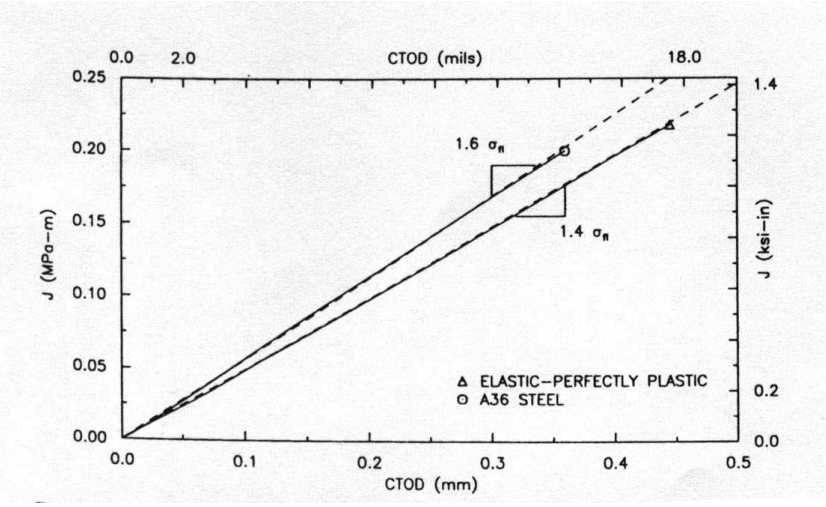

Figure 2.8 Correlation of J~ to experimental J as found by Sorem et al. [95]

Dodds [96, 97] furthered his research and applicability of this relationship, using complex 3-D crack fronts and various crack geometries. Most recently, Gullerud et al. [98] (including Dodds) extended this work of indirect fracture modeling with conventional elements to model fatigue crack growth of thin, ductile aluminum alloys. To do so, they determine a critical crack tip opening angle (CTOA) at which the crack extends. Figure 2.9 depicts the CTOA as determined at a specified distance (L_c) from the crack tip in the mesh.

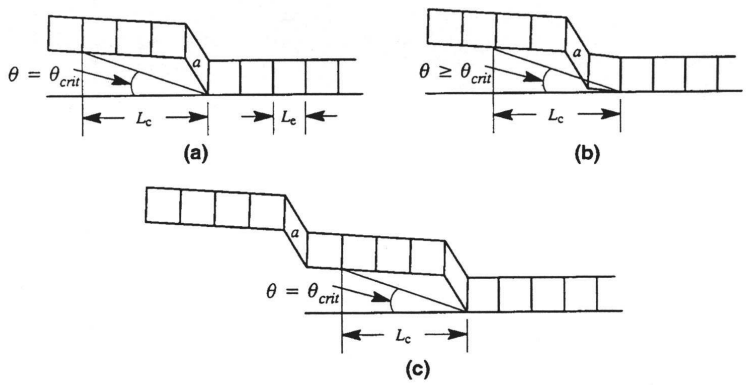

Figure 2.9 Schematic of the CTOA approach to simulating crack growth in a conventionally meshed model by Gullerud et al. [98]

The value of these approaches, which model SIF and FCG without using singular elements is significant. Being able to use non-singular conventional element geometries is an elegant approach, which greatly reduces mesh size, thereby reducing computation duration. Additionally, it offers flexibility of the mesh designer to simulate crack growth without creating separate models for each crack length. With singular elements, one either has to pre-specify several distances to which he/she plans to extend the crack and create singularities around each, or a new model and mesh needs to be recreated at each crack length that is being modeled. The latter option involves, as mentioned, much larger mesh sizes, while the former involves multiple, distinct models which have to incorporate data from each other in order to “grow” the crack appropriately.

While this concludes the overall background research upon which the current investigation stands, extensive material specific research was published that is extremely pertinent to this investigation as well. This research is surveyed in Chapter 3 as the specific material properties used in the ANSYS model are discussed.

CHAPTER 3: CONSTITUITIVE MODELING

Initially, an accurate constitutive model was developed before proceeding to the physical model. The validity of mechanical modeling using FEA is highly dependent upon the material properties used in the model, particularly when the properties are nonlinear. All material properties for this research have been acquired from published sources.

The material used in this study is a nickel-based superalloy, called B-1900+Hf. Nickel-based superalloys have been used in turbine engine applications for over fifty years for their high-temperature mechanical properties. One author goes so far to tie the alloys' development to such applications as he writes:

> The development of nickel-base superalloys has, almost entirely, been motivated by the requirement to improve the efficiency, reliability, and operating life of gas turbines. There have been other peripheral applications but, at present [*1996*] about 90% of superalloys produced are used in gas turbines for a range of applications, including aerospace, electricity generation, gas/oil pumping and marine propulsion. [99]

While most applications are typically the turbine blades and rotors, these alloys are used for many turbine components, including combustor liners. Conventionally cast B-1900+Hf is commonly used for combustor liner applications. Table 3.1 includes the chemical composition of B-1900+Hf as given.

Table 3.1 Chemical Composition of B-1900+Hf [100]

Composition %													
C	Cr	Co	Mo	W	Ta	Nb	Al	Ti	Hf	Zr	B	Ni	Other
0.1	8.0	10.0	6.0	-	4.3	-	6.0	1.0	1.5	0.08	0.015	Bal	-

3.1 Temperature Dependent Properties

The alloy B-1900+Hf has been used, specifically, for combustor liners in some of turbine engines. B-1900+Hf has been researched extensively in recent years. Table 3.2 includes a compilation of the basic time-dependent properties of this material. B-1900+Hf as found in the literature from various sources. Significant work was accomplished by researchers at Southwest Research Institute (SwRI) [101-107] on B-1900+Hf in support of NASA's Hot Section Technology program in the 1980's. The elastic modulus with temperature was acquired via a formula as a function of temperature from Chan, et al. [106] and is listed with the other properties in Table 3.2. (It should be noted here that 1093 °C or 2000 °F is the key hot spot temperature. Thus, having material properties up to this temperature is believed to be crucial to this model.) The Poisson ratios for each temperature that are in normal typeface in the table were taken from that same report [106]. The values italicized were interpolated to fill out temperatures for which data was not provided. The bilinear stress-strain properties, to include the S_y and the tangent modulus are approximations made from Chan's data (as shown in Figure 3.1) from the same report as well [106]. Lastly, the α values per temperature used for the model are shown, with the normal typface indicating the published values found in the ASM handbook [100] for the same material, only without the hafnium added. It is not believed that this element would change the α significantly at all. Again, only the non-italicized values were documented in the source, while the italicized were acquired via interpolation of the trend observed using the published values, as was done in the case of the Poisson ratio.

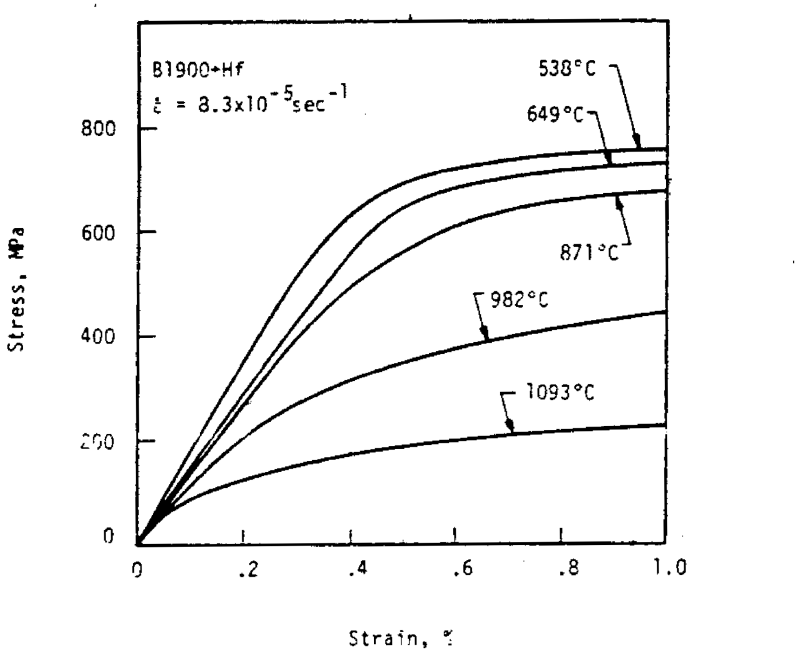

Figure 3.1 Time-dependent tensile data of B-1900+Hf from Chan et al.[106] which was used to approximate bilinear plastic behavior.

Table 3.2: Material properties for B-1900+Hf with temperature

Temp (C)	Modulus[106] (GPa)	ν [106]	S_y[106] (MPa)	Tangent Modulus (MPa)	α [100] (μm/m °C)
21	199.01	.322	780	8000	*10.75*
93	-	-	-	-	11.7
260	196.27	.328	-	-	*11.97*
483	183.97	*.331*	-	-	*13.11*
538	179.58	.331	730	7500	13.39
649	-	-	705	7800	-
760	156.75	.339	-	-	*14.52*
871	142.42	.324	650	7300	*15.09*
926	134.65	*.34*	-	-	*15.37*
982	126.29	.351	350	14700	*15.65*
1037	117.65	*.351*	-	-	*15.93*
1093	108.44	.351	175	7600	16.22

Each of these values was incorporated into the ANSYS material model. The plasticity properties (S_y and tangent modulus) were each input into a bilinear kinematic hardening model, whereby the material hardens only kinematically. The was done based on Figure 3.2 showing research of Marchand et al. [26] in the HoST program. In testing, the authors noted that the figure indicated that the maximum stress in the IP cycling continually hardened while the minimum stress in the OP cycling continually softened. They went on to state, “continuous hardening of σ_{max} and softening of σ_{min} occurred until final fracture without evidence of saturation.” Such behavior is indicative of kinematic hardening, in which the yield surface translates instead of expands, as indicated by isotropic hardening. Though most materials behave with a combination of both types of hardening, only kinematic hardening is included due to these conclusions.

It should be noted that ANSYS linearly interpolates the trends indicated by the values in Table 3.1 for intermediate temperatures that do not have defined values.

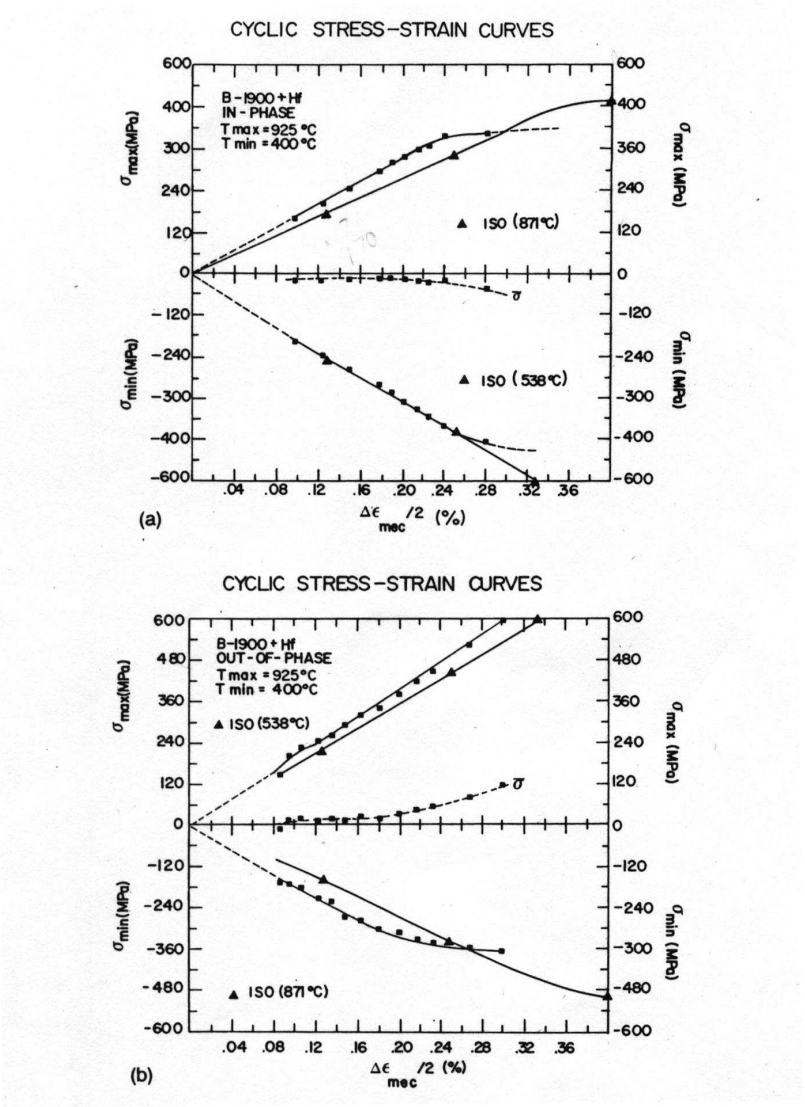

Figure 3.2 a) TMF-IP and b) TMF-OP cyclic stress-strain curve data of B-1900+Hf by Marchand et al. [26] indicating a trend toward kinematic hardening

3.2 Time-Dependent Properties

As with many turbine engine components, the time-dependent behavior is extremely important to characterize as structures remain at high temperatures and stress for extended times. Creep (change in strain over time with constant applied stress) is the most common time-dependent phenomenon experienced by engine structures (i.e. rotors and turbine blades). However, when a material

is held at a constant strain over time under high enough temperatures, the stress can change (or relax) over time. Known as stress relaxation, this is expected to occur with a hot spot as a local area remains hotter than the surrounding metal and is therefore constrained and in compression for a duration of time. At creep-level temperatures, this compressive stress is expected to relax over time within the hot spot.

In another SwRI report, Chan et al. [104] reported creep research on B-1900+Hf. They ran creep tests at 5 different temperatures at different applied stress levels to determine the steady state creep rates for varying stresses at each temperature. Their results are presented in Figure 3.3, showing steady-state creep rates with applied stress at 760, 871, 982, and 1093 °C. Since the paper was to show the effects of unified constitutive models, those model approximations of that data are shown as well. A test was run at a fifth temperature (649 °C) but caused no creep at 690 MPa. While there appeared to be a fairly consistent trend at 871 and 982 °C of increased strain rates for increased temperatures, the data at 760° C indicated a wide range of strain-rates with very little change in the applied stress. Additionally, insufficient test data at 1093 °C was presented. Therefore, the time-dependent behavior of the material could not be adequately quantified without more experimental data. Additional data was found in two NASA reports (one by V. Moreno, et. al[108] and one by J. Whittenberger [109, 110]) to extend the data to more extreme applied stress levels in order to better approximate the trends. Figure 3.4 shows all the data from each source. (Note the axes are switched from Figure 3.3 to Figure 3.4 in order to put the actual independent variable, applied stress, on the x-axis while the dependent secondary creep rate is on the y-axis).

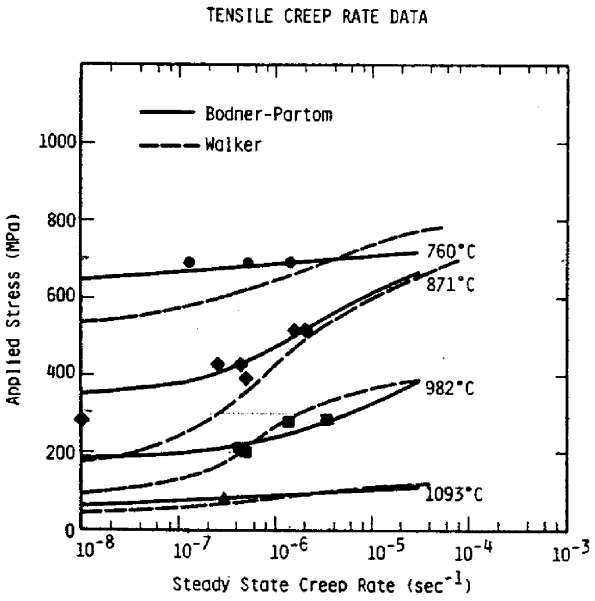

Figure 3.3 SwRI data reported by Chan et. al [104] on B-1900+Hf.

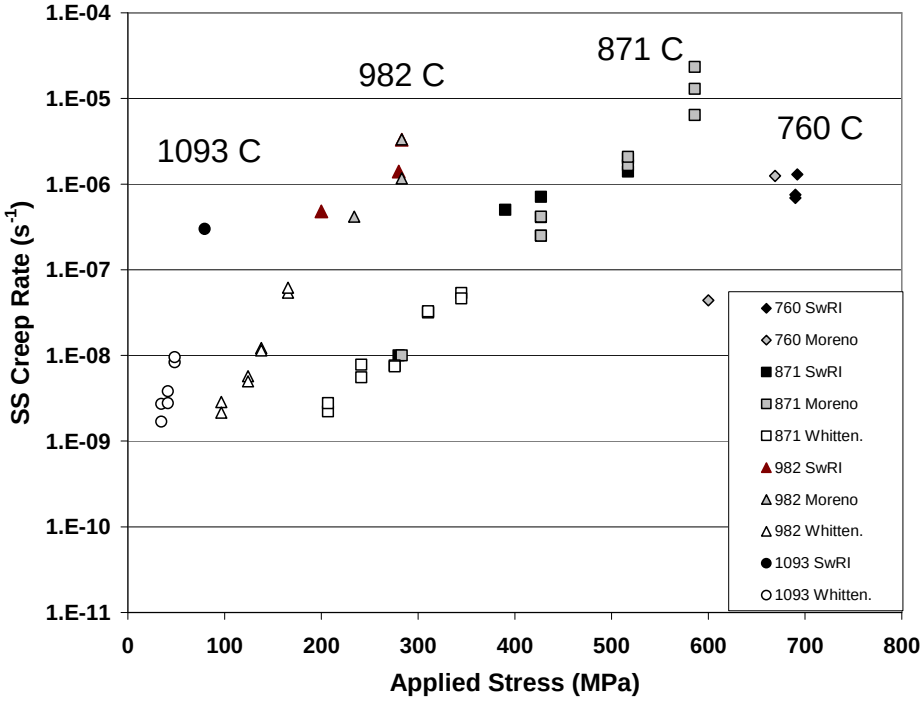

Figure 3.4 "SwRI" creep data as acquired by Chan et. al [104], "Moreno" data reported from the report by Moreno et. al [108] , and "Whitten." data from J.Whittenberger [110].

Consistent trends are now shown for the data across each of the temperatures, with the axes switched (to reflect the dependent variable of

steady-state creep rate along the y-axis, while the x-axis is now the independent applied stress). With this data, power trend lines in Excel were above an R-squared (correlation coefficient between the variance of y and x) value of 0.95 for the highest three temperatures and above 0.86 for 760 °C. The graphs of these trends are shown in Figure 3.5 with solid bold lines.

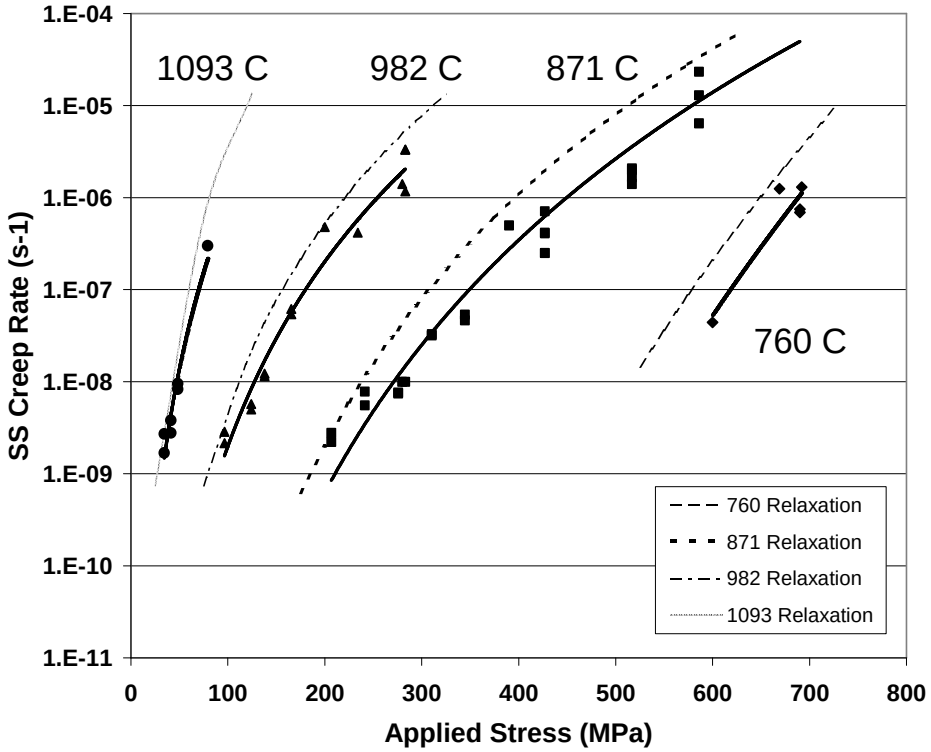

Figure 3.5 Creep data [104, 108, 110] as modeled by a power-law trend fit (shown with bold, solid lines) as well as the relaxation-matching final ANSYS model constants.

The Arrhenius equation has often been used to model the thermally activated behavior of materials over time. A general form of the equation was developed by Bird, Mukherjee, and Dorn [111]. ANSYS utilizes the simpler, Norton [112] form of this equation more commonly called the basic power law equation; this is shown as Equation 3.1.

[3.1] $$\dot{\varepsilon}_{cr} = C_1 \sigma^{C_2} e^{\frac{-C_3}{T}}$$

However, before transforming this data into steady-state time-dependent properties to be used in ANSYS, it was more important to make sure stress relaxation and not creep was fit more closely. The SwRI group [103] also conducted stress relaxation tests on this material at both 760 °C and 982 °C. After conducting TMF cycling, the materials were held with constant mechanical strain at these temperatures and the relaxation of the stress with time was recorded. Figures 3.6 and 3.7 show the stress relaxation for two-hour holds at the same mechanical strain range for two different temperatures. Figure 3.6 shows isothermal cycling at 538 °C and a two hour hold at 760 °C and which shows the stress level decreasing from ~605 MPa to ~540 MPa. Figure 3.7 shows the results of the same procedure, only the two-hour hold is now at 982 °C and the stress drops from ~350 MPa to ~120 MPa.

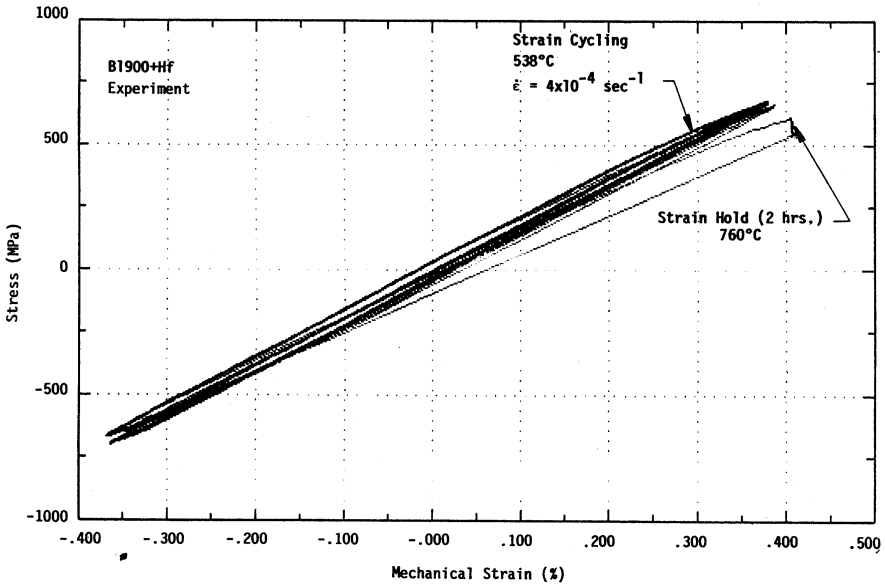

Figure 3.6 SwRI [103] data for stress relaxation at 760 °C with a two hour mechanical strain hold

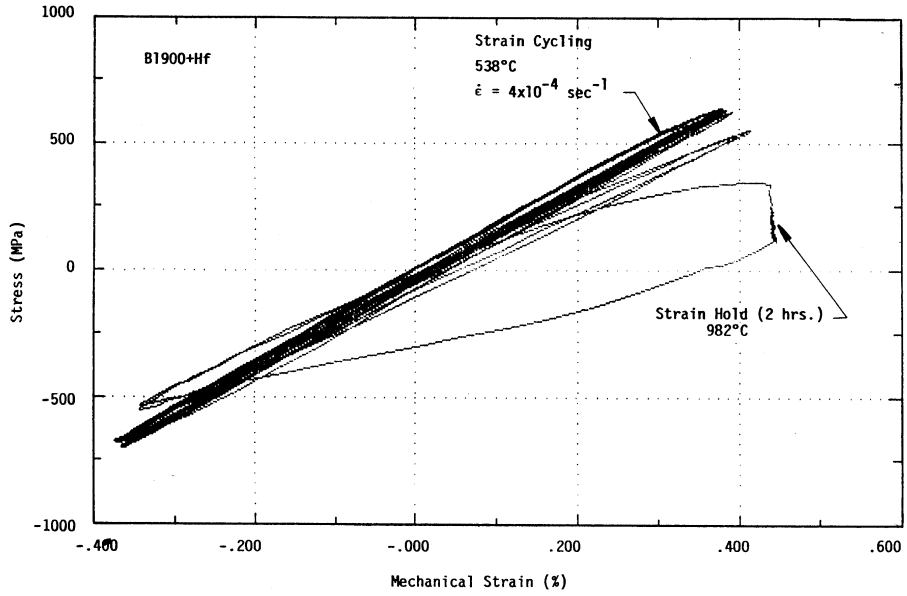

Figure 3.7 SwRI [103] data for stress relaxation at 982 °C with a two hour mechanical strain hold

Eq. 3.1 was modified to account for stress relaxation. The equation was first modified to account for the change in stress with time instead of change in strain. Replacing the creep rate with the change of stress divided by the modulus and with the partial derivative with time separated, the equation becomes

[3.2] $$\dot{\varepsilon}_{cr} = \frac{\partial \varepsilon}{\partial t} = C_1 \sigma^{C_2} e^{\frac{-C_3}{T}} \rightarrow \frac{\partial \sigma}{E} = C_1 \sigma^{C_2} e^{\frac{-C_3}{T}} \partial t$$

With stress terms on the left, the partial differential equation becomes

[3.3] $$\sigma^{-C_2} \partial \sigma = C_1 E e^{\frac{-C_3}{T}} \partial t$$

Finally after integration, a closed form equation is given in Equation 3.4 with the change in stress level a function of the same creep constants and the change in time.

[3.4] $$\sigma_f^{-C_2+1} - \sigma_o^{-C_2+1} = (-C_2+1)C_1 E e^{\frac{-C_3}{T}} t_f$$

The constants (C_1, C_2, and C_3) were now chosen to represent that the final "relaxed" stress within 5 MPa of the SwRI test results. The final constants used in the ANSYS model are listed in Table 3.2 along with the original constants as determined by the trend fit.

Table 3.2 Constants for Norton Equation before and after fit with stress relaxation data

$$\dot{\varepsilon}_{cr} = C_1 \sigma^{C_2} e^{\frac{-C_3}{T}}$$

Temp (°C)	C_1		C_2		C_3	
	Initial	After relaxation fit	Initial	After relaxation fit	Initial	After relaxation fit
760	5.8×10^{-46}	9×10^{-41}	21.5	20	51800	52800
871	1.39×10^{-10}	2×10^{-9}	9.112	9	53500	54500
982	8×10^{-4}	4×10^{-3}	6.669	6.68	54790	55650
1093	.3	2	6.005	6.1	54800	56500

It should be noted that this modification to the constants for relaxation was applied to all four temperature levels, even though only data for 760 °C and 982 °C existed. The modifications for 871 °C and 1093 °C were made based on the same approximate shift as made by 760 °C and 982 °C. The graphs of how the original trend fit and the relaxation modified model match the creep data are

shown in Figure 3.5 with the dashed lines showing the relaxation matching trends.

The shift in the curves not only matches the stress relaxation behavior, but is a conservative shift in creep estimation. The modification results in modeling the fastest creep data points for a given applied stress for each temperature. This slight difference has been observed before, whereby relaxation data and steady-state creep data are not both well-predicted [113, 114] from a Power-Law model like the Norton equation. However, these curves are still very reasonable approximations of the data, and again, relaxation is more important in this case.

Additional material properties for B-1900+Hf have been researched and determined that are pertinent to this study. Most notably, additional study was accomplished by Marchand and Pelloux [115] on the isothermal FCG behavior at both high and low temperatures for study of the effects of plasticity on crack growth. However, because this research is integral to the crack and crack-growth modeling accomplished in this study, the pertinent material properties are discussed in Chapter 6.

3.3 Conclusions

Material properties testing was not within the scope of the current investigation. No specimens were provided for any tensile, cyclic, or TMF characterization. Therefore, the only means of constitutive model validation is as a result of the blister model validation as compared with the experimental test which will be accomplished in the next two chapters. However, with data from published sources, each necessary material property was adequately determined for use in the ANSYS blister model. The following points summarize the constitutive model findings:

- The published temperature dependent tensile properties can characterize the reversed loading, compressive, as well as tensile behavior at temperature ranges up to 1093 °C.

- The yield and subsequent plastic hardening behavior of the material is approximated as bilinear as based on the published curves found from the research by Chan et al.

- The material properties at the specified temperature levels are linearly interpolated by the ANSYS.

- Based on the findings of Marchand and Pelloux [26], the hardening behavior of B-1900+Hf is concluded to be kinematic only, in spite of many materials normally behaving as a combination of kinematic and isotropic.

- While the published steady-state creep behavior can be easily determined from multiple sources for four different high temperature levels, a conservative shift towards faster creep rates is necessary if the properties are to match stress relaxation behavior.

- It is assumed that no measurable creep or stress relaxation behavior occurs below 760 °C for even high levels of applied stress.

CHAPTER 4: BLISTER MODELING FOR ONE THERMAL CYCLE

In order to represent the combustor liner hot spot behavior, an experimental “blister” test was developed to simulate the repeated thermal cycles using a burner-rig set-up. With this blister test serving as a means to characterize hot spots, an FEA model was developed based on the loading and geometry of this test. While the same geometric model serves as the representative structure for repeated thermal cycles, as well as eventual fracture behavior, this chapter details the basic techniques used to portray the effects of just a single thermal cycle using the ANSYS FEA code.

4.1 Blister Test Set-up

The experimental work for this project was conducted at the Pratt & Whitney Company in E. Hartford, CT. The experimental work was accomplished with one specimen of the material which was tested for 462 thermal cycles.

A schematic of the blister test set-up is shown in Figure 4.1. The figure shows a Bunsen burner-type test stand with a specimen of the test material resting on the frame. The specimen is not clamped or fixed in any way to the frame. An oxygen-propane gas mix is used to fuel the burner-rig. The thermal loading is controlled using the data acquired via a thermocouple (T/C) attached at the center of the specimen where the heat is being applied. This center thermocouple is in a feedback loop with the burner-rig and an air-cooling jet in order to control the center temperature of the specimen where the hot spot is located. Additional thermocouples are shown attached at distances (r = 1.27, 2.54, and 4.13 cm) away from the center; these were used strictly for thermal gradient estimation. Finally, a dial gage is placed at the specimen center to monitor the out-of-plane displacement resulting from the thermal cycle(s).

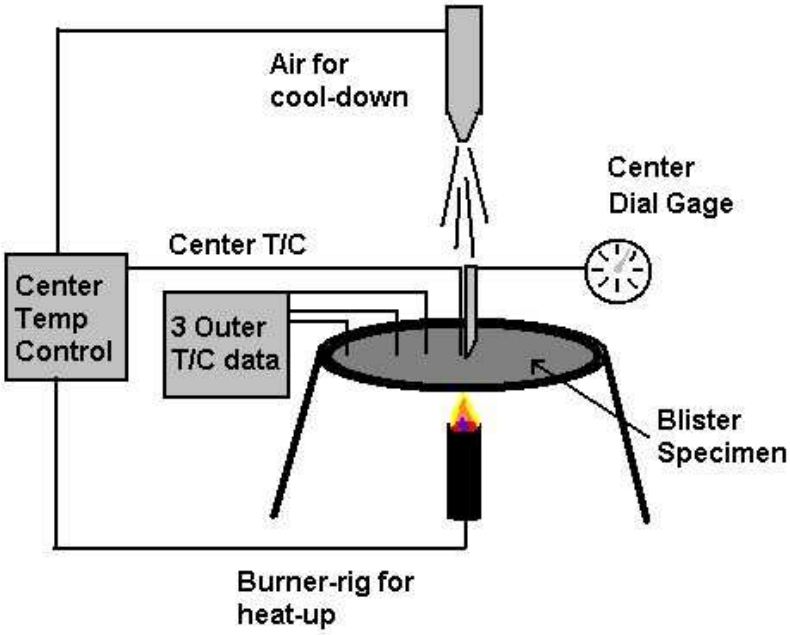

Figure 4.1 Blister test set-up schematic, showing burner and air-cooling inputs as well as data collection devices.

The disk's thickness is not uniform across the diameter. It is 1.51 mm thick out to a radius of 16 mm. This thickness then begins to taper linearly to a thickness of 1.35 mm at the edge. This was the structure modeled by ANSYS 7.1.

Because of the axisymmetric nature of the loading, a quarter plate model was constructed, using symmetry boundary conditions along the two, radial edges being the x and y axes. One additional structural boundary condition was imposed, that being restraining a node in the z-direction at the outermost radius along the x-axis. It was restrained simply to prevent rigid body motion in the z-direction. "SOLID 186" brick elements were used in the model. These elements are 20-noded structural elements with mid-side nodes on edges that model

quadratic displacement. The elements are capable of modeling temperature dependent plasticity, hardening, and creep material properties.

4.2 Thermal Gradient Determination

For the experimental test, thermocouples were placed at four radial locations (r = 0, 12.7mm, 25.4mm, and at 41.5mm) labeled TC1, TC2, TC3, and TC4, respectively, on the top side of the disk. The temperatures were recorded with time for one thermal cycle. Figure 4.2 shows the temperatures recorded for the four thermocouples. The out of plane displacement of the hot-spot center was recorded also for validation of the constitutive model.

The stresses in the structure all resulted from the applied thermal gradient, therefore the size of the gradient is important. The four experimental temperature readings with time were used to approximate the gradient across the entire radius. In order to model such a gradient, an ANSYS model was created with 32 annular volumes in-plane, with 2 volumes thru the thickness for a total of 64 annular volumes. Each volume has a radial dimension of 1.27 mm (0.05 in) except the outermost volume which is 1.905 mm (.075 in). With the volumes, individual temperatures could be assigned to each volume and thereby each element within each volume for any point in time. Figure 4.3 shows these volumes. Additionally, Figure 4.3 shows the model of the quarter plate along with the axis system that will be used for the analysis of all results.

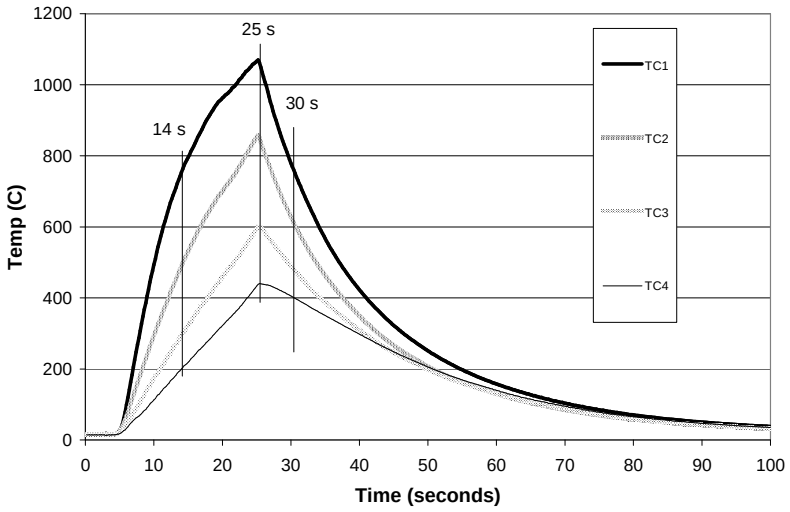

Figure 4.2 Thermocouple readings for 4 radial locations vs. time during initial blister test

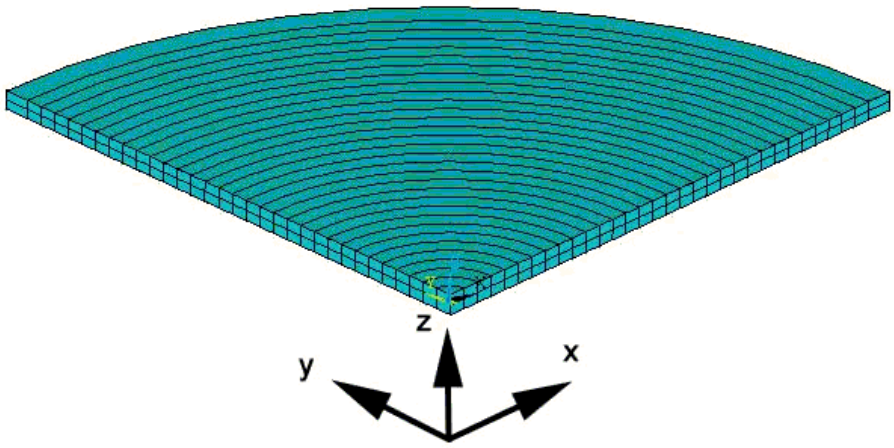

Figure 4.3 Quarter plate and axis system showing volume sections created in ANSYS that are used to create the blister hot spot an in-plane thermal gradient, loading each volume with a distinct temperature.

4.3 ANSYS Thermal Load Steps

Figure 4.4 shows the temperature gradients across the radius that were chosen to represent three specific times during the thermal cycle. The four lines

intersecting each curve indicate the actual data points acquired from the thermocouples at the shown times. The other points are distinct temperatures which were interpolated to extend the trend of the experimental data using basic thermodynamic trends. Specifically, the intermediate points were manually chosen to fit hyperbolic sinusoidal-type curves (as shown in Fig. 4.4) between the measured points reflecting typical thermodynamic behavior via conduction. These temperatures are input as body temperatures for all elements within annular volume sections under the "BFV" ANSYS command. The three distinct times chosen, as previously noted in Figure 4.4, refer to three distinct stages of the gradients in the thermal cycle.

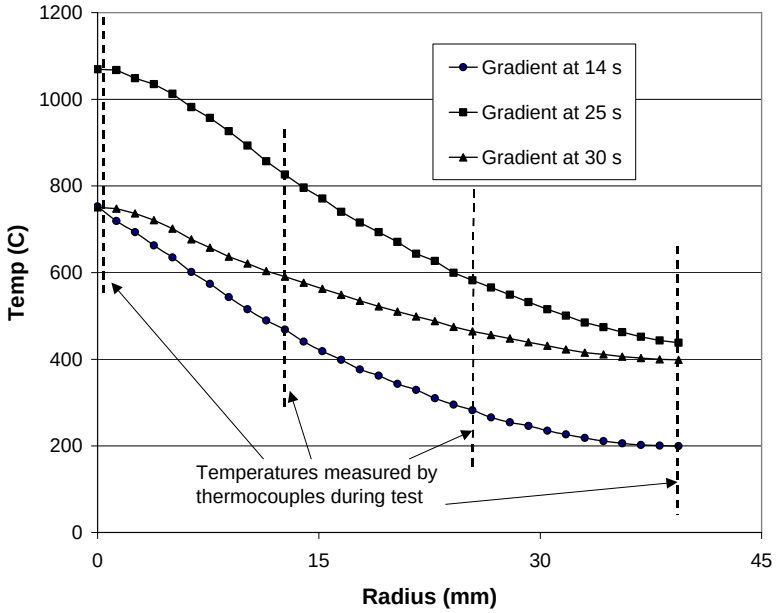

Figure 4.4 Discrete temperature levels used to load ANSYS temperature gradients created from the four thermocouple readings with time.

The first stage occurs in the first 14 seconds of the heating up period, whereby all temperatures are below 760 °C, which is when time-dependent behavior begins. For this stage, an ANSYS load step is written to reach the gradient without a strain-rate (or time-dependent) effect, so as to minimize extremely low stress relaxation rates. The second stage continues the heat up to the final, highest temperature gradient, reached experimentally at 25 seconds. In this stage, the temperatures are high enough to cause measurable creep with

nominal applied stresses, thus the strain-rate effect is “on” to allow for stress relaxation. The third stage is reached around 30 seconds and there is a portion of the cool down that remains in a time-dependent state (above 760 °C). There is a fourth stage for each cycle at which the temperature gradient returns to a uniform temperature of 37.7 °C and does not have a strain-rate effect. An important point to each of these thermal steps is that the temperature change is linear within each step, but there are obviously different heating rates between steps. Each of these four stages is used to define each ANSYS load step within the thermal cycle and each load step.

4.4 Modeling Buckling

Any model for this research also had to ensure that large displacement and rotation were permitted in the element behavior in order to ensure that the instability could be modeled correctly. The ANSYS command “NLGEOM, 1” accomplishes this, by ensuring that the potential for a nonlinear geometric response exists. Because both geometric and material nonlinearities exist; each load step has 40 substeps in order ensure convergence.

In the experimental test, the center of the specimen moved toward the flame side during heating (creating a convex flame or bottom side and a concave top side.) While this is considered a true instability where the direction of the buckling is not believed to be consistent or important, the goal of the model was to represent the experimental behavior as accurately as possible. To ensure the ANSYS model initiated the geometric nonlinearity to move the specimen center toward the bottom, the thermal gradient in the first load step was divided into a hot side and a cooler side, referring to the thru thickness temperatures. By having a slight temperature differential between the top and bottom, the model would initiate the instability in the preferred, hot side direction. Recall, that the model was created with a two-volume thick property. Therefore, the “bottom” volumes were designated with 0.5% higher values than the top side. For the

remaining three load steps in the cycle, no gradient through the thickness was used.

4.5 Results and Validation: One Thermal Cycle

Figure 4.5 shows the change in the stress at the hot spot center, at the node at the top surface as well as for the bottom surface for the entire thermal cycle, divided into the four distinct load steps of the cycle. The stress plotted is technically the stress in the y direction; however because the two nodes are both at the axisymmetric center, an equal biaxial stress state exists to where $S_y = S_x = S_r = S_{\theta}$.

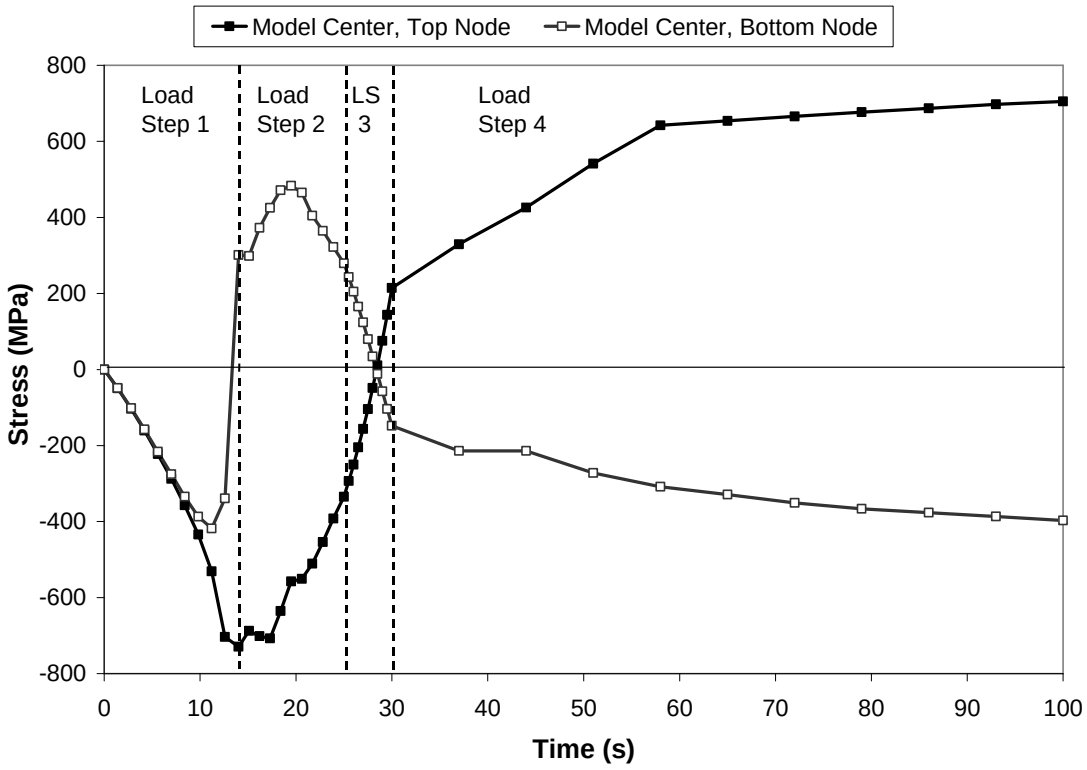

Figure 4.5 ANSYS plot at of Sy (Normal to vertical plane) showing the deformed shape upon coo down (40 s).

During the first load step, the stress at both the top and bottom node are virtually identical, linearly increasing in compression until ~10s. At this point, enough compression has developed radially in the mesh to buckle the model downward and the model takes a shape with a concave top side and a convex bottom/flame side. As this occurs, the stress along the top and bottom diverge as plate bending begins due to the buckled shape. The top node not only remains in compression, but the bending induces even more at a steeper rate. The compressive stress levels off just before the end of the load step as yielding in compression occurs. The bottom node, however, rapidly becomes tensile by the end of the load step.

Load step 2 completes the heat up (with time-dependency) and the model takes the shape as seen in Fig. 4.6. During this step, both the top and bottom node depict stress relaxation as the temperature increases. This relaxation is depicted by the movement of stress towards the graph centerline of zero, showing a decrease in magnitude. The steps of increasing magnitude are due to the stress induced as the model continues to heat up, the model displaces more out-of-plane and more bending occurs. It is important to note the bottom surface has yielded in compression while the top has not. This is due to what effectively is a state of combined loading, where both bending stresses and additional in-plane compressive stresses exist. So, while the top node is in compression due to bending, additional radial compression is added due to the thermal stresses from the continued heat-up. As a result there is a qualitative difference in the trends of the two; the top node, with more stress, relaxes sooner than the bottom, which shows a gradual increase in stress and then relaxation. Figure 4.6 shows the obvious “blister” downwards. The maximum magnitude of the out-of-plane displacement at the model center was 3.05 mm, which compares favorably with the experimental value of 2.46 mm, which is just under 24% error. (It should be noted that the rectangular plane seen at the right side of the ANSYS results image in Figure 4.6 is a contact element plane. While it is necessary to have this plane in the model at this stage for later crack modeling, it does not impact the current results.)

During load step 3, the model begins cooling down and the stresses move to opposite signs due to the model contraction. As the model cools and as all the elements contract, the buckled shape now tries to return to its original, flat shape. When it does so, the representative bending behavior switches, with the top node now taking on tensile behavior and the bottom node, compressive behavior. This occurs linearly until the end of step 3 at 30 seconds. Because the stress values are so low during this step, there is no relaxation occurring, even though time-dependent properties are still active.

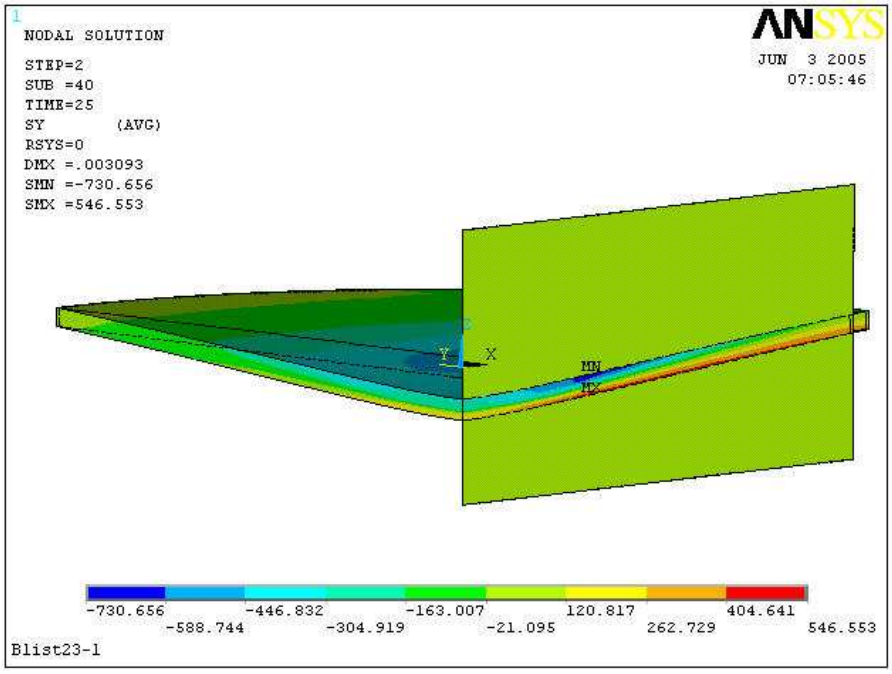

Figure 4.6 ANSYS plot at of Sy (Normal to vertical plane) showing the deformed shape upon heat up (25 s).

As load step 4 begins, the rate effect is off again to ensure insignificant creep strains are calculated as the model cools back to a uniform temperature of 38 °C. There is a noticeable change in slope in the top and bottom node stress trends. However this change in slope occurs due to a significant change in the cooling rate, not the rate-dependency of the model. The cooling is much slower in Step 4 (See Fig 4.2 in the area after the 30s point), thus the change in stress is

slower as observed in the experimental test. The top surface shows yielding in tension close to 60 seconds. The yield level is different in magnitude than occurred during load step 1 due to the Bauschinger Effect as modeled by the bilinear kinematic properties incorporated in the model. The final shape after one thermal cycle is evident in Figure 4.7, an image produced at 100 seconds, which is the total time needed for one cycle. The slight bow downward (with a concave top side and a convex flame side) that remains is a result of the plastic strain resulting from the first two load steps of the heat up. The amount of this plasticity will be discussed in the next chapter which details the results of several thermal cycles.

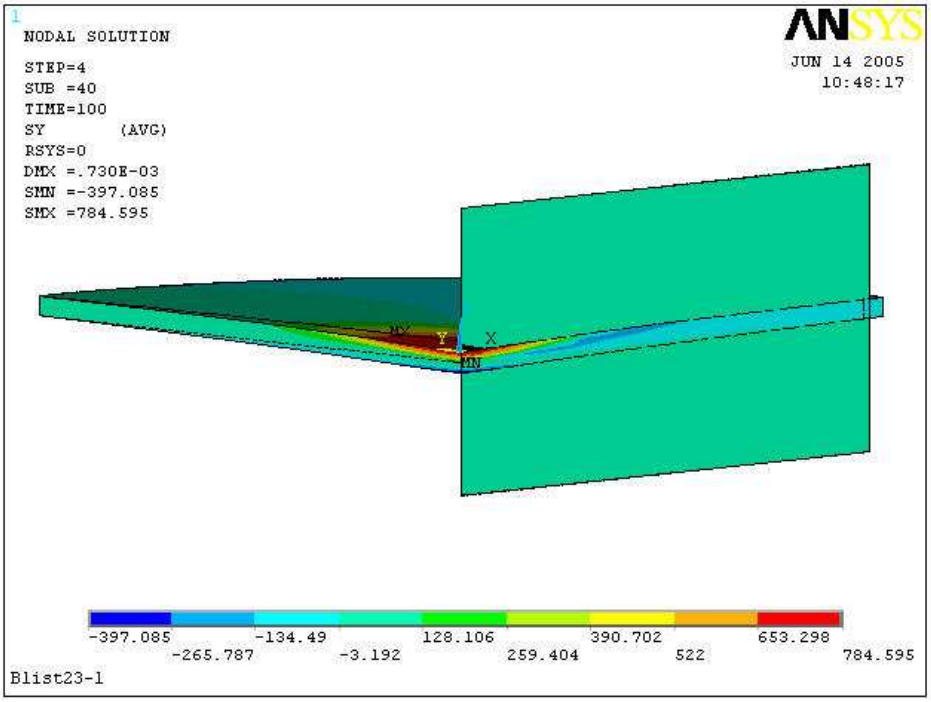

Figure 4.7 ANSYS plot at of Sy (Normal to vertical plane) showing the deformed shape upon cool down (40 s).

The same out-of-plane displacement data was compared at the end of the cycle. Figure 4.7 shows the residual displacement resulting from plasticity effects. The displacement of the ANSYS model in the center was 0.72 mm while

the experimental value was 0.84 mm. The percent error for the cool down drops to 14%.

4.6 Conclusions

The blister model for one thermal cycle was deemed successful in representing the experimental test, particularly in the overall specimen out-of-plane displacement. As a result, many conclusions are made regarding the constitutive and geometric modeling of the structure.

- A quarter-plate with symmetry boundary conditions can represent the behavior of a circular blister test specimen sufficiently.

- With an error (in comparison to the experimental test) of 24% at heat up and 14% at cool down in comparing the out-of-plane displacement for a model that possesses both geometric and material nonlinearity, the material properties used in the model as denoted in Chapter 3 are representative of B-1900+Hf.

- The assumed temperature gradients developed from four thermocouples used in the sequential thermal loading procedure adequately approximate the actual thermodynamic application of heat via the burner-rig test set-up.

- The geometric nonlinearity capability incorporated into the model, allowing large strains and rotations, along with a slight (0.5%) thru-thickness temperature gradient are all that is required to initiate the instability or buckling that occurs in the model.

- The buckled shape creating what is known as the “blister” takes its eventual basic form within the initial heat-up. Yielding occurs at the hot spot center, primarily on the top surface, which creates the permanent specimen blister, even after cool-down.

- The in-plane stress behavior at the center is governed by bending, with tension occurring on the bottom and compression on the top during heat-up, while cool-down reverses this behavior. The yielding that occurs creating the

deformed shape occurs at the top surface, with compressive yielding at heat-up and tensile yielding at cool-down.

- Stress relaxation occurs at the center of the specimen when temperatures exceed 760 °C. Since the greatest stress magnitudes upon heat-up occur on the top surface in compression, this is where the greatest relaxation takes place. The highest magnitude of stress is always at the top surface (whether in heat-up or cool-down) because of the combined loading effects of bending and radial compression or tension that result at the center.

- A list of functions or options that must be specified in the ANSYS code for the current analysis (with the actual ANSYS command) are summarized as follows:

- Bilinear kinematic hardening is used to define the yield, tangent modulus, and hardening (BKIN)
- Norton secondary implicit creep is modeled (TB, CREEP, , , ,10)
- Geometric nonlinearity is on (NLGEOM ON)
- Rate dependency is on for the 2nd and 3rd load step for each thermal cycle (RATE, ON)
- For each load step, 40 substeps are used, with a maximum possible number of 60, to ensure convergence. (NUSUBST, 40, 60, 40)

These conclusions are important in reviewing the model's behavior. The model results reveal much about the why the specimen behaves the way it does and why it is dubbed a "blister" test. The model is representative of the single blister cycle tested, when the out-of-plane response is compared. The trends observed in just one thermal cycle form the foundations for the next two chapters, being the repeated cycling and crack modeling. Furthermore, the importance of having accurate mechanical properties in the constitutive model is only heightened, when behavior such as plasticity and stress relaxation is observed.

CHAPTER 5: THERMAL CYCLING

Though modeling the behavior of one thermal cycle was an important step in characterizing the hot spot problem, representing the behavior after many thermal cycles was just as important. Actual hot spots in combustor liners see thousands of thermal cycles in their lifetime as engines are repeatedly put to use. Specifically, the effects of plastic hardening can only be seen with additional cycles. What's more, the eventual cracking that has been observed in both liners as well as experimental blister tests only occurs after many thermal cycles are applied.

The blister model was cycled for 11 additional cycles for a total of 12 to stabilize the stress state, monitor the mechanical behavior, and compare the same trends seen in the first cycle. Specifically, the out-of-plane displacement of the model center as well as the evolution of the stress state were of chief concern.

5.1 Modeling Additional Cycles

The same thermocouple data that was used to monitor the blister test and that was eventually incorporated into the applied thermal gradient in the first cycle was repeated for the additional 11 cycles. Because of thermal conduction, additional cycles produced a "hotter" hot spot and, therefore, more intense thermal gradient over the twelve cycles. But because this was not a true thermal conduction model, it was necessary to incorporate this data manually, by delineating each successive heat up with these new temperatures by using the 'BFV' ANSYS command as before. The new thermocouple data was turned into discrete temperatures applied to the annular volume elements.

However, thermocouple data was only acquired every other cycle (on odd cycles). Therefore, the applied thermal gradient was changed every other cycle in the model by using 6 distinct sets of thermal commands that were written by

using 24 different load steps (with four load steps per cycle). In other words, for cycles 1 and 2, the thermal data for cycle one was used and turned into 8 load steps, with cycles 5-8 being identical to cycles 1-4. An average of 40 substeps were used for each load step in order to ensure convergence of the highly nonlinear solution. Table 5.1 lists the center temperature change as recorded by the thermocouple every odd cycle.

Table 5.1 Hot Spot Temperature reached at the blister center at the end of each heat up

Cycle	Hot Spot Temperature	
	°C	°F
1	1069.4	1957
3	1081.1	1978
5	1081.1	1978
7	1088.3	1991
9	1089.4	1993
11	1088.9	1992

Though not shown, the resulting thermal gradient curves for each load step were representative of the curves shown in Fig. 4.3, only each curve was a little higher with a hotter center temperature.

5.2 Results and Validation

There were several sets of results that were important to post-process from the ANSYS solution. The most important data set involved the out-of-plane displacement data as it was the primary means by which the model was validated by the experimental blister test. Additionally, the trends of how the specimen behaved in light of the material properties used was also of value. This section reviews the out-of-plane behavior results with validation, the model

center stress trends with each cycle, and the extent of material nonlinearity throughout the model.

5.2.1 Out-of-plane Behavior

Table 5.1 and Figure 5.1 show the difference between the center out-of-plane displacements over the course of the twelve cycles. The difference for the final, 12th cycle, heat-up is only 0.16 mm, showing a displacement of 3.4 mm for the experiment compared to 3.24 mm for the model. This is only 5% error. The difference between the two increases for the cool-down step over the twelve cycles, with a final displacement of 1.499 mm for the experiment vs. 1.135 mm for the ANSYS model for a difference of 0.364 mm. This is a percent error of 24%.

As a third means of comparison, the total out-of-plane translation (from heat-up to cool-down) was compared over the course of the twelve cycles. This shows a marked improvement, with the difference in translation at the first cycle having 43% error, while narrowing to 10% error by cycle twelve.

Table 5.1 Out-of-plane Displacement Comparison over 12 Cycles

Cycles	Center, Out-of-Plane Displacement (mm)					
	Blister Test			ANSYS Model		
	Heat-up	Cool-Down	Total translation	Heat-up	Cool-Down	Total translation
1	-2.46	-0.84	1.62	-3.06	-0.72	2.34
2	-2.54	-0.97	1.57	-3.07	-0.78	2.29
3	-2.79	-1.07	1.72	-3.24	-0.90	2.34
4	-2.84	-1.17	1.67	-3.26	-0.94	2.32
5	-2.92	-1.17	1.75	-3.22	-0.92	2.3
6	-3.1	-1.32	1.78	-3.23	-1.0	2.23
7	-3.1	-1.34	1.75	-3.31	-1.05	2.26
8	-3.33	-1.35	1.98	-3.32	-1.08	2.23

9	-3.27	-1.45	1.82	-3.25	-1.09	2.16
10	-3.33	-1.47	1.85	-3.26	-1.11	2.15
11	-3.38	-1.50	1.88	-3.23	-1.13	2.1
12	-3.4	-1.5	1.9	-3.24	-1.14	2.1

Among the reasons for difference, it should be noted that the test specimen did experience slight warping in a “saddle-type” shape. This was believed to be caused by asymmetry in the actual experimental heat up. When the specimen was observed following the test, the point of maximum displacement (corresponding to the obvious hot spot from observed oxide) of the specimen was not precisely at the planar center.

The warping effect was only noted at the end of the 12th cycle. It is not known whether this effect was gradual or not over these cycles. Obviously, the ANSYS model was created and loaded in perfect axisymmetry, thus no warping was observed. This could be a source of error in the model representing the blister test accurately.

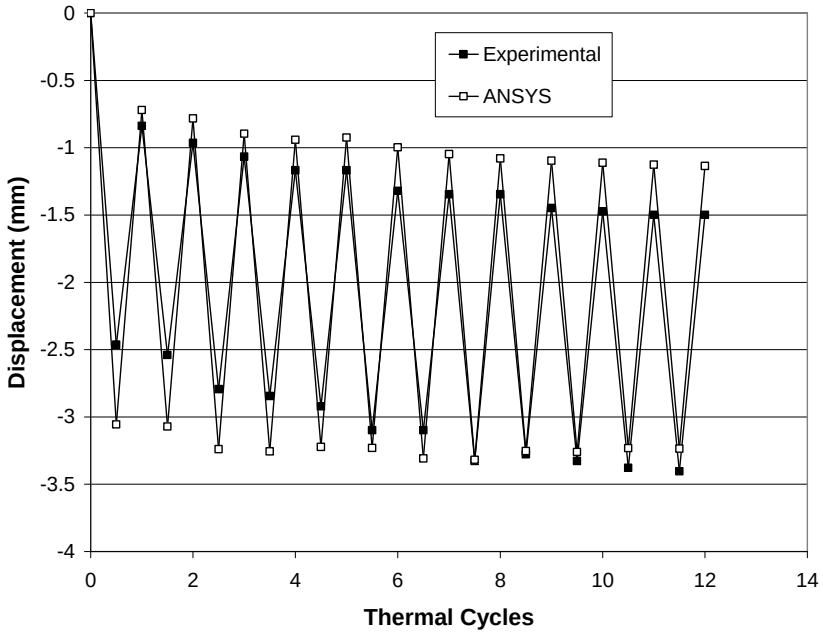

Figure 5.1 Comparison of out-of-plane displacement of the hot spot center of the blister test with the ANSYS model over twelve cycles.

The overall out-of-plane profile was also compared. A dial gage was used on an x-y table and z-displacement measurements were taken every 2.54 mm. Figure 5.2 shows a photo of this test setup, showing the dial gage, specimen, and x-y travel table.

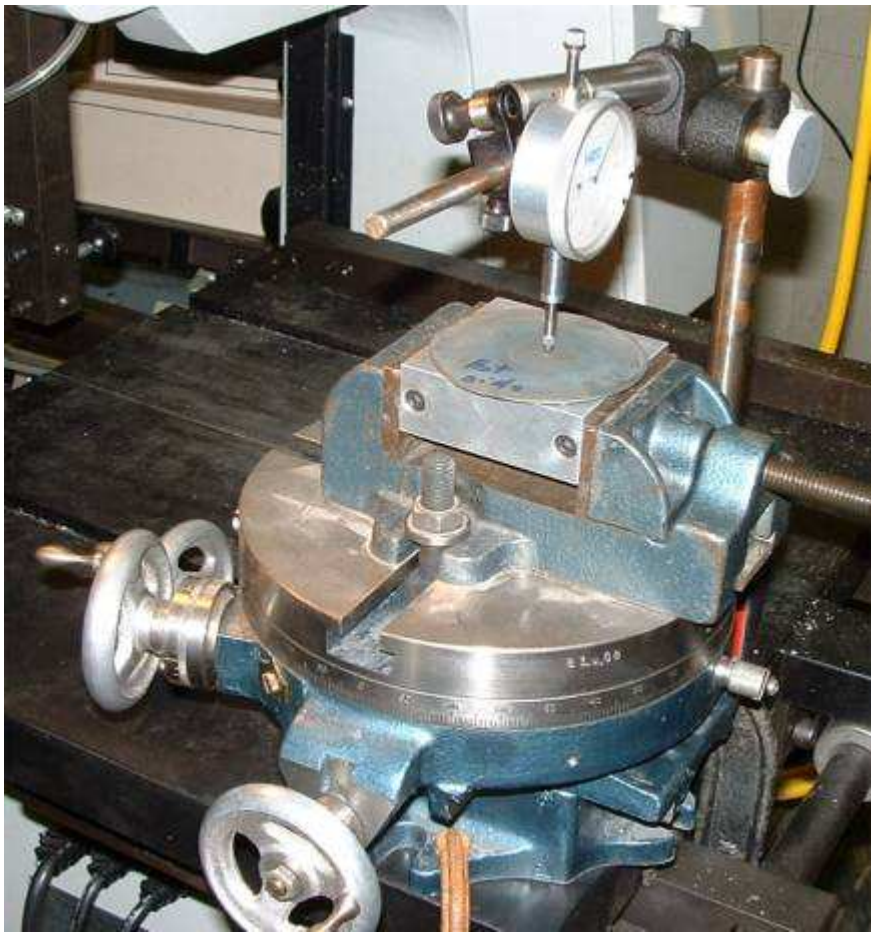

Figure 5.2 X-y table with specimen and dial gage for profile measurements

Figure 5.3 shows the ANSYS profile (which, due to symmetry, is one profile mirrored around the z axis) as compared to both the raw experimental profile and the profile normalized to remove the warping effect. The axes on the graph (though the units are both mm) are on different scales intentionally to magnify the differences. Without warping, the displacement at the center decreases to 1.32 mm, which reduces the difference in comparison to the model to 0.185 mm from 0.364 mm. It is also evident that the model profile shape is

almost identical to the experimental profile, indicating the residual stress field holding the blister in the permanent “blister” is appropriate.

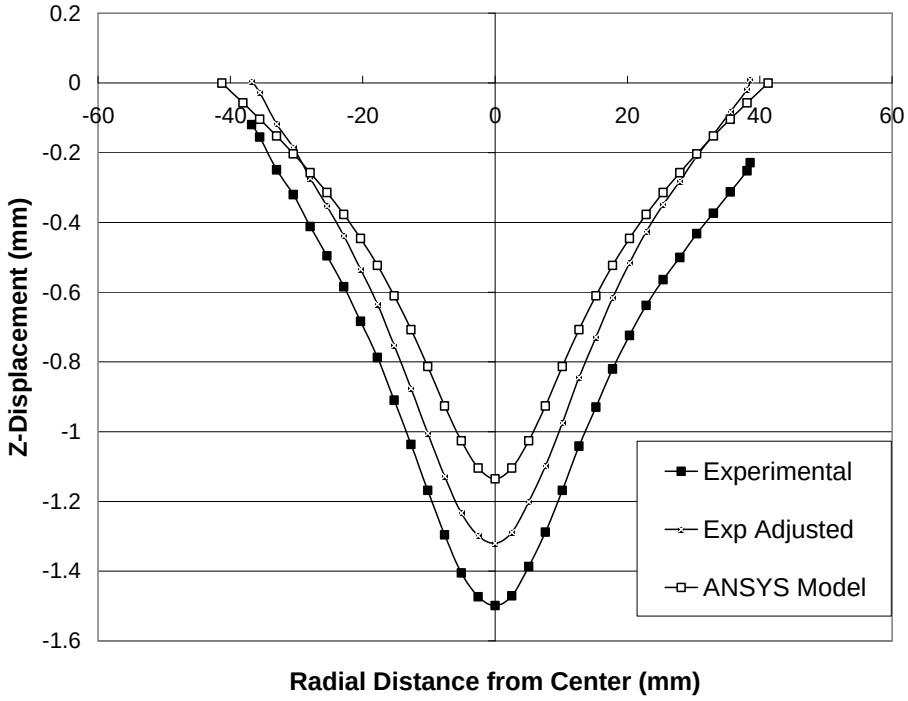

Figure 5.3 Comparison of out-of-plane displacement over the entire specimen of the blister test (both the raw experimental and that adjusted to remove warping) with the ANSYS model after twelve cycles

5.2.2 Stress Changes at the Model Center

Figure 5.4 shows the change in the stress at the hot spot center, at the node at the top surface as well as for the bottom surface for the entire thermal cycle, along with the temperature at the center. The behavior over twelve cycles is shown, however only during the first four and last cycle is the exhaustive data recorded and graphed. This is to keep the results file size to a minimum while still displaying all the important mechanical trends. The stress plotted is technically the stress in the y-direction; however, as was mentioned in Chapter 4, because the two nodes are both at the axisymmetric center, an equal biaxial stress state exists to where $S_y = S_x = S_r = S_\theta$. The initial cycle behavior was

discussed in Chapter 4, with the building radial compression produced the buckling, followed by a divergence in stress as plate bending begins due to the buckled shape. The stresses at the top and bottom node remain separated for the ensuing cycles, alternating between tension and compression with each heat up or cool down. It should be noted that the magnitude of stress, for both the top and bottom node, during heating decreases with each cycle. This is due to stress relaxation and the time-dependent material properties. However, a greater magnitude of stress exists still at the top surface than at the bottom, during both heat-up and cool-down stages from the same combined loading behavior seen in the first cycle. Yet at heat-up, this difference decreases over the course of twelve cycles. This is primarily due to the stress relaxation that continues with each subsequent cycle.

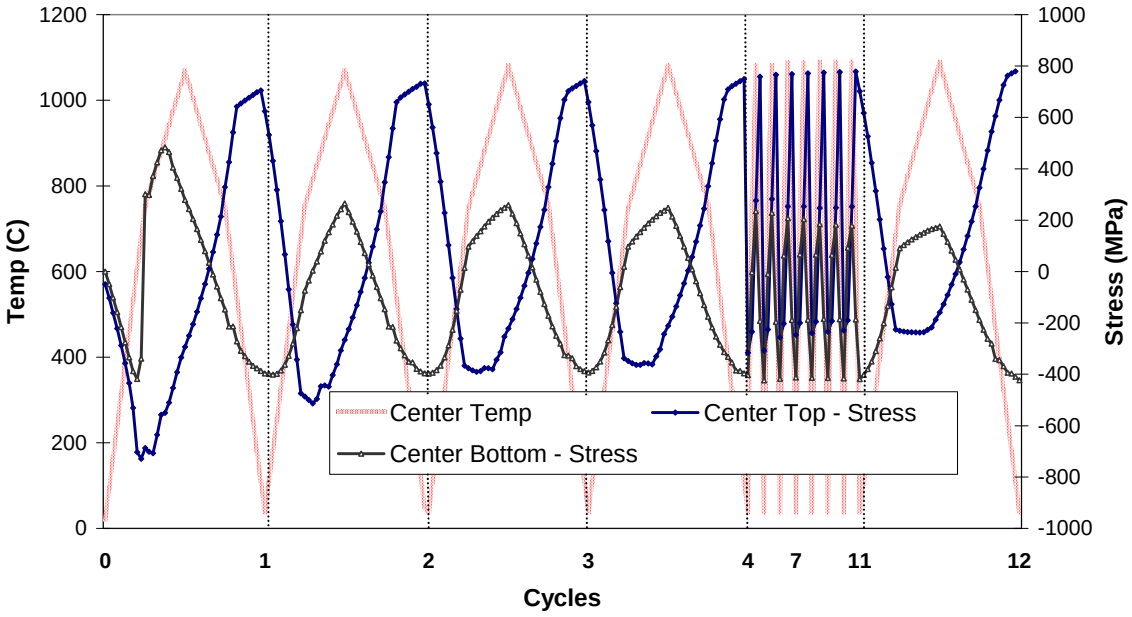

Figure 5.4 ANSYS plot at of the stress at the center of the hot spot (both on the top surface as well as bottom) along with center temperature vs. cycles

Additionally, the tensile stress at cool down at the top node increases with each cycle, due to the Bauschinger Effect and kinematic hardening model used. However, the amount of hardening decreases with each cycle such that the

difference between the stress at the end of the eleventh and twelfth cycles is under 2 MPa.

5.2.3 Extent of Plasticity and Creep

Though it is very clear from Fig 5.4 that significant plasticity and creep occurred at the center of the model, particularly at the top surface, it is important to note the extent of each behavior across a greater section of the quarter-plate model. Figures 5.5 and 5.6 depict graphically the extent of plastic strain from the top side and from an isometric point-of-view, respectively, throughout the model at the end of the 11th cycle. This plastic strain is cumulative over the course of the 11 cycles, therefore residual plasticity from earlier cycles is shown.

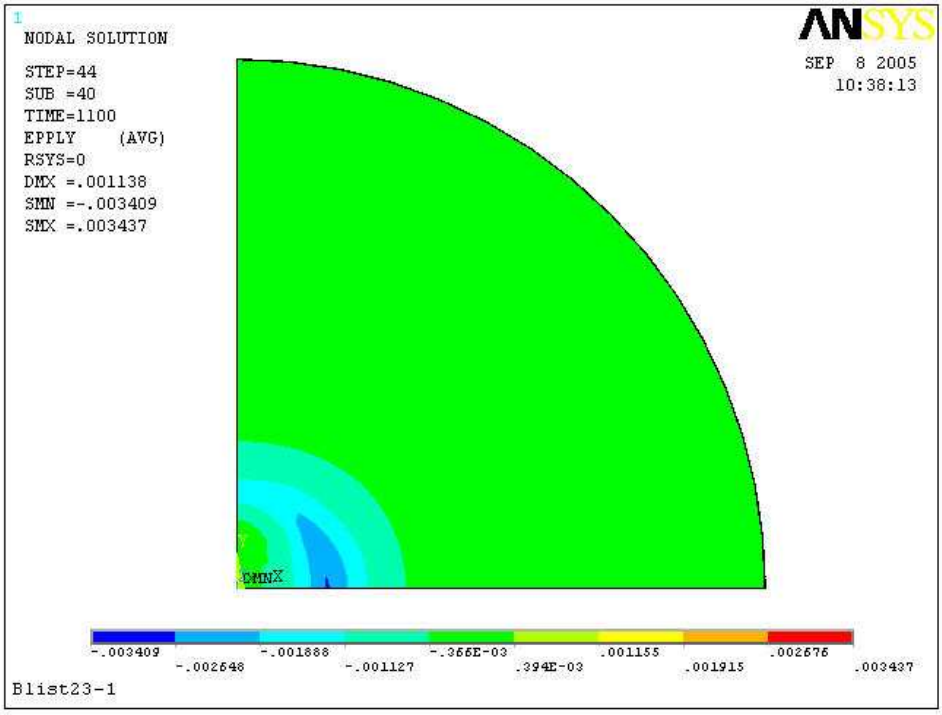

Figure 5.5 Top down ANSYS plot at of the plastic strain (y-direction).

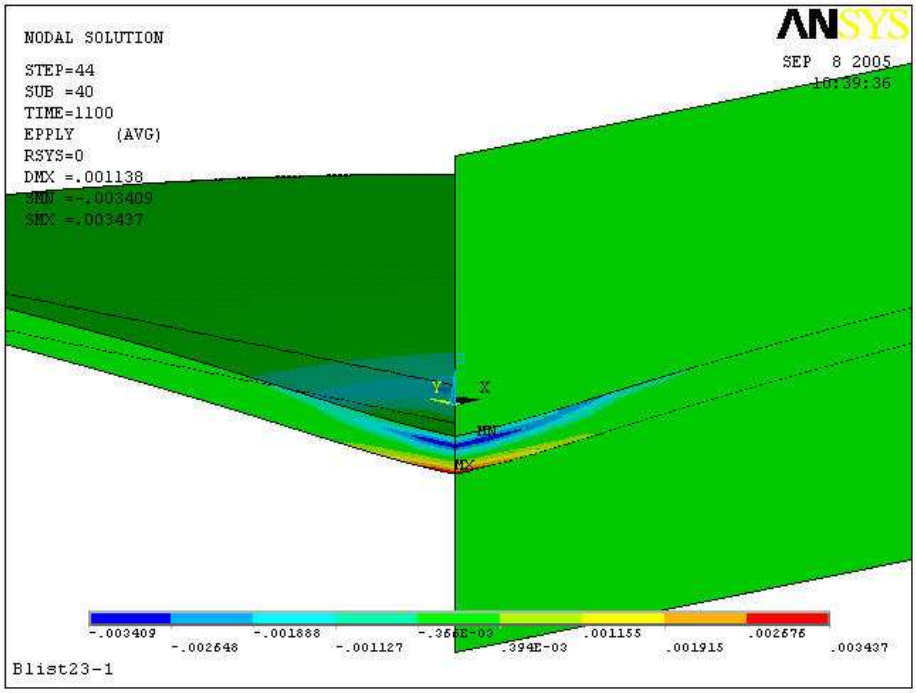

Figure 5.6 Isometric ANSYS plot of the plastic strain (y-direction) in the model

Figure 5.5 shows that the plasticity is limited to a small area of the center of the model, within approximately a 13 mm radius or about a third of the overall specimen. Figure 5.6 shows the same data from an isometric perspective. This view shows the behavior is limited to the outer regions of the surface, with the most plasticity at the surface and no plasticity at the center of the thickness. This indicates the bending behavior is driving the stress distribution throughout the model, particularly at the center where the stresses are highest. What can also be seen from Fig. 5.5 is that the top surface has compressive residual plastic strains while the bottom has tensile strains. Again, each figure shows the results at the end of the 11th cycle, so it is at cool down when the stresses at the center on the top surface are in high tension, while the bottom, center is in high compression. The reason that Fig 5.5 shows the plasticity on the top to be compressive is because the initial plastic strains occurred when the center was at high temperature. At this point the top went in to high compression, while the

bottom went into tension. At cool down, though the stresses reverse direction, the plasticity from the heat up lessens.

However, Fig 5.6 does show that there has been some reduction of that compressive plastic strain at the very top. The max compressive strain is actually within the model thickness. This is because the model center does yield in tension at the top after it cools down, thereby reducing the compressive plastic stain.

Figures 5.7 and 5.8 show the residual creep strain in the model from the same views that the plasticity was shown. And similar trends can be seen. Though these images are at cool down, the residual creep strain was induced when the specimen was at heat up. Compressive creep strain is seen on the top surface in both figures while Fig 5.6 show that the bottom surface has tensile creep strain. So, the permanent strain here gets “locked” in at temperature. What is notable, as compared to the plasticity, is that the amount of compressive creep strain in the top is not reduced from heat-up to cool-down. The reason is somewhat obvious, in that at cool down the temperatures are not hot enough to create the positive creep strain. The other noteworthy observation from Fig. 5.6 is that the creep strain is much more extensive, radially. A greater volume of material experiences creep than plasticity. However, because creep is a function of stress as well as temperature, it is non-uniform through the thickness.

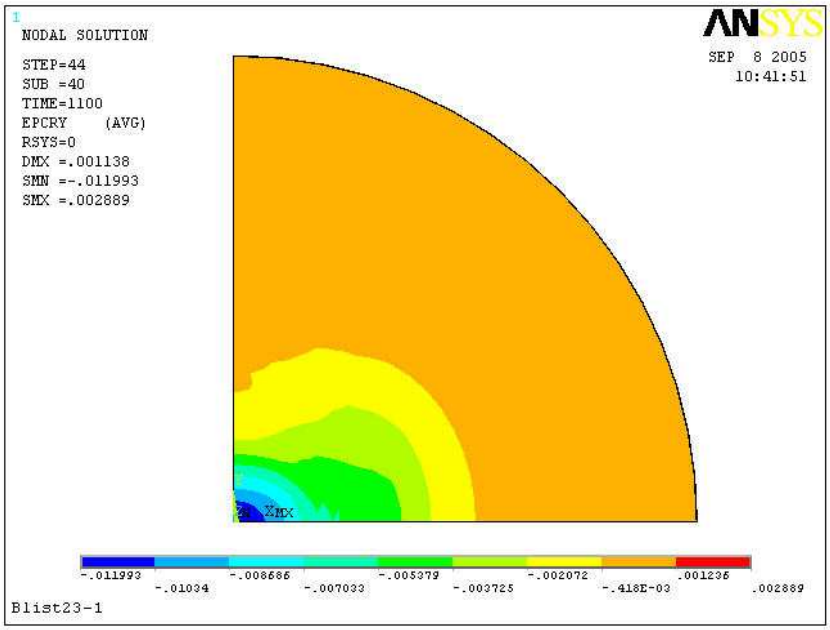

Figure 5.7 Top ANSYS plot at of the creep strain (y-direction) in the model

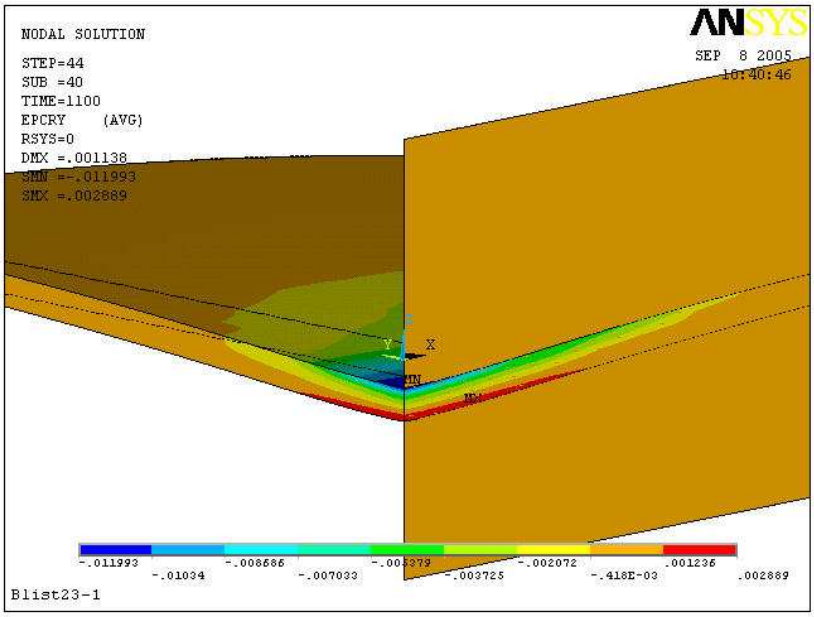

Figure 5.8 Isometric ANSYS plot at of the creep strain (y-direction) in the model

5.3 Conclusions

Some important conclusions can be made from the cyclic behavior of the model that should be highlighted. Aside from the model validity, many important physical trends can be discussed.

- The model represents the experimental specimen behavior within reasonable error during both heat-up and cool-down. The first cycle is within 24% error at heat-up while dropping to 14% at cool-down. This trend is reversed at the end of twelve cycles, with the heat-up error being 5%, while the cool-down was at 24%.

- The overall error in the out-of-plane translation distance (between heat-up and cool-down) improves significantly over the twelve cycles. The initial total translation error is at 42% after the first cycle, but drops to 10% after cycle twelve.

- Though a single-source for error is not known for the difference in out-of-plane displacement, one potentially significant source may lie in the slight saddle-like warping behavior observed in the test article. This warping, perhaps caused by having the hot spot applied just off of geometric center, is not represented in what is a completely axisymmetric model.

- An additional source for error could lie in the changing thermal gradient with each cycle. The experimental test only recorded thermocouple readings on each odd cycle. Therefore, the temperature gradient created from these recordings was repeated for the following even cycle. While the overall temperature change is not great, it would have a direct impact in the displacement response.

- The model characterizes the out-of-plane profile across the specimen diameter very well. With warping effects normalized, the shape is almost identical, showing the blister “bubble-like” shape at the center over the same radial distances.

- The stress behavior at the hot spot center continues the same trends over twelve cycles that were observed in the initial cycle summarized in Chapter

4. The top surface exhibits the higher magnitudes of stress (during both heat-up and cool-down) than the bottom and remain opposite in sign due to the bending behavior. Because of this higher stress magnitude, the top undergoes the most plasticity and creep/stress relaxation behavior.

- Both the plasticity and creep strains are localized toward the center of the specimen. The plasticity is by no means “gross” throughout the specimen, and again is greater at the top. The residual plastic strain at the top is compressive, even after cool-down. This is because the greatest yielding occurs initially in compression at heat-up, but does lessen after reverse-loading occurs when it yields in tension at cool-down.

- The creep strains (though caused actually by stress relaxation) are more pervasive radially across the specimen than the plastic strains, but are still localized toward the center. These strains, of course, occur only at temperature.

- The repeated yielding, particularly at the top surface, does indicate kinematic hardening over each cycle but lessens to only ~2 MPa between the eleventh and twelfth cycle. With such minimal change, the model is believed to have “shaken-down” sufficiently to have assumed the appropriate stress/strain state of the actual test article before crack modeling.

CHAPTER 6: CRACK GROWTH MODELING

This chapter chronicles how a growing crack is modeled in the ANSYS program after a given amount of thermal cycling has taken place. How a crack is inserted, extended (or grown), and characterized by stress intensities are all discussed before comparisons are made to the experimental blister specimen crack behavior, specifically the distance and thermal cycle number at which the crack is believed to arrest.

6.1 Crack Insertion

As has been mentioned, the thermal cycling of the hot spots, whether in actual combustor liners or blister tests, eventually induces fatigue crack growth. In order to incorporate the plasticity, hardening, and relaxation of a thermally cycled specimen, the model is cycled twelve times before the initial crack length was created. This cycle number is, as we shall see in Section 6.4, around an order of magnitude short of the true number of cycles a normal blister experiment is cycled before a visible, measurable crack appears. However, based on how the maximum stresses at the hot spot center have leveled off after twelve cycles (See Fig 5.3), the mechanical behavior is believed to have stabilized. Therefore, increasing the number of cycles beyond these twelve cycles only greatly increases run time for what would be a fairly insignificant change in stresses and plastic strain that would affect fracture analysis.

In order to model such behavior, determining to what extent (or length) and what shape the crack is first inserted can become important. The term insertion is chosen carefully, as the model is intended to not to predict true crack initiation behavior. The goal of the model is to represent the “evolving” K distribution at varying crack lengths from the center through the edge of the hot spot. Therefore, the somewhat arbitrary initial crack length is 0.635 mm, which is the radial length of the brick element used throughout the mesh.

The basic means by which a crack is modeled for this analysis is by removing the symmetry boundary condition along the x-z plane of the model at cool down. Figure 6.1 depicts a schematic of the center of the quarter-plate with a 3-D axis system. However, in order for this method to work for our model, modifications must be made to account for the bending occurring through the thickness, particularly at the center of the model as seen in Figures 6.2 and 6.3.

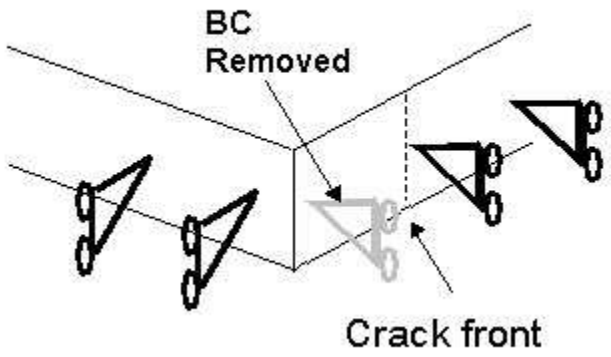

Figure 6.1 Schematic of crack insertion by removing the symmetry boundary condition along the x-z plane of the mesh.

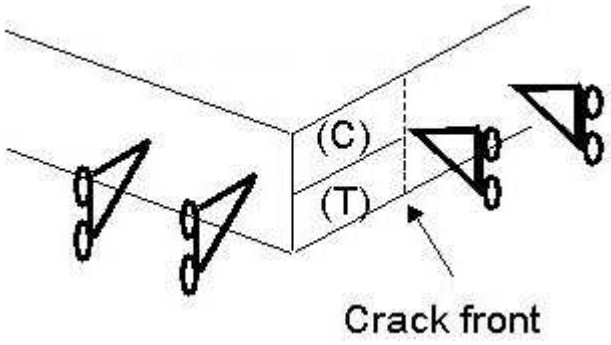

Figure 6.2 Schematic of crack insertion at the beginning of the cool-down by when the top surface is in compression, while the bottom is in tension along the x-z plane of the mesh.

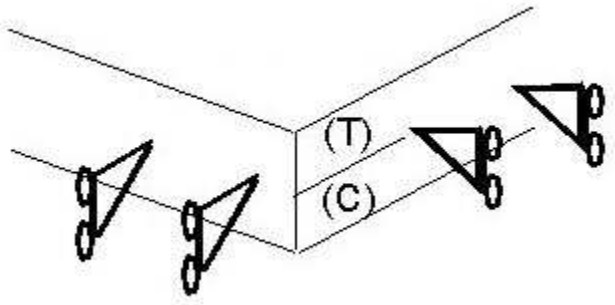

Figure 6.3 Schematic of crack face at the end of the cool-down by when the top surface is in tension, while the bottom is in compression along the x-z plane of the mesh.

When the symmetry boundary condition is removed, the elements along that respective edge are free to move, either away from or towards the symmetry plane depending on whether the elements along those locations are in either tension or compression, respectively. If the psuedo-crack face moves away from the symmetry plane as a result of the loading, there is no problem. The crack would merely be opened along the crack face. This is the case for the bottom of the model at heat-up (Fig 6.2) or the top at cool down (Fig. 6.3). However, if elements at this location are in compression, a fictional “penetration” of the symmetry boundary occurs as the elements are trying to “expand” beyond this boundary. Such a model no longer can be considered valid.

In order to prevent this penetration from occurring, a plane of contact elements has been introduced along the x-z plane of the model. The contact plane (as shown in Fig. 6.4) consists of 9, 4-noded quadrilateral elements which extend to 40 mm along the radius (x-direction) and 10 mm in both the positive and negative z (or out-of-plane) direction. The contact plane is separated 0.0001 mm from the quarter-plate.

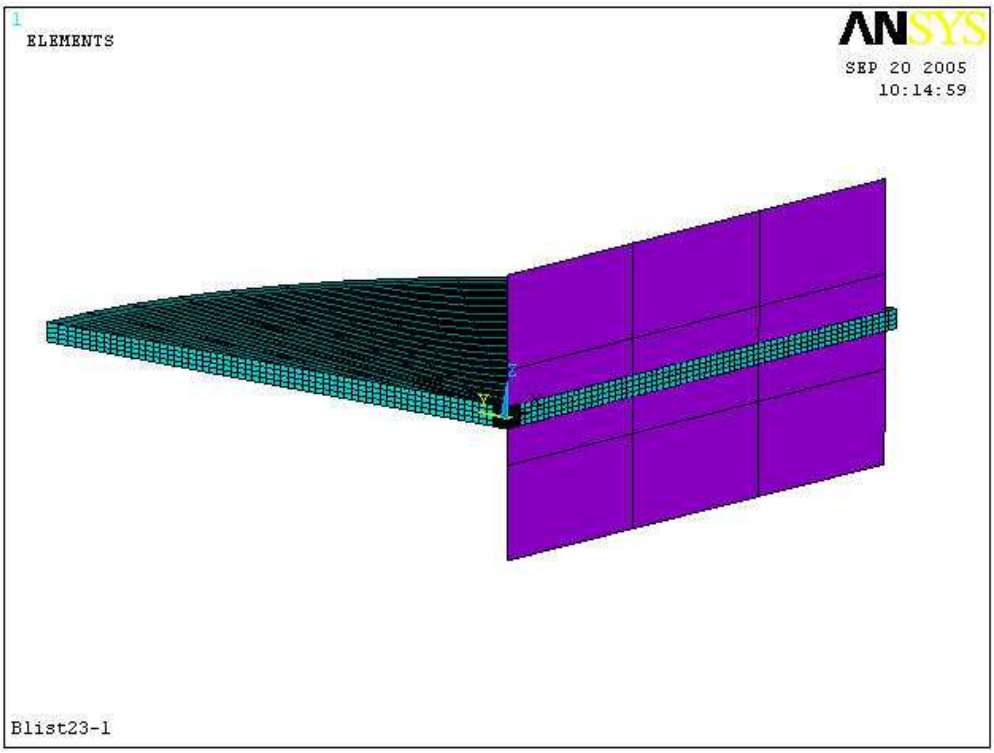

Figure 6.4 Isometric view of ANSYS model showing nine contact plane elements used to prevent penetration of the crack face elements during thermal cycling.

The contact plane was extended in both positive and negative z-directions in order to prevent symmetry penetration as the blister model moves out-of-plane as it thermally cycles. A default contact stiffness factor (FKN) of 1.0 was used, resulting in an actual contact stiffness of 24.9 MPa. The ANSYS default penetration factor (FTOLN) was also used, resulting in a penetration tolerance of 0.0159 mm for the gauss points of each element. The plane was given a frictionless contact coefficient in order to prevent unrealistic shear stresses along the crack face as the model cycles in and out-of-plane. While the actual blister specimen is expected to have friction between the crack faces when in contact, both faces are expected to be moving in and out-of-plane mirroring one another. Therefore, a minimal (if not negligible) amount of relative displacement between the faces is expected. If a non-zero friction coefficient is chosen, significant shear stresses will result as the contact plane is stationary, while the quarter-

plate is free to move in the z-direction. In other words, because the contact pair does not “mirror” each other as the model thermally cycles, an unrealistic friction would develop if it is not assumed to be a frictionless contact.

With the contact element plane in place, the symmetry boundary condition could be removed. As mentioned, an initial crack length of 0.635 mm was chosen, somewhat arbitrarily. It was chosen to be a thru crack. As will be noted in the experimental blister results, the initial crack length observed on the positive z-face is ~5 mm. However, in order to ensure solution convergence, the initial crack length and subsequent extension increments are all chosen to be 0.635 mm. Removing significantly greater portions of the symmetry boundary condition (> ~2mm) at one time or at one load step consistently resulted in an unconverged solution.

In order to remove the constraint, the same load step files used to thermally cycle the model were used, except for one major difference: the y-constraint “D, NODE, UY, 0” was removed from the file for every node that corresponded to a node that should be on the new crack face. This was done only over the two cool down steps of the thirteenth thermal cycle. Figure 6.5 shows the center of the model at heat up just before the symmetry conditions are removed for cycle 13, with the element stress contours being in the y-direction or normal to the contact plane. The compressive stresses at the top surface and tensile stresses at the bottom surface can be seen. Figure 6.6 shows the same region at cool down of that cycle with the resulting stress contours showing the compressive stresses at the bottom and tensile stresses at the top. The crack front can be clearly seen where the restraint triangles begin along the right side.

It should be noted that while the majority of the model brick elements have a radial dimension of 0.635 mm, both Figures 6.5 and 6.6 show a higher concentration of much smaller elements at the center of the model. These elements were created at this size automatically by the mesh generator for the smaller volume at the model center to ensure a more reasonable aspect ratio. Again, while it is unlikely a thru-crack of this size is realistic for an initial crack

length, it provides a means by which gradual extension can occur; as a reasonable, representative crack length can be created.

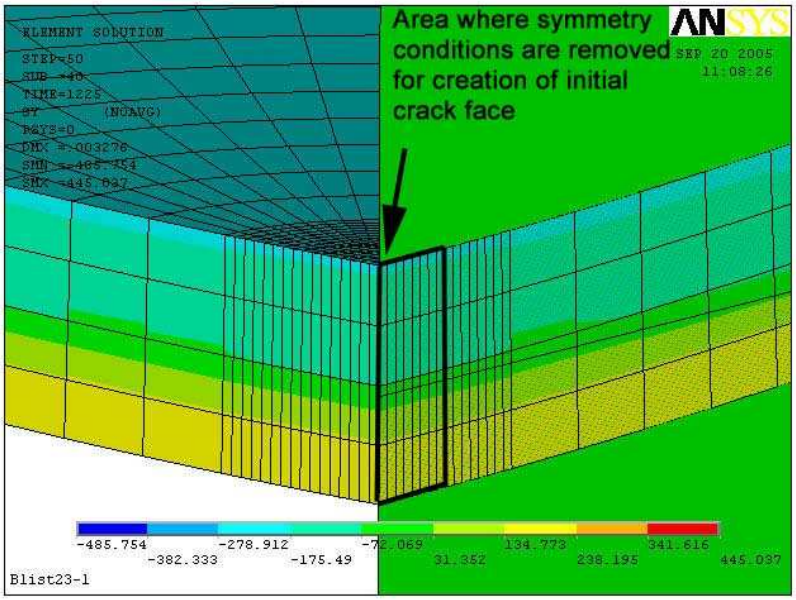

Figure 6.5 Isometric view of ANSYS model just before crack "insertion" showing the y-stress distribution at the would be crack face.

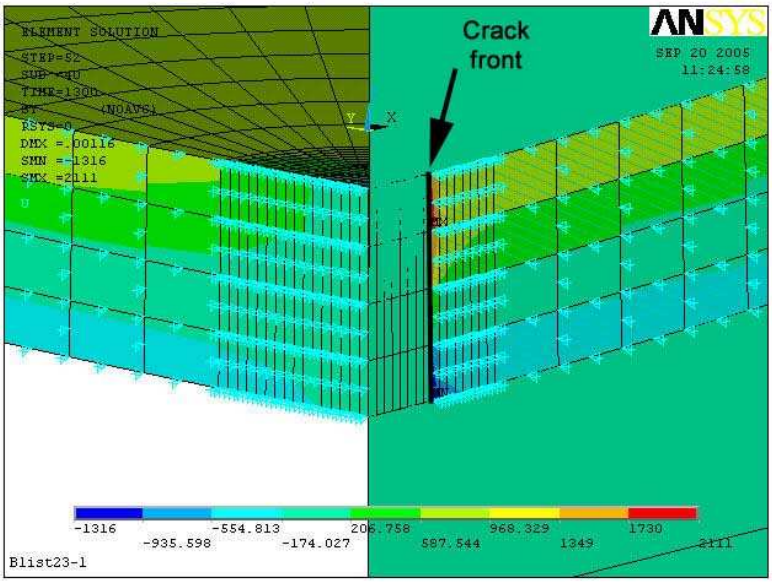

Figure 6.6 Isometric view of ANSYS model at cool down after crack "insertion" showing the y-stress distribution.

The reason the cracks are “inserted” at the beginning of cool down is to allow the top side to open during this part of the thermal cycle. At the end of cool down, the top, concave side experiences the highest tensile stresses during the uncracked cycles. It is believed that the stresses on this side at this point in each cycle will contribute the most towards the extension of a thru-crack across the radius.

6.2 Crack Extension

To extend the crack along the radial, x-direction, additional y-restraints were removed along the entire thickness, leaving the crack front as a straight thru-crack. The y-restraints were removed every 0.635 mm of the x-direction each thermal cycle. As was done for the initial crack length, the restraints were removed for the two cool-down load steps per thermal cycle. This removal of the restraints simulated crack growth at a constant rate of 0.635 mm per cycle. While this is a relatively fast rate (high by ~10x as will be seen), the intent was not to model true crack growth, but to determine the stress intensity for each crack length radially across the model. In order to model true crack growth, element size along the x-z plane would have had to be reduced in size by at least 10, which would have greatly increased mesh size and therefore the necessary solution time.

The normal number of substeps used per load step was 40, given 80 substeps for both heat-up and cool-down. At crack extension number 25, once the crack length reached 15.8 mm, 10 additional substeps were needed in the third load step for each thermal cycle. Because this is the load step at which the restraints are removed, an increasing number of substeps were needed to ensure convergence as the crack length was extended. The longer the crack becomes, the greater the displacements, and thus the need for smaller substeps for solution convergence.

6.3 Determining Stress Intensity Factors

At the end of each thermal cycle and crack extension, load and displacement data was recorded in order to estimate the stress intensity factors across the model. As discussed in section 2.3.3, there are basically two different means by which stress intensities are determined in an FEA program: direct and indirect. Because the current model possesses material nonlinearity (plasticity), ANSYS cannot directly compute the stress intensity for a given solution. ANSYS requires that only linear elastic material properties are present to calculate the stress intensity factor, K. However, as was determined in section 5.2, the extent of plasticity was not pervasive throughout the model, but rather limited to the center. Therefore, LEFM can be assumed for a crack in our model. Furthermore, the stress intensity will be calculated at room temperature, since that is the point in the thermal cycle at which tensile stresses are highest. Therefore, K was determined to be valid, although it had to be determined indirectly.

6.3.1 Element Crack Front Behavior

In order to determine the stress intensity K, a detailed analysis of the loads and displacements around the crack tip or 3-D crack front was important. Specifically, the normal loads were needed in the area of restraint ahead of the front, while the normal displacements were needed along the crack face itself. A schematic of a sample section of elements at the model center at the end of cool-down is shown in Figure 6.7. Because the highest tensile stresses occur at the top surface at cool-down it was determined that the pertinent stress intensity data should be determined there. With four elements through the thickness, the top two element sections along the crack front are the most critical. The four elements in the top half that surround the crack front are shown and labeled in Figure 6.7. The figure also depicts the typical, qualitative y-direction displacement of the elements in the crack face region at the end of cool-down.

The top section has “pulled-away” from the symmetry plane while the bottom has “pushed-against” the contact plane region along the bottom. The crosshatched region is a representative portion of the elements that make contact with the plane.

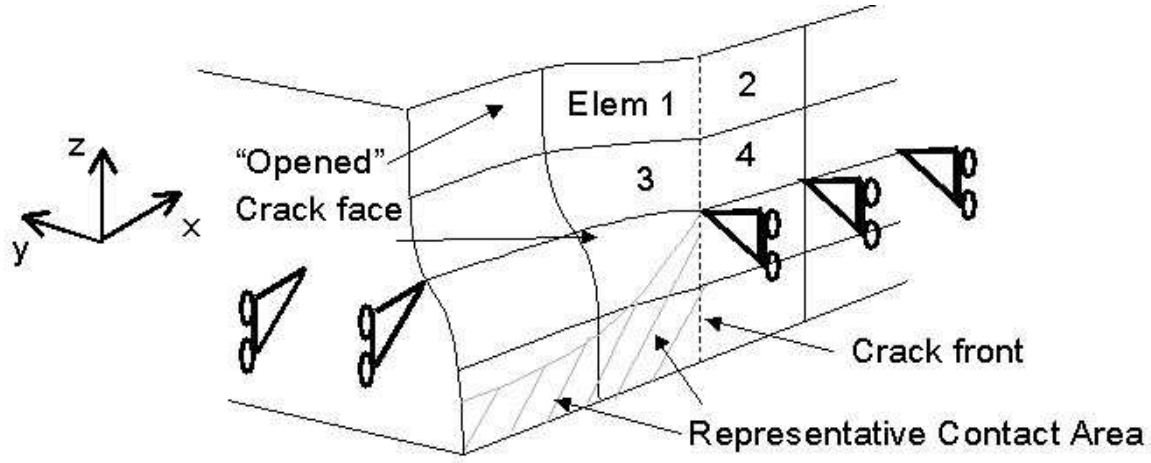

Figure 6.7 Isometric schematic of the center of the model at cool down after crack extension showing the normal displacement of elements along the crack face.

Data from the four elements noted in Figure 6.7 were recorded for each thermal cycle and thus each increment of crack extension. Specifically, data was recorded in order to approximate either J or K. Using 20-noded brick elements, with basic structural displacement degrees-of-freedom in the x-, y-, and z-directions, the resultant nodal loads in the y-direction were recorded for the elements ahead of the crack tip (elements 2 an 4), and the resultant nodal displacements in the y-direction for the elements along the crack face (elements 1 and 3). With each subsequent cycle, and thereby each increment of crack extension, the representative elements 1-4 shift with the crack front and the data is recorded again.

6.3.2 Determining J

Because K cannot be directly determined, it must be calculated by some indirect means. Since we have assumed that the amount of plasticity in the

model isn't "gross" and the model is at room temperature, LEFM is assumed to still be valid. This means that one method for approximating K is to use the J-integral.

But, we still need to be able to determine J from the model in order to approximate K in this way. We learned from Wellman [93] and Dodd's [94, 96] work that equation 2.9 could approximate J experimentally and through FEA with CTOD, the flow stress, and a state of stress estimator, m. Using equation 2.9, the CTOD can be estimated from the model by using the node in the crack wake nearest the crack front, finding its displacement in the y-direction for a given crack increment, and multiplying it by 2. Figure 6.8 shows a schematic of the top section of the thickness and the four elements and their nodes across the crack front. To estimate J using this method, the CTOD at crack front node B is found by finding the displacement in the y-direction at node d. For estimating the J at node C, the displacement at node e is used, and so on.

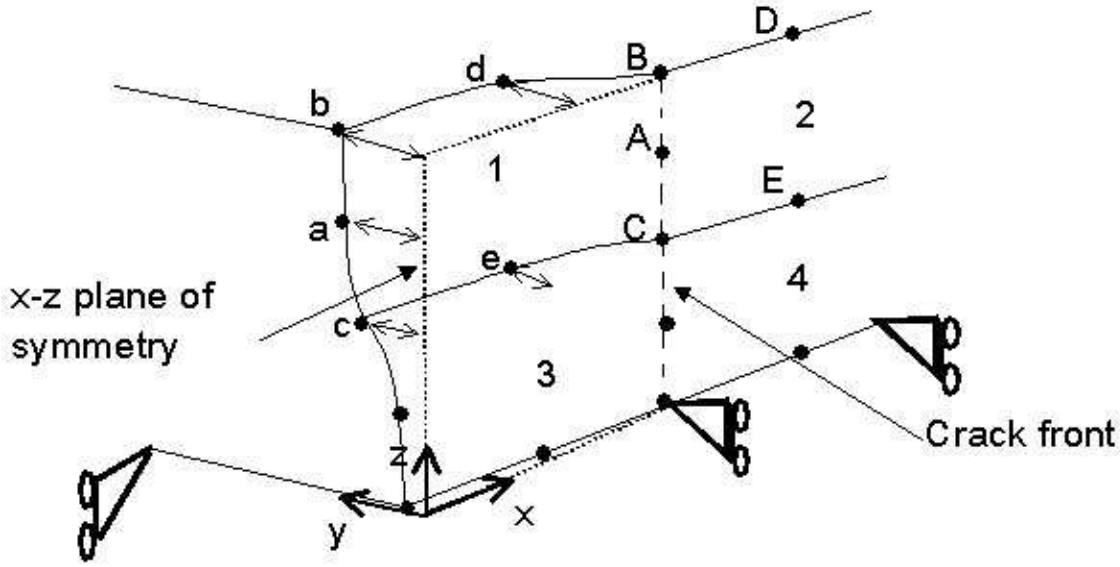

Figure 6.8 Isometric schematic of the top four elements that straddle the crack front at cool down for a given crack increment showing the normal displacement of nodes along the crack face.

The σ_{flow} needed for equation 2.9 is an average of the ultimate and .2% yield strength of a given material. Because the crack face is opening the

greatest when it is at lower, cool-down temperatures, the room temperature values for the two strengths are used for the flow stress estimate.

The state of stress term, m, fluctuates as to whether the location is deemed to be in a state of either plane stress or plane strain. Wellman et al. [116] stated that in general, m ranges between 1 and 2, depending on whether the material is in plane stress or plane strain, respectively. However, he and colleagues [93] went on to show that for three-point bend specimens with a range of thicknesses and materials, each experiencing elastic-plastic behavior, the range is closer to being from 1.2 to 1.6 for FEA. With these numbers in mind, the current application must be analyzed as to the appropriate state of stress. When analyzing the topmost outside node (node B) for a given crack front, one can assume a complete state of plane stress exists. Therefore when calculating the J at this node, both 1 and 1.2 were used as this appears to be the range for plane stress constraint based on the Wellman publications. However, the J at node C was also recorded for a given crack length. Node C, being between the two "upper" elements of the total four elements through the thickness, is always ¾ of the way through the thickness. A complete state of plane strain is typically found at the center of extremely thick specimens. For the current model, the location is not at the center of a not-so thick (1.5 mm) component. Therefore, a range of 1.15 to 1.4 was determined as a range from the least possible constraint and most possible constraint, respectively. Were it a thick specimen and at the center, 1.6 – 2.0 would be the estimated range based on the publications. However, the value would not be expected to be so high for such a thin material.

Once J is determined for the appropriate nodes at a given crack length, the crack extends after an additional thermal cycle, and the appropriate "new" nodes d and e are used to estimate the new J values at the new B and C locations. J is then determined at these two locations for every increment of crack extenstion. From J values for each crack length, K is determined.

6.3.3 Determining K

Two means of determining K were developed for a given modeled crack length. Because of the number of assumptions used for calculation by J, it was important to have a separate, proven means of approximating K to ensure that all the values are "ballpark" for the given application. This section reviews each method.

6.3.3.1 K from J

In order to determine K from the J found as stated in Section 6.3.2, Equation 6.1 was used. With this relationship, K can be approximated from J, assuming E' is E for plane stress and is $E/(1-\nu^2)$ for plane strain. Plane stress was assumed for each J to K conversion as the material is so thin.

[6.1] $$J = \frac{K^2}{E'}$$

As was the case in calculating the flow stress for J, the room temperature material properties (in this case, E) are used for the K calculation. The crack opening on the top side at cool down would reflect room temperature behavior.

6.3.3.2 K using DCCI

R. Singh et al. [88] developed the decomposed crack closure integral (DCCI) (as discussed in section 2.3.3.2) whereby K can be determined across a crack front at various nodes. To do so, equation 2.8 was given as the mean value of K across that front, taking 5 y-displacements at the crack face and 5 nodal loads ahead of the crack for a given crack increment. Specifically, according to Fig. 6.7, the mean K across B-A-C can be found by determining the loads in the y-direction at nodes A-E and the y-direction displacements at nodes a-e. This mean value for K was found at this respective location for each crack length across the model.

The DCCI method does assume strict linear elasticity. While true LEFM does incorporate some limited plasticity in a component, DCCI does not. However, since all materials experience some plasticity at the crack tip (even if very small) and the DCCI method compares favorably to experimental data, we assume it to be within a "ballpark" estimate of the stress intensity across the model.

It should be noted that each method for producing K, whether from J or DCCI, specifically produces K_I, only. Mixed mode behavior does not exist since neither a shearing nor a tearing at the crack faces occurs in the test article. However, it is also important to note that the K from either method is actually a K_{eff}. Since the K calculated is always determined using the opening displacement, the value would be 0 when the crack is closed. Therefore, each maximum value of K is truly an opening K or K_{eff}.

6.4 Results and Validation

This section surveys the results of the stress intensity solutions as represented by the ANSYS blister model. However, before presenting the FEA results, the experimental blister test and subsequent results will be discussed. After both are presented, the viability of a predictable crack arrest length will be presented based on the current investigation as well as published da/dN vs. K_{eff} data. Finally, analysis of the final fracture surface will be discussed.

6.4.1 Experimental Blister FCG Results

The same blister specimen that was thermally fatigued for twelve cycles was cycled an additional 450 cycles for a total of 462 cycles. Temperature gradient data was not acquired as discussed in Chapters 4 and 5. However, manual detection of thermal fatigue induced crack growth was monitored and crude fatigue crack growth data was acquired.

6.4.1.1 Crack Growth Data

As the blister specimen was being cycled (~100 seconds per cycle or 0.01 Hz) it was inspected intermittently at the top (non-flame side) surface with the naked eye for evidence of thermal fatigue cracking. Historically, similar tests as well as actual combustor liner inspections indicated such loading results in very low-cycle fatigue (LCF). At total cycle number 130, no cracks were visible. By cycle 170, a three-way crack pattern was clearly evident by the naked eye and a rough measurement was taken to estimate the distances of each of the three cracks. Fig. 6.9 shows a schematic of the thru-crack pattern, with each tip labeled with its respective distance measured from the vertex of the three cracks. As is shown, each crack length is between 5-6 mm, measured with dial calipers to the nearest thousandth of an inch and then converted here into mm. However, the measurement was considered crude in that it wasn't removed from the test stand in order to be as accurate as possible. The reason for this was to not risk placing the specimen back on the test stand in a slightly different location, which would cause the hot spot to be in a different location than previously tested.

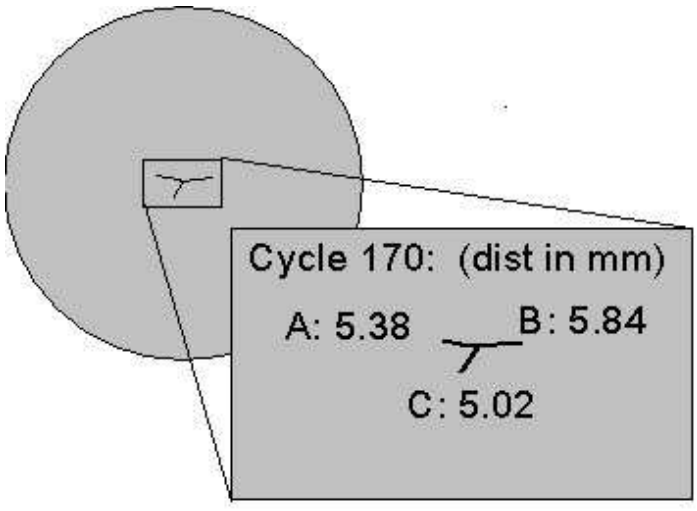

Figure 6.9 Schematic of the initial crack pattern (all thru cracks) and respective distances of the blister test specimen after 170 thermal cycles. Crack lengths measured from the vertex of the three crack branches.

Schematics are shown in Figures 6.10-6.12 for three other distinct periods in the test showing the growth at each respective cycle. In Figure 6.12, a range of cycles between 365 and 462 cycles is shown in order to indicate that no measurable difference was detected. The test ceased at 462 cycles. The raw data for the crack measurement per cycle is shown in Table 6.1.

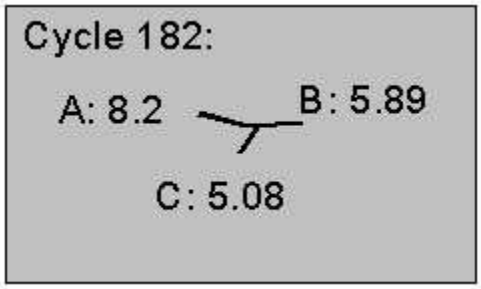

Figure 6.10 Schematic of the crack pattern distances of the blister test specimen after 182 thermal cycles. Crack lengths measured from the vertex of the three crack branches.

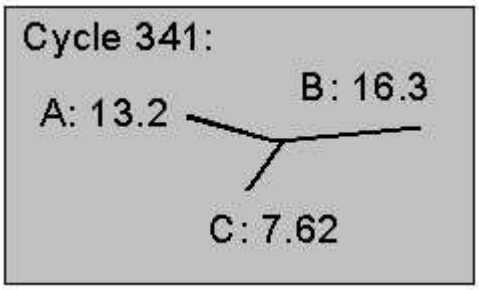

Figure 6.11 Schematic of the crack pattern distances of the blister test specimen after 182 thermal cycles. Crack lengths measured from the vertex of the three crack branches.

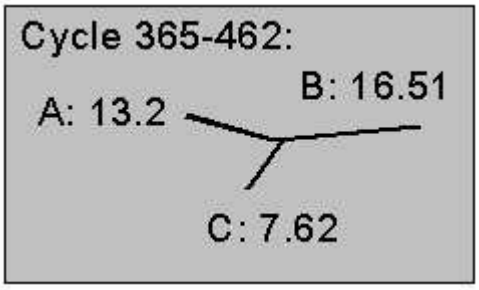

Figure 6.12 Schematic of the crack pattern distances of the blister test specimen after 182 thermal cycles. Crack lengths measured from the vertex of the three crack branches.

Table 6.1 Raw crack data from the blister test specimen

Cycle #	Crack length (mm)		
	A	B	C
130	0	0	0
170	5.3848	5.842	5.0292
178	5.7404	5.842	5.0292
182	8.2042	5.8928	5.08
197	9.4234	Not available (NA)	NA
207	11.5824	NA	NA
219	11.7856	NA	NA
231	12.4968	NA	NA
241	12.4968	NA	NA
255	12.4968	NA	NA
292	13.716	NA	NA
307	13.716	NA	7.9756
341	13.208	16.3068	7.62
365	13.208	16.51	7.62
462	13.208	16.51	7.62

What can be noted, particularly from Table 6.1, is evidence of the "crudeness" of the measurements. This can be seen in the measurement difference between cycles 307 and 341 of cracks A and C. In both cases, the crack length is measured to be actually shorter at cycle 341 than at cycle 307. While a possible alternative explanation is that the crack may have closed somewhat at branches A and C due to the extension of B, it is more likely that there was error in the measurement. However, taking this as an initial, rough error measurement, one can assume the crack length is recorded within the nearest 0.5 mm of accuracy. (Note: Though the values of the crack measurements were taken in inches to the nearest thousandth of an inch and are shown here, converted to the nearest 1e-4 mm. The accuracy of the caliper belies the accuracy of the measurements reported in Table 6.1.)

The crack length measurements between cycles 197 and 292 were not recorded for cracks B and C, but are shown for crack A. The average crack growth rate for crack A between cycle 170 and 231 is 1.72e-4 m/cycle, however there is a standard deviation of 2.28e-4 m/cycle.

6.4.1.2 Post-test Specimen Inspection

Once the final thermal cycle was applied at cycle 462, the specimen was inspected and measured in a more detailed manner. The specimen was first photographed, with both a camera with a macro setting for an overall specimen view, but also under a Leica MZ6 imaging microscope. Using the microscope, images were made of both the top surface and the bottom surface, which was the flame side. Figures 6.13 and 6.14 are composite images of the top and bottom surfaces, respectively, showing the overall crack pattern.

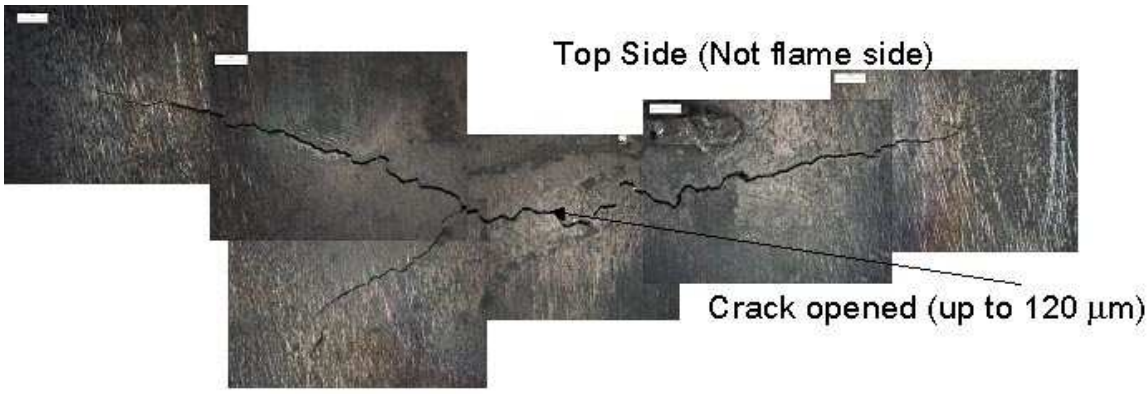

Figure 6.13 Microscope composite image of the top surface of the blister specimen, showing the overall crack pattern.

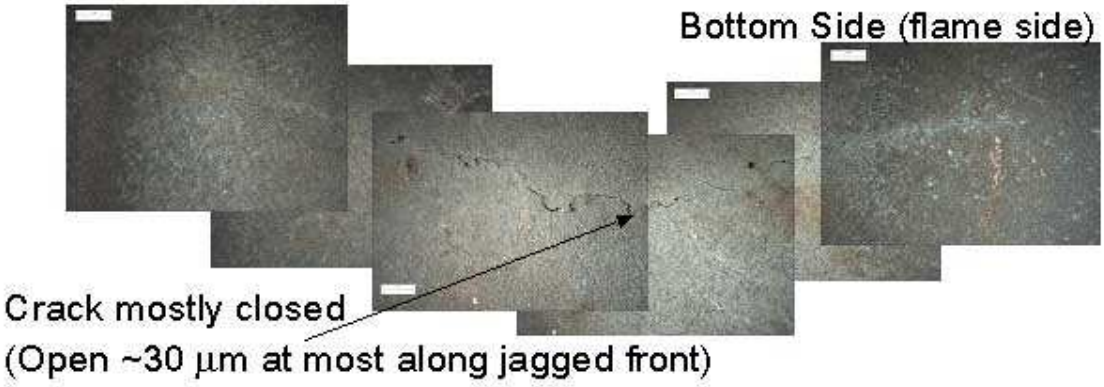

Figure 6.14 Microscope composite image of the bottom (flame-side) surface of the blister specimen, showing the overall crack pattern.

What is initially evident from these figures is that the thru crack as evidenced on the specimen's top side is distinctively opened to a much greater degree then on the bottom side. The crack face is open as much as 120 μm in the center area of the crack region on the top. However, on the bottom side, while the thru crack is obvious, it is only opened as much as 30 μm in some locations, but is mostly closed. The open areas seen along the areas the crack path are most jagged, where the surface irregularity appears to be preventing

crack closure. This validates the bending behavior depicted in the model. The blister model exhibits tensile behavior on the bottom surface and compressive behavior at the top while at high temperature, with the opposite behavior at room temperature. Obviously at room temperature, the specimen shows a clear state of tensile behavior, with an opened crack, at the top surface while the bottom crack face is in compression.

Also evident from post-test inspection is a significant amount of oxide build-up on the bottom side, with most of the oxide in the center of the specimen. This, too, has an obvious cause, being the side and location that was closest to the flame.

The crack lengths were again measured, this time digitally with a cursor under the microscope. Because human error can still be a factor, three measurements were made per crack length, per side. The final measured average lengths with standard deviations are listed in Table 6.2. Again, the distances were measured from the vertex of the three branches.

Table 6.2 Average final crack lengths for the three crack branches, with standard deviations, as measured on both the top and bottom surfaces of the blister specimen

	Top Side		Bottom Side	
Crack Branch	Avg. Length (mm)	Standard Deviation (mm)	Avg. Length (mm)	Standard Deviation (mm)
A	14.43	0.048	13.64	0.05
B	20.32	0.054	20.09	0.08
C	7.48	0.04	7.55	0.10

With these final measurements, the major crack branches A and B were deemed to be the major thru crack of the specimen with a total distance of A + B (2a) of 34.75 mm on the top side. While the two branches, A and B, are not the same length, it should be noted again that the blister specimen center was not collocated with the center of the applied flame. However, since the model is approximating a quarter-plate and therefore axisymmetric, an average final crack

length of half of 2a is a reasonable estimate for model comparison with the test article. This average, a length of 17.4 mm, is then the average final crack length. Using an average initial crack length of 5.5 mm for the same two branches, we can state that for this particular test, the crack grew from 5.5 to 17.4 mm in 195 cycles. This serves as an important comparison and validation for the following sections, wherein the model's fatigue crack growth is estimated.

6.4.2 K vs. a Results for FEA Model

As stated in section 6.3, K was determined two different ways for each crack extension in the model, using the J and DCCI method and that each K is actually a K_{eff}. With the four K's calculated from four J's (two at the top node with m's of two separate values; two at the ¾ node thru the thickness with two separate m values), as well as the one K trend using DCCI, a range of K's can be seen for crack lengths from 0.635 mm out to 29.21 mm in Figure 6.15, with a crack extension every 0.635 mm.

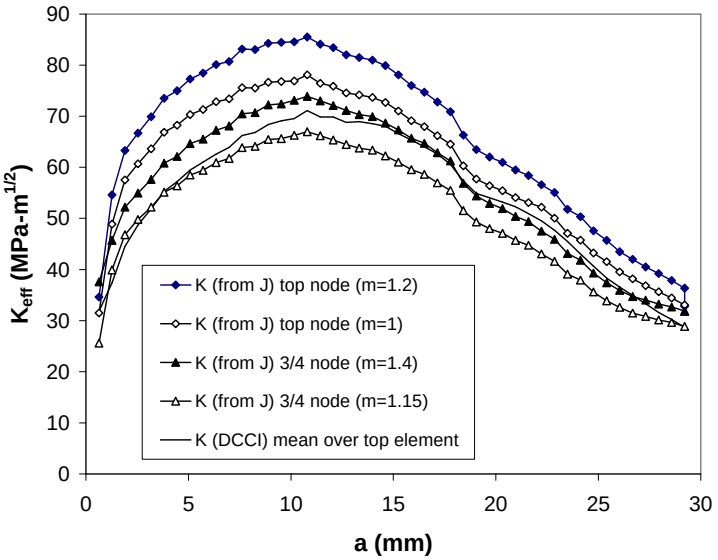

Figure 6.15 K vs. a curve for 5 separate estimates of K.

Qualitatively, every curve shows the same trend, being a steady increase from the initial crack length to a crack length of ~10 mm. The increase is due to a crack growing through an area where the tensile tangential stresses remain relatively constant. Then a steady decline of K is seen in each graph out to the final a length of 29.21 mm. This would indicate a changing slower crack growth rate due to both the center of the specimen (having a large crack) becoming more compliant while the tangential stresses applied which create a model I crack opening are lessened. These crack driving stresses are lessened because at greater radii from the center, the max temperature at heat-up is less than at the center, therefore the range in temperature to cool-down is less, creating less stress at cool-down.

In looking specifically at the five distinct curves for K, a range can be seen between the highest curve (K at the top node when an m value of 1.2 being used as a plane stress constraint value) and the lowest curve (K at the ¾ node thru the thickness with an m of 1.15 being used). While there is a higher value of m expected with higher constraint when comparing the top surface vs. the ¾ node position, there is a trade off with CTOD as one is closer to the center of the thickness. Since the specimen is technically bending through the thickness, the CTOD is highest at cool down at the very top. So the J (and therefore K) goes up at the top because of CTOD but is balanced by a lower m value. While the ¾ node has a higher m, it has a lower CTOD. The average K across the crack front as estimated by DCCI is seen within the two extremes of K from J, but is slightly closer to the lower limit. However, for a better estimation of the crack growth rates from these K values, published FCG data for B-1900+Hf data was used.

The validity of K being used, again, is based on being at room temperature and the lack of gross plasticity within the model, both before the crack was “inserted” and during cracking and crack growth. Figures 6.16-6.18 show top down views of the maximum principle plastic strain in at three different crack lengths. The figures correspond to crack lengths of 8.89, 14.6, and 18.4 mm, respectively. Previously, the y-direction of plastic strain has been shown, however, in order to show the plasticity caused by the precracked cycles as well

as the crack plastic zone, the a principal plastic strain plot is shown. Plotting this strain allows for the axisymmetry to be seen. The axisymmetric "ring-shaped" plastic strain area towards the center of each figure represents the plasticity resulting from the pre-cracked cyclic behavior of the model. The remaining areas of plasticity (non-axisymmetric) result from the actual crack induced stresses. The area average radius of plastic zone size is on the order of 1 mm, which is well within limits of normal LEFM allowed plasticity. What can be seen, however, is a growing plastic zone size as evidenced by a larger plasticity region seen in the wake of the crack, particularly in Figure 6.18.

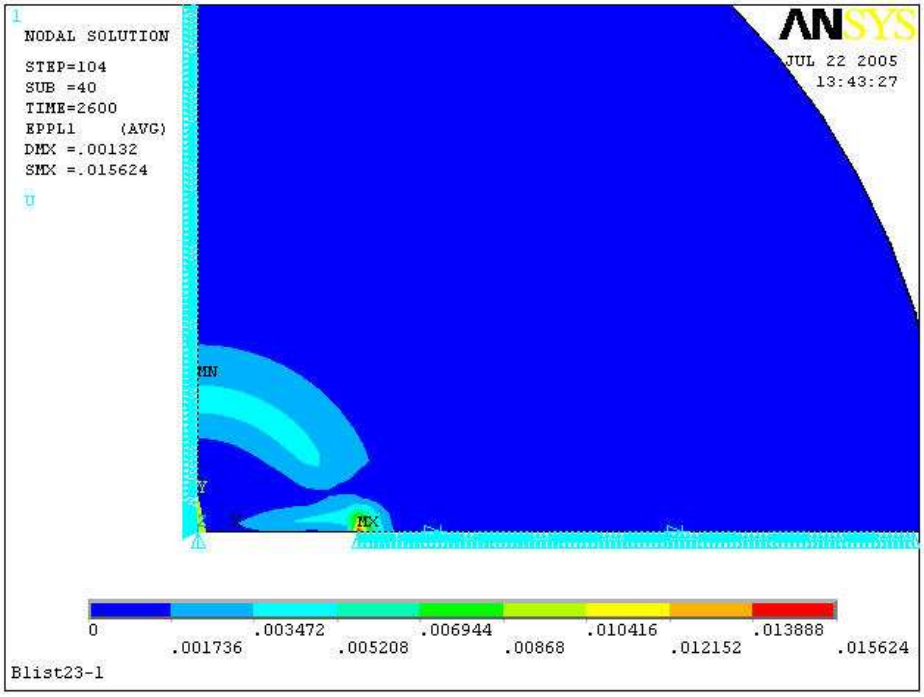

Figure 6.16 Extent of the 1st principal plastic strain when the crack length is 8.89 mm.

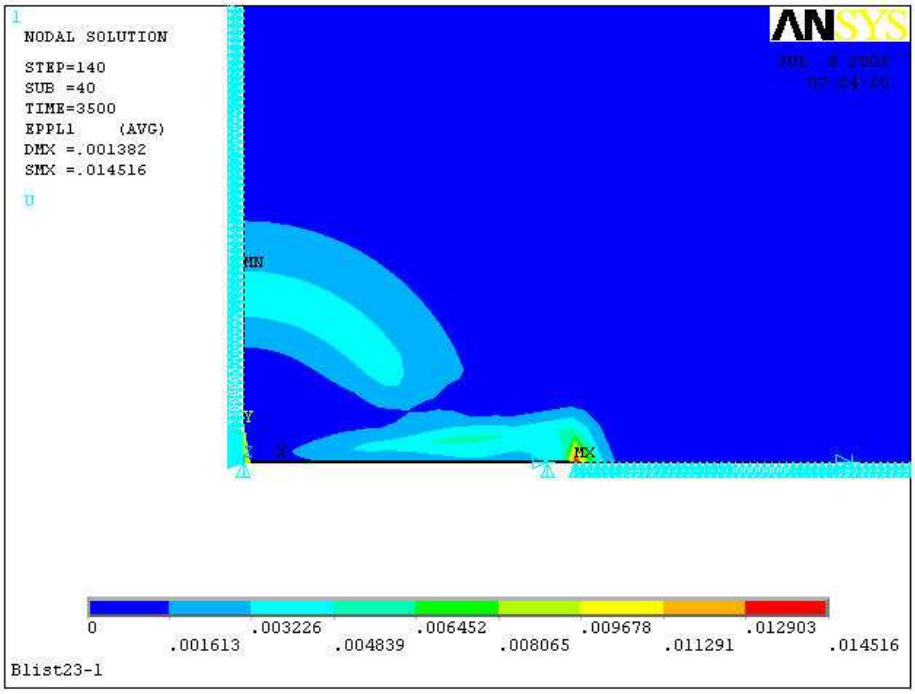

Figure 6.17 Extent of the 1st principal plastic strain at a crack length of 14.6 mm.

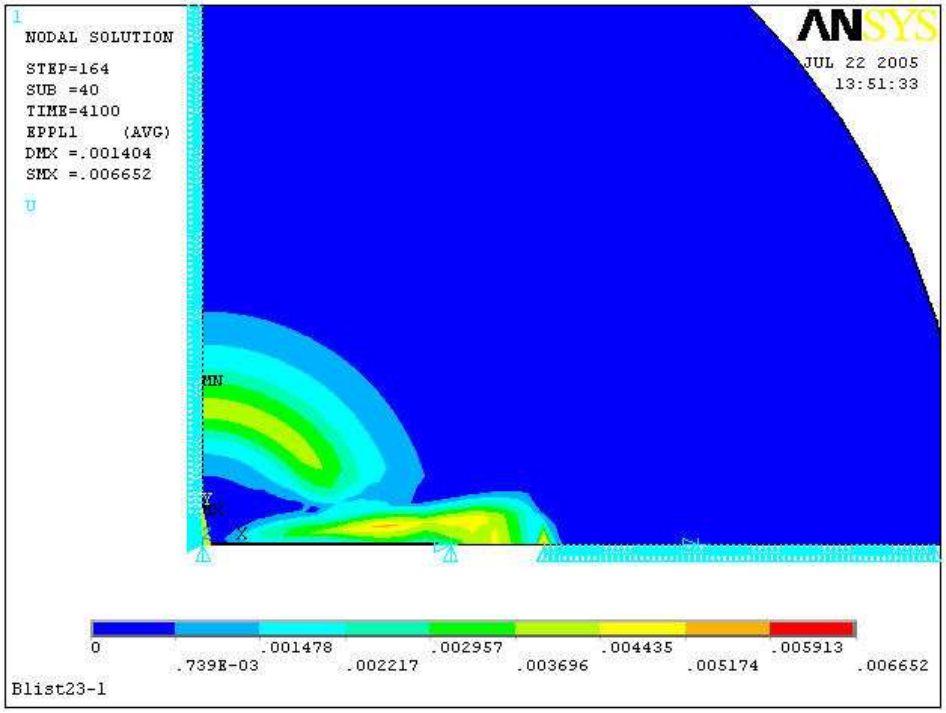

Figure 6.18 Extent of the 1st principal plastic strain when the crack length is 18.4 mm. The growing plasticity region is seen in the wake of the crack tip.

6.4.3 Estimation of da/dN vs. K for Model

Marchand and Pelloux [115] published FCG results of B-1900+Hf for two distinct strain ranges at two different temperatures. With isothermal conditions of both 400 and 925 °C, they plotted the FCG of single-edge notch specimens for the material using da/dN vs. K_{eff}. The graph of this data is shown in Figure 6.19.

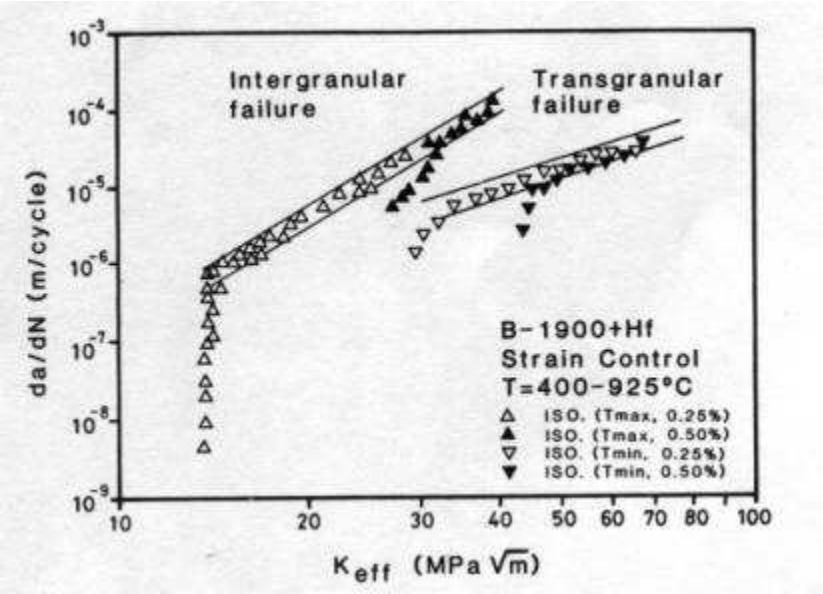

Figure 6.19 Marchand and Pelloux [115] isothermal FCG data at 400 °C (T_{min}) and 925 °C (T_{max}) using single-edge notch specimens of B-1900+Hf.

The data is separated into crack growth that occurred in an intergranular way, which all occurred at 925 °C and the crack growth that was transgranular, which was the 400 °C data. Each test was also run at two distinct mechanical strain ranges for the gross section of the specimen. At 0.25% mechanical strain (shown with the open symbols of each curve) the far-field stress/strain behavior was elastic. At 0.50% mechanical strain (shown as filled symbols), the gross section experiences significant plasticity. The K_{eff} for this test was determined using Equation 6.2.

[6.2] $$\Delta K_{eff} = \frac{\Delta P}{BW} \times \sqrt{\pi a} \times H$$

The equation is a function of ΔP, the change in load for a given cycle, however the minimum load is the opening load (or load at which the crack face begins to reopen after closure), which is determined by the potential drop technique.

The graph shows consistent, Paris-like trends for each type of failure. Based on the two curves, the behavior blister crack on the top surface when the model cools to room temperature is best represented by the 400 °C curve, with the open symbols. The fracture behavior of B-1900+Hf is not expected to change significantly between room temperature and 400 °C and the blister, as has been stated, does not see gross plasticity.

Using this curve, an estimation can be made of the FCG rate of this material based on the curves shown in Figure 6.15. Using the highest curve (K from J at the top with an m=1.2) and the lowest curve (K from J at the ¾ node with an m=1.15), each value of K was used to determine the representative da/dN rate per K as given in Figure 6.19. With a da/dN value determined from each K value, the number of cycles needed to extend the crack at the given K value 0.635 mm was determined for each of the two curves. Equations 6.3 and 6.4 show the method of determining the total number of cycles to “grow” a crack from a given K distribution. The number of cycles, then to grow the crack from 5 to 14.6, 17.78, and 20.32 mm was totaled for both curves by the model and compared to the experimental blister test total. Figure 6.20 shows the highest and the lowest K curves, as stated, only beginning with the crack length of 5.08 mm, corresponding closest to the initially detected crack length from the experiment.

[6.3] $$K_i(ANSYS) \rightarrow {da/dN_i(Marchand)} \Big/ {.635mm} = N_i$$

[6.4] $$\sum_{i=}^{Crack\#} N_i = N_{total}$$

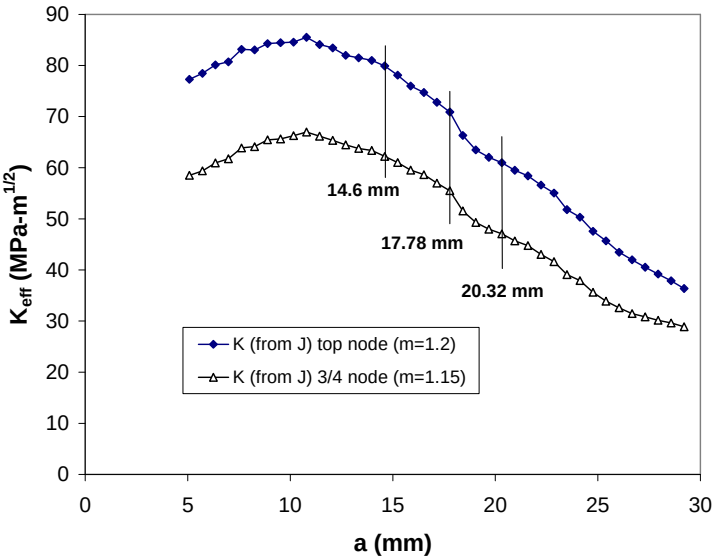

Figure 6.20 Curves of the two extremes of the K vs. a trends from Fig. 6.11, beginning at a crack length of 5.08 mm. Annotations are made to the graph a crack lengths of 14.6, 17.78, and 20.32 mm, where the total number of cycles to grow to the lengths are estimated.

Table 6.3 summarizes the estimated number of cycles to grow to the stated crack lengths for each curve based on Equations 6.3 and 6.4. Recall, that the experimental results showed one crack length (A) reached a final value of 14.43, with the other major branch (B) reaching 20.32 mm over 195 cycles when starting from ~5 mm. If we assume that the average experimental crack length is 17.4 mm (albeit from only two cracks), we can see that by using the K (high) modeled K curve, the stated method for estimating crack growth predicts the number of cycles as being within 5 cycles to grow the crack within 0.5 mm of the final crack length.

Table 6.3 Estimated number of cycles to grow to stated crack lengths for the extreme K vs. a curves as based on Fig 6.13

a length (mm)	14.6	17.78	20.32
	Total Number of Cycles		
K (high)	125	190	265
K (low)	205	303	456

These results indicate that the high estimate of the K vs. a behavior (being calculated from J at the top surface node, assuming a constraint value, m, of 1.2) is a very reasonable estimate for the K vs. a distribution across the blister specimen. Given that the Marchand et al. [115] data is representative of this specimen in order to approximate da/dN, the values for both K and the final number of cycles are very acceptable.

6.4.4 Arrest Distance Estimation

With this “best curve” determined for the cracked blister model, a discussion on a potential crack arrest distance is appropriate. From the experimental test, the cracks did not propagate (based on the crude measurement) between cycles 365 and 462. Assuming the cracks are truly arrested at this cycle number, the final crack lengths recorded would be the arrested crack lengths. From Figure 2.3, we know that the normal means of determining a state of crack arrest is by estimating the threshold K value (K_{th}) for a given Paris curve. Figure 6.19 suggests that for B-1900+Hf at 400 °C, the K_{th} is somewhere between ~30-40 MPa-$(m)^{1/2}$. Upon analysis of the K (high) curve from Figure 6.20, the K levels at 14.6, 17.78, and 20.32 mm are 79.9, 72.8, and 60.9 MPa-$(m)^{1/2}$, respectively. This indicates that the model has not produced an accurate representation of K_{th}.

However, the current model results are based on the assumption that the crack extends 0.635 mm per cycle, when experimentally it averages closer to 0.17 mm per cycle. With a slower actual crack growth, a change in K is

expected. In order to capture the trends for how the K values change at slower crack growth rates, a study was conducted whereby the crack was not extended at all at certain crack lengths, while additional thermal cycles tests were run. At four distinct crack lengths (5.7, 10.8, 17.78, and 29.21 mm) five additional thermal cycles were modeled with no change in crack length. (Note: 5.7 mm corresponds to the 2nd crack length, 10.8 mm is at the peak of each K curve, and 29.1 is the last K value shown in Fig. 6.20. K was determined again as based on the K (high) curve and the K was recorded each thermal cycle. Table 6.4 lists the results of the change in K at each of the crack lengths over the five thermal cycles. K_o is the initial K at the crack length before repeated cycling. K_{+5} is the K after 5 additional thermal cycles with the same crack length.

Table 6.4 Change in K with 5 additional thermal cycles per crack length

Crack Length (mm)	5.7	10.8	17.78	29.21
K_o (MPa-m$^{1/2}$)	78.1	85.5	70.9	36.4
K_{+5} (MPa-m$^{1/2}$)	75.8	82.6	69.7	32.8
Change	-2.3	-2.9	-1.2	-3.6

The change is always down, at an average of 2.5 MPa-m$^{1/2}$. Therefore, if a crack is indeed stationary and not moving, the K does drop with repeated cycles. This is a result of the slight tensile hardening of the material in the area around the crack tip upon each cool down. However, we know that cracks realistically change length and K with each cycle and are not stationary, even with only one additional cycle. So observations can be made regarding two regions of Figure 6.20: the “uphill” side from a = 5 – 10 mm when the curves hit their K peak, and the “downhill” side, being from 10 - 29 mm.

On the uphill side, we expect that while the repeated cycles may drive a K lower, the actual ever growing crack only drives the K higher in this range as evidenced by the rising K_{eff} levels with increasing a. So while one cause results in lower K’s, the other would shift the curve higher. Therefore, realistically, very

little change would be expected in the actual K vs. a relationship on the uphill side of Figure 6.20.

The expectation is different for the downhill side of the curve. Once K reaches its peak at a = 10.8 mm, there is no reason for the K to increase in value as it extends through the specimen because the tangential stress that drives the crack open is lessening. Therefore, the repeated cycles (slower crack growth) would only drop the K vs. a. Moreover, one would expect there to be a cumulative effect, whereby the entire curve wouldn't just shift down by 2.5 MPa-$m^{1/2}$, but a value at 10 mm may shift down 2.5, and the next value at 10.635 mm would shift 5.0, and so forth. This cumulative effect would likely shift the K curve as shown in Figure 6.21.

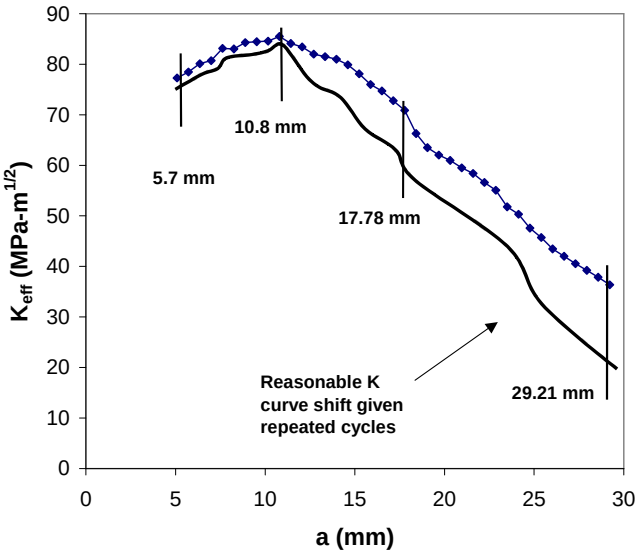

Figure 6.21 Potential shift of the K (high) vs. a curve based on the drop seen in K with repeated cycles as summarized in Table 6.4

The figure shows a minimal shift down for the increasing side of the graph and the cumulative effect dropping the K at a sharper rate on the decreasing side of the curve. Such a shift would change the potential K_{th} significantly lower at the crack length of 17.78 mm to much more reasonable numbers, and certainly closer to the threshold estimation from Figure 6.19.

6.4.5 Fracture Surface Inspection

After the experimental specimen was inspected for final crack length measurements, it was broken in two pieces along the major crack axis (A-B) for fracture surface inspection. To do so, sections of the specimen ahead of each crack tip were cut-off using a wet saw. The specimen was then frozen with liquid nitrogen to keep the material below the ductile-to-brittle transition temperature and placed in a three-point bend load frame. The separated crack faces were each inspected for signs of crack initiation, crack growth increments via striations, or other noteworthy fracture surface details. However, with the amount of oxide present on the crack faces, as well as the surface roughness and crack path irregularities, no indications of striations or crack initiation could be determined.

The crack front at the final crack length of each of the two major branches could be clearly seen. Figures 6.22 and 6.23 show the fracture surface at the ends of both crack A and B, respectively, after 462 cycles using the Leica microscope. The images show the crack front on each side is not a straight, thru-crack shape, but each shows a “tunneling” trend. This trend shows the crack front at the two surfaces lagging behind the front which is more towards the center. The tunneling indicates the state of stress and constraint is indeed a factor in the fracture characteristics of the specimen. With the surface being in more plane stress with less constraint, the stresses are less than towards the inner section.

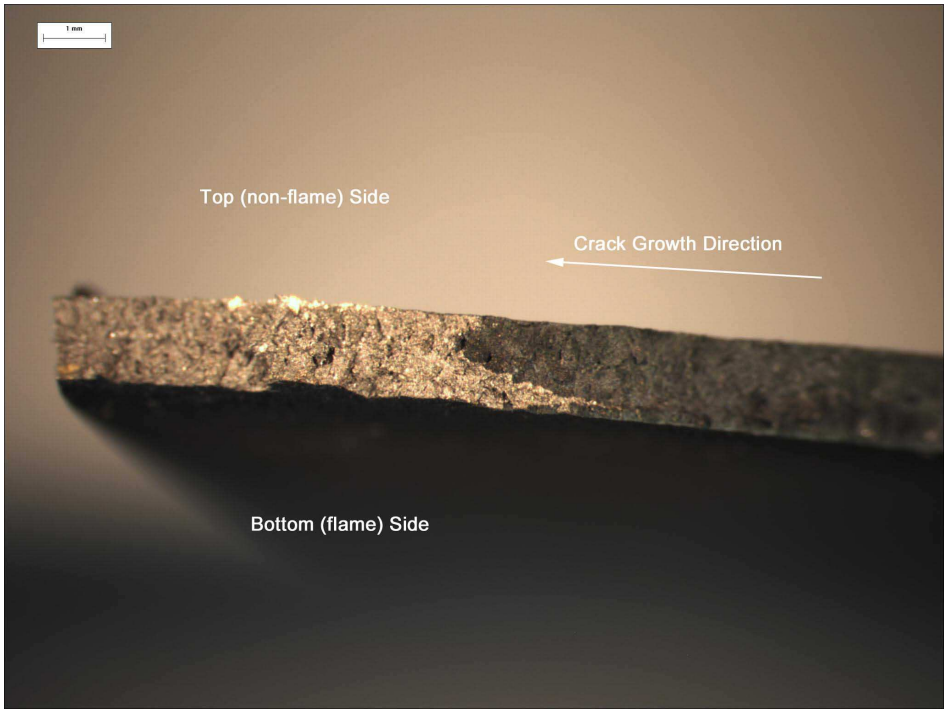

Figure 6.22 Fracture surface of crack branch A, showing the crack front separating the shiny, uncracked material on the left from the darker, oxidized crack face on the right.

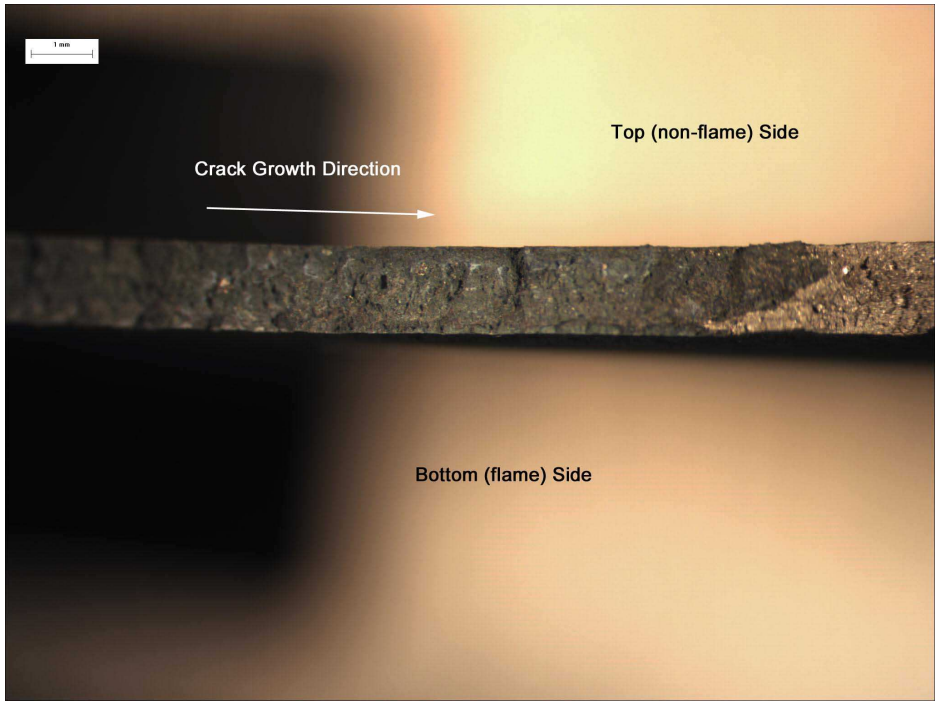

Figure 6.23 Fracture surface of crack branch B, showing the crack front separating the shiny, uncracked material on the right from the darker, oxidized crack face on the left

However, what is also clear is that this front is not symmetric through the thickness at all. The crack extends to a greater distance on the top surface than at the bottom surface and the point of the front at the “tunnel” is not at the center of the thickness. This was caused by the combined loading behavior as discussed in Chapters 4 and 5. The model represents this behavior well as shown in Figure 6.24. Here, with a crack at 5.7 mm being shown, the tensile stress distribution at the top covers more of the thru-thickness dimension then the compression at the bottom. Furthermore, the distribution shows that the max point of stress occurs in the middle of this tensile side (denoted by the “MX”) which is at the node ¾ thru the thickness from the bottom.

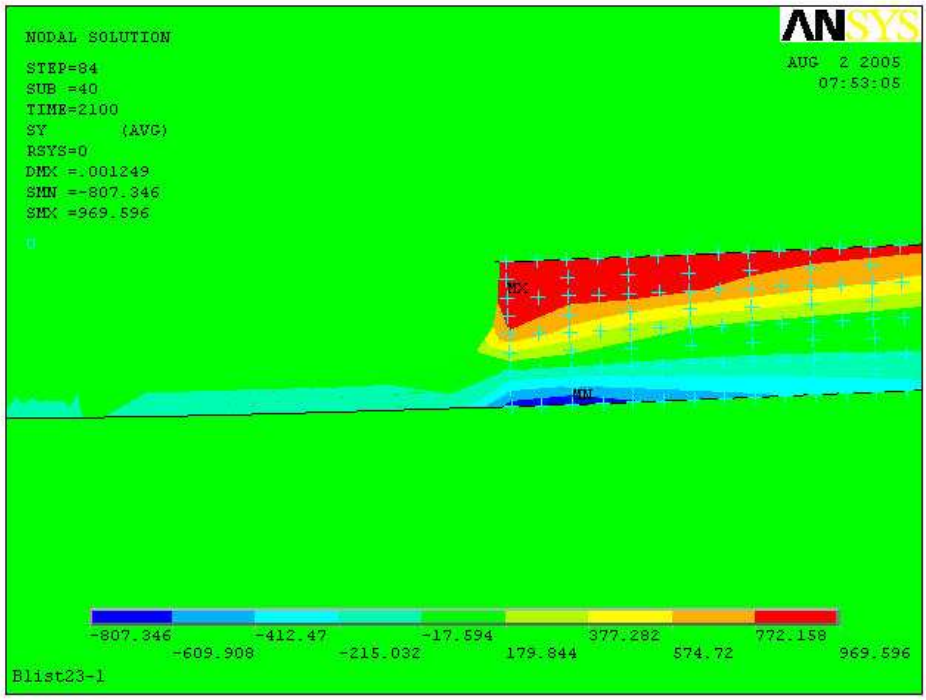

Figure 6.24 The y-stresses distributed through the thickness of the area ahead of a crack at length 5.7 mm at cool-down, showing typical tensile stresses along the top surface, with the max stress noted by the “MX” at the node ¾ thru the thickness from the bottom.

This point of max stress at the ¾ node position corresponding well with the crack front tunnel tip shown in fracture surface inspection raises another question regarding the K vs. a estimation made in Figures 6.17 and 6.20. The highest K curve was deemed most accurate from the perspective of the number of cycles for a crack to grow from 5 - 17 mm. However, this was the “top node” not the ¾ node. It is more likely that the ¾ node position is more determinative for driving the crack growth. While the highest curve might still be accurate, it may be not because the top node with an m of 1.2 is a correct model, but because the ¾ node with an even higher m value than 1.4 is likely. An m value of ~2 on the ¾ node produces a K vs. a curve that matches the m=1.2, top node curve of 6.20. This would indicate match both the crack growth/arrest test data as well as explain the crack front tunneling behavior.

However, more experimental data is needed before any of these curves can be validated and deemed determinative with any statistical significance. While matching the number of cycles to grow a crack between two distances is a good gauge of the viability of the model, repeatability in the test results is necessary before quantitative confidence in the model’s crack growth and arrest is made.

6.5 Conclusions

There were many steps involved in developing an FEA model that could approximate a growing and arresting crack in the hot spot specimen. By these steps, the model yields a very reasonable estimate of FCG through the hot spot as well as potential arrest distance based on the stress intensities developed at each crack length. The following is a set of conclusions that can be made based on the model results.

- A crack can be “inserted” into an FEA model along a plane of symmetry by removing displacement boundary conditions along that plane. An increased number of substeps is necessary for the load step at which the constraints are removed to ensure solution convergence.

- For the thru-crack in the model, it was necessary to have in place a contact element plane along the would-be crack face in order for the symmetry plane to not be unrealistically penetrated by elements/nodes that are in compression before and during cycling at the crack face. The contact plane adequately prevents penetration of the boundary, while allowing for realistic closure effects at the face when compression does occur.

- The crack can be extended along the symmetry plane by the gradual removal of additional boundary conditions.

- The crack is opened most, and thereby driven chiefly, by the tensile stresses that occur along the top surface at cool-down. Because of this, the stress intensity solutions that drive the crack's extension can be calculated along the half of the crack front that is at the top surface at cool-down. This assumption is confirmed by two separate facts observed in the post-blister test specimen inspection:

1) the thru-crack is opened at the top surface while being almost completely closed at the bottom surface.

2) when the crack faces were separated, the crack front on each end of the crack length showed further crack growth along the top surface than the bottom surface.

- Creating stress intensity solutions from both a CTOD to J to K method as well as by R. Singh's DCCI method yielded very similar trends that indicate a growing crack up to a radius of 10 mm with a slowing to arresting crack from 10-20 mm and beyond.

- Using a range of K vs. a curves for the model, the FCG could be approximated by utilizing published da/dN vs. K_{eff} data and totaling the number of cycles needed to grow a crack to varying distances from an initial length of 5 mm. Using the highest of these curves, the number of cycles estimated by the model and the published data that are needed to grow a crack from 5 to 17 mm is within 5 cycles of the experimental test, if the two main final crack lengths are averaged. Using this process, the likely arrest distance is estimated to be near 17 mm as well, based on the modeled hot spot conditions.

- The tunneling behavior visible in the post-test inspection images that indicates the stress state plays an important role in crack behavior. Furthermore, the location of max stress along the crack front as represented by the straight thru-crack model corresponds favorably to the location of the “point” of the tunnel through the thickness.

- Additional test data is necessary before statistical significance and confidence can be placed in the model. While the model qualitatively represents the rapid crack growth and eventual arresting behavior of the one blister test, variability may exist in such test data that has not been observed.

CHAPTER 7: SUMMARY AND CONCLUSIONS

The work accomplished in this investigation sufficiently uses FEA code to model the repeated hot spot behavior and subsequent fatigue crack growth of a conventionally-cast nickel-based superalloy as represented by blister specimen testing. This model provides a framework by which the effects of hot spots can be shown to effect the response of both the uncracked and cracked blister experiment. Using this model, parametrically, one can vary different inputs (temperatures/temperature gradients, heat up times, specimen geometry, and material properties) to show the impact on the stresses and strains, the out-of-plane response, as well as crack behavior. With such a study, one can predict the severity of damage based on specific conditions in turbine engines, thus facilitating a damage tolerance approach toward the maintenance of an engine that may experience hot spot behavior.

What follows is a summary of the specific conclusions that can be made from this study involving the constitutive modeling, uncracked, and cracked plate modeling accomplished in this investigation.

7.1 Constitutive Modeling

- The published temperature dependent tensile properties can characterize the reversed loading, compressive, as well as tensile behavior at temperature ranges up to 1093 °C.

- The yield and subsequent plastic hardening behavior of the material is adequately approximated as bilinear kinematic as based on the published curves found from the research by Chan et al. Based on the findings of Marchand and Pelloux [26], the hardening behavior of B-1900+Hf is concluded to be kinematic

only, in spite of many materials normally behaving as a combination of kinematic and isotropic.

- While the published steady-state creep behavior can be easily determined from multiple sources for four different high temperature levels, a conservative shift towards faster secondary creep rates is necessary if the properties are to match stress relaxation behavior.

- It is assumed that no measurable creep or stress relaxation behavior occurs below 760 °C for even high levels of applied stress.

7.2 Uncracked Blister Modeling

- A quarter-plate with symmetry boundary conditions can represent the behavior of a circular blister test specimen sufficiently.

- In comparing the out-of-plane displacement for a model with experiment, having a percent error of 24% at heat up and 14% at cool down at the first cycle and 5% at heat-up and 24% at cool down after twelve cycles (in a model that possesses both geometric and material nonlinearity) the material properties used in the model as denoted in Chapter 3 are acceptable.

- The overall out-of-plane translation distance (between heat-up and cool-down) improves significantly over the twelve cycles. The initial total translation error is at 42% after the first cycle, but drops to 10% after cycle twelve.

- The assumed temperature gradients developed from four thermocouples used in the sequential thermal loading procedure adequately approximate the actual thermodynamic application of heat via the burner-rig test set-up.

- The geometric nonlinearity capability incorporated into the model, allowing large strains and rotations, along with a slight (0.5%) thru-thickness temperature gradient are all that is required to initiate the instability or buckling that occurs in the model.

- The buckled shape creating what is known as the “blister” takes its eventual basic form (concave on the top, convex on the bottom) within the initial heat-up. Yielding occurs at the hot spot center, primarily on the top surface, which creates the permanent specimen blister, even after cool-down.

- The in-plane stress behavior at the center is governed by bending, with tension occurring on the bottom and compression on the top during heat-up, while cool-down reverses this behavior. The yielding that occurs creating the deformed shape occurs at the top surface, with compressive yielding at heat-up and tensile yielding at cool-down.

- Stress relaxation occurs at the center of the specimen when temperatures exceed 760 °C. Since the greatest stress magnitudes upon heat-up occur on the top surface in compression, this is where the greatest relaxation takes place. The highest magnitude of stress is always at the top surface (whether in heat-up or cool-down) because of the combined loading effects of bending and radial compression or tension that result at the center.

- A list of functions or options that must be specified in the ANSYS code for the current analysis (with the actual ANSYS command) are summarized as follows:

- Bilinear kinematic hardening is used to define the yield, tangent modulus, and hardening (BKIN)
- Norton secondary implicit creep is modeled (TB, CREEP, , , ,10)
- Geometric nonlinearity is on (NLGEOM ON)
- Rate dependency is on for the 2nd and 3rd load step for each thermal cycle (RATE, ON)
- For each load step, 40 substeps are used, with a maximum possible number of 60, to ensure convergence. (NUSUBST, 40, 60, 40)

- Though a single-source for error is not known for the difference in out-of-plane displacement, one potentially significant source may lie in the slight saddle-like warping behavior observed in the test article. This warping, perhaps caused

by having the hot spot applied just off of geometric center, is not represented in what is a completely axisymmetric model.

- An additional source for error could lie in the changing thermal gradient with each cycle. The experimental test only recorded thermocouple readings on each odd cycle. Therefore, the temperature gradient created from these recordings was repeated for the following even cycle. While the overall temperature change is not great, it would have a direct impact in the displacement response.

- The model characterizes the out-of-plane profile across the specimen diameter very well. With warping effects normalized, the shape is almost identical, showing the blister “bubble-like” shape at the center over the same radial distances.

- The stress behavior at the hot spot center continues the same trends over twelve cycles that were observed in the initial cycle summarized in Chapter 4. The top, concave surface exhibits the higher magnitudes of stress (during both heat-up and cool-down) than the bottom and remain opposite in sign due to the bending behavior. Because of this higher stress magnitude, the top undergoes the most plasticity and creep/stress relaxation behavior.

- Both the plasticity and creep strains are localized toward the center of the specimen. The plasticity is by no means “gross” throughout the specimen, and again is greater at the top. The residual plastic strain at the top is compressive, even after cool-down. This is because the greatest yielding occurs initially in compression at heat-up, but does lessen after reverse-loading occurs when it yields in tension at cool-down.

- The creep strains (though caused actually by stress relaxation) are more pervasive radially across the specimen than the plastic strains, but are still localized toward the center. These strains, of course, occur only at temperature.

- The repeated yielding, particularly at the top surface, does indicate kinematic hardening over each cycle but lessens to only ~2 MPa between the eleventh and twelfth cycle. With such minimal change, the model is believed to

have “shaken-down” sufficiently to have assumed the appropriate stress/strain state of the actual test article before crack modeling.

7.3 Crack Modeling

- A crack can be “inserted” into an FEA model along a plane of symmetry by removing displacement boundary conditions along that plane. An increased number of substeps are necessary for the load step at which the constraints are removed to ensure solution convergence.

- For the thru-crack in the model, it was necessary to have in place a contact element plane along the would-be crack face in order for the symmetry plane to not be unrealistically penetrated by elements/nodes that are in compression before and during cycling at the crack face. The contact plane adequately prevents penetration of the boundary, while allowing for realistic closure effects at the face when compression does occur.

- The crack can be extended along the symmetry plane by the gradual removal of additional boundary conditions.

- The crack is opened most, and thereby driven chiefly, by the tensile stresses that occur along the top surface at cool-down. Because of this, the stress intensity solutions that drive the crack’s extension can be calculated along the half of the crack front that is at the top surface at cool-down. This assumption is confirmed by two separate facts observed in the post-blister test specimen inspection:

1) the thru-crack is opened at the top surface while being almost completely closed at the bottom surface.

2) when the crack faces were separated, the crack front on each end of the crack length showed further crack growth along the top surface than the bottom surface.

- Creating stress intensity solutions from both a CTOD to J to K method as well as by R. Singh’s DCCI method yielded very similar trends that indicate a

growing crack up to a radius of 10 mm with an slowing to arresting crack from 10-20 mm and beyond.

- Using a range of K vs. a curves for the model, the FCG could be approximated by utilizing published da/dN vs. K_{eff} data and totaling the number of cycles needed to grow a crack to varying distances from an initial length of 5 mm. Using the highest of these curves, the number of cycles estimated by the model and the published data that are needed to grow a crack from 5 to 17 mm is within 5 cycles of the experimental test, if the two main final crack lengths are averaged. Using this process, the likely arrest distance is estimated to be near 17 mm as well, based on the modeled hot spot conditions.

- The tunneling behavior visible in the post-test inspection images indicates the stress state plays an important role in crack behavior. Furthermore, the location of max stress along the crack front as represented by the straight thru-crack model corresponds favorably to the location of the “point” of the tunnel through the thickness.

CHAPTER 8: RECOMENDATIONS

The first and perhaps most obvious recommendation is that additional experimental results are a must for the model to be deemed valid within a statistically significant confidence interval. Only one experimental blister test was run, producing only three crack branches, with just two being used for crack modeling validation. Any good research engineer would insist upon more statistical evidence for further validation.

However, while there does need to be more testing, extreme variation from the one observed test behavior is not expected. Specifically, the amount of out-of-plane displacement is primarily a function of two major model inputs: 1) the material properties and 2) the input temperatures. If the test specimens are tested and controlled in a similar fashion, little variation is expected. The greater variation is expected in the experimental cracking results, particularly in the initial crack pattern. With the scatter that is well documented for crack initiation characterization, the actual crack pattern (specifically branching behavior) is believed not consistent if subsequent tests are conducted. The author is confident that each crack branch will arrest within a statistical range based on the specimen loading and geometry.

Additionally, a study was not accomplished whereby inputs such as the hot spot size, ΔT, and model thickness were varied. Parametric studies of these three variables could be conducted and would be valuable in the understanding of different hot spot geometries.

The next recommendation is related to the first as more detailed material properties testing is warranted. Assumptions about the material properties, particularly the nonlinear behavior (plasticity/hardening, creep/stress-relaxation, etc.) were made based on a compilation of data from many publications. While these assumptions were believed valid, the opportunity to characterize the

material's behavior for the precise conditions modeled would only increase the accuracy of the study.

The experimental results showed an irregular crack front at each end of the major thru-crack. A specific crack modeling recommendation would be to vary the FEA front to more closely represent the actual front. A tunneled front as pictured in Figures 6.18 and 6.19 would be possible, even with the current element size and shape. The K vs. a and subsequent da/dN estimation would be expected to change. If done, the stress intensity resulting from the "forward-most" tunneling point would be the likely node to produce the graph from.

A significant amount of oxide developed on the center of the flame-side of the specimen as well as along the crack faces. The effects of oxidation, particularly related to TMF and FCG, continue to be a major area of investigation and should be pursued in better characterizing the crack growth behavior of this study. While incorporating its effects into an FEA model would be difficult, a thin layer of elements along the flame side section is a possible means of accounting for the oxidation effects.

Three additional areas for research that make worthy areas of follow-on investigation have been given some initial study and are noted in the first three appendices. While this initial study shows much detail in each of the areas, they were considered "cursory" analysis and thus are not included in the main body of the dissertation. The analysis of each is meant to be somewhat introductory in nature for others to begin more detailed follow-on work.

A more detailed investigation into the crack branching phenomena is another possible area for study. While the first appendix chapter in this dissertation (Appendix A) gives a cursory analysis for noting the stress states that can lead to/explain crack branching, further crack branch modeling could add much to understanding this behavior. Utilization of the T-stress (a parameter describing the biaxiality of the stresses at a crack tip) is one recommended means of accomplishing this.

Another area of study is the effect of uniformly dispersed cooling holes throughout the model. Actual in service liners have these holes, showing their

effects on constitutive response, crack initiation, crack growth and crack branching direction. The results of their effect in the first of these areas is summarized in Appendix B.

Finally, the effect a thru-crack in the hot spot has on the actual liner thermal gradient is also an area that significantly effects the constitutive response of the hot spot. This effect, called “cooled-lip” behavior is briefly outlined and studied in Appendix C.

APPENDIX A: CRACK BRANCHING

There were additional areas of research that were briefly investigated, each having to do with specific features of the combustor liner cracking behavior. One of those areas is the potential for crack branching through the hot spot. This appendix section will discuss that potential as seen with the stress levels and directions in the FEA model when cracks are present.

A.1 Experimental Results Showing Branching

One common result of thermal fatigue induced crack behavior in combustor liners is the presence of multiple cracks emanating from one central (2a) crack. In fact, the experimental blister test conducted for the present investigation showed this behavior. Recall, three thru-crack tips were seen from the naked eye as well as under a microscope and were labeled branch A, B, and C. Figure A.1 depicts the top-side (non flame-side) of the overall specimen showing each branch. However, closer inspection revealed there are signs of other “would-be” branches appearing as surface flaws on the top surface.

Closer inspection under higher magnification was conducted in areas around crack branch A and B. Figures A.2 and A.3, respectively show these areas as composite images, showing close-ups of regions in which small surface cracks appear. Figure A.2 shows several surface cracks around crack branch A, all of which are radially oriented with respect to the overall disk. Figure A.3 shows one surface crack that has grown over 4 mm and is actually linked to branch B. Figure A.4 shows the overall crack pattern overlaid with the locations, distances, and directions of the small surface cracks seen under the microscope.

What can be seen from these photos is that each branch is generally in a radial direction. This is because, most likely, the state of stress, throughout the specimen, is axisymmetric. But in order to understand this behavior more completely, the FEA solution reveals more details regarding this stress state.

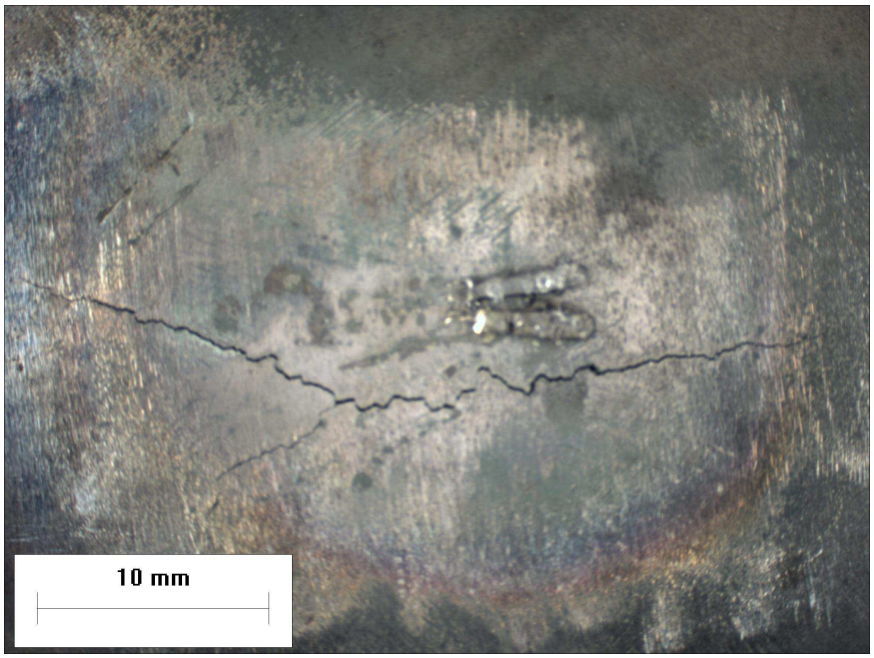

Figure A.1 The top side of the experimental blister specimen with cracks A and B forming the major crack (2a) while crack branch C being the smaller crack branch directed toward the bottom left of the photograph.

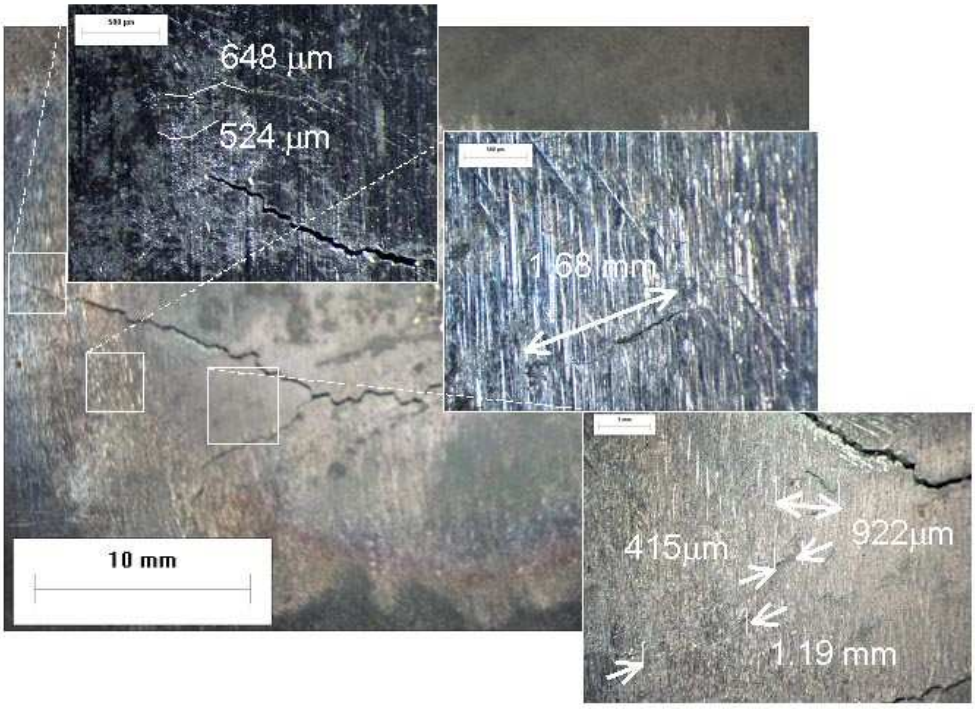

Figure A.2 Composite image showing close-up areas of the region surrounding crack branch A.

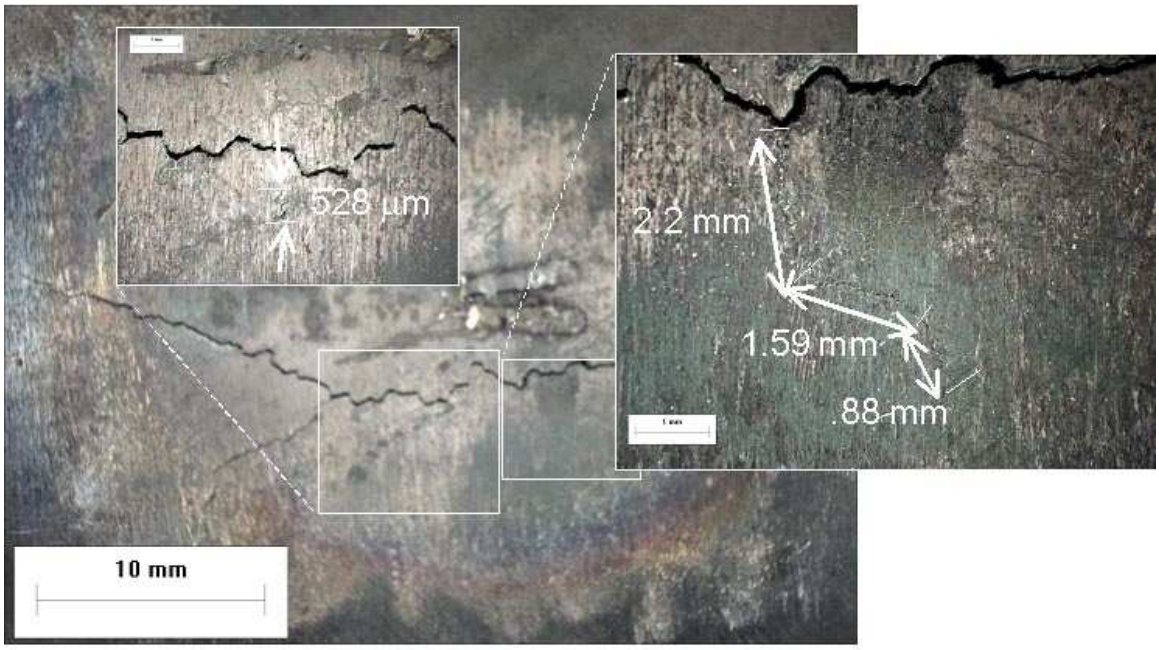

Figure A.3 Composite image showing close-up of the region surrounding crack branch B.

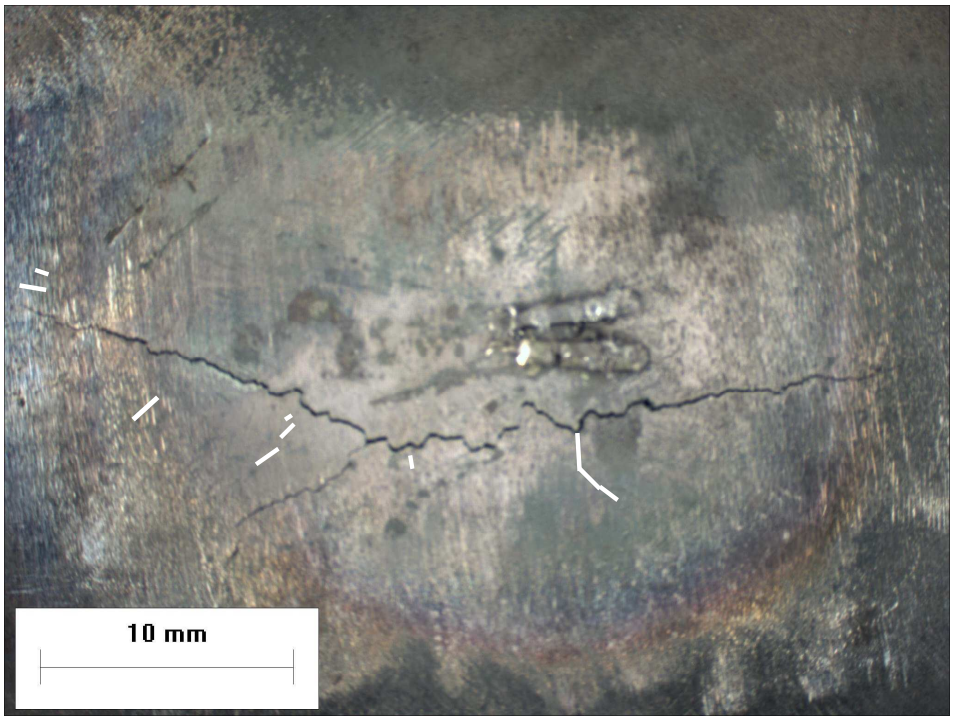

Figure A.4 Overall Crack Pattern

A.2 Possible Cause and Location of Branch

Figures A.5-A.9 reveal the distribution of the in-plane stress state at six locations along the crack path. The ANSYS images plot the 1st principal stress across the deformed model at cool down for the given cycle. Each figure corresponds to a different crack length after cool-down as it is extended from a length of 5.7 mm in Figure A.5 through 17.78 mm in Figure A.9. In each figure, the “shaded” box indicates the location of the crack tip at the top surface. Each of the six points along the path is on the top surface of the specimen, which is the tensile (and therefore crack opening) side of the thickness upon each cool-down. The in-plane stress state for each location is shown with arrows oriented in the two planar orthogonal directions, x and y. However, along this particular crack path (which is on the x-z plane), the x-direction corresponds to the radial direction in the axisymmetric coordinate system, while the y-direction (always normal to the crack face) corresponds to the tangential (or θ) direction. Each stress value has units of MPa. The arrows are proportional in size to the relative stress magnitude and the arrow direction indicates whether the stress is tensile (out of the box) or compressive (into the box).

Figure A.5 shows the stresses when the crack length is modeled at 5.7 mm (shaded box). In observing the node in the wake of the crack at the model center, we can see that the tangential, y-stress which drives the crack open is almost nonexistent; the node is on the crack face. However at that same node, the radial, x-stress is still quite high at 539 MPa. This value is actually slightly higher then at the crack tip, which is at 516 MPa. This radial stress is relatively high along this crack path up through the node at a radius of 13.32 mm, which is at 538 MPa.

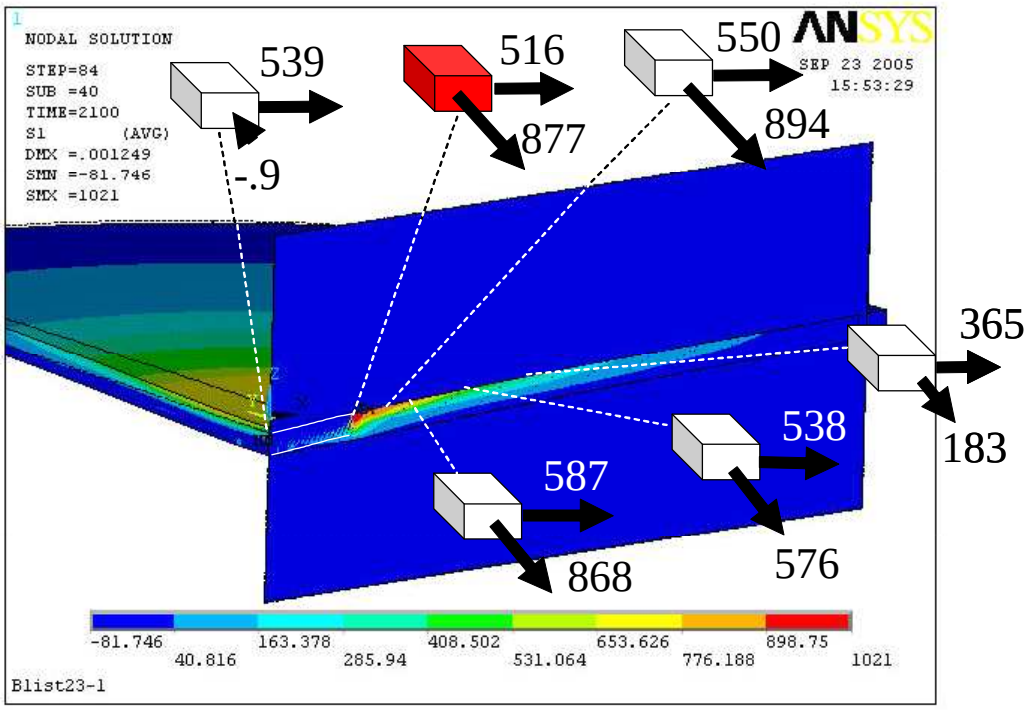

Figure A.5 Model stresses along the top surface along the crack path when crack length is 5.7 mm.

The ultimate cause of this behavior lies in the overall compliance change in the specimen. As a crack extends, the material on either side of the crack faces becomes much more compliant as the crack is permitted to open. This opening, or compliance is not present in the orthogonal (or cracking) direction. Therefore, the radial stresses remain high along the crack path.

This stress radial direction would be the driving stress towards either a branched or turning crack. If this stress remains high, particularly at, or in the wake of a given crack tip, the possibility for crack initiation in a different direction certainly exists. Experimentally, the crack was not a turned crack, but a bifricated or branched crack. Recall, the branched crack was seen immediately, when the first cracks were seen and measured. The distances were between 5-6 mm each. Though this was just one specimen, the indication is that the cracks branch when the initial crack is at an early (at short crack length) stage rather than late (at long crack lengths). This early stage is seen in Figure A.5. Figure

A.6 shows crack at a radial distance of 7.62 mm. The tangential stress at the node at 5.7 mm have dropped off as expected, while the radial stress is 399 MPa.

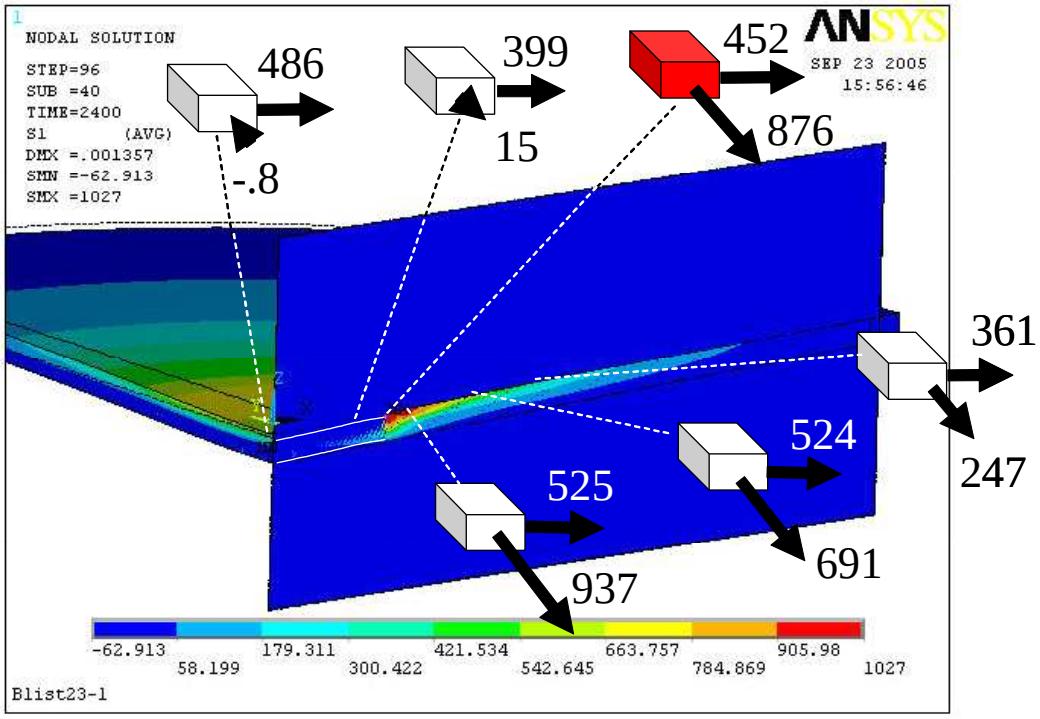

Figure A.6 Model stresses along the top surface along the crack path when crack length is 7.62 mm, showing high radial stresses and low tangential stresses in the wake of the crack.

Also note that the stresses ahead of the crack tip in each direction are both high. In fact the stresses at the next node shown ahead of the crack tip (r = 8.89 mm) are even higher than at the crack tip itself. It should be pointed out that the highest tangential, or y, tensile stress for this and every crack increment shown is not at the very top surface, but is at the ¾ node position on the crack front. For this particular crack length, that node has a tangential stress of 968 MPa. This trend is a result of the plain strain constraint within the thickness.

The next figure, Figure A.7, shows the crack length now at 8.89 mm. The same trends continue. The stress or load is shed in the tangential direction

along the crack face while remaining somewhat high radially. However, it should be pointed out that while the radial stresses in the crack wake are higher relative to the tangential stresses, they are decreasing in comparison to previous crack lengths. Each successive crack extension lessens the radial crack stress levels behind the crack. This adds more explanation as to why a crack might branch when the original crack is shorter, rather than longer.

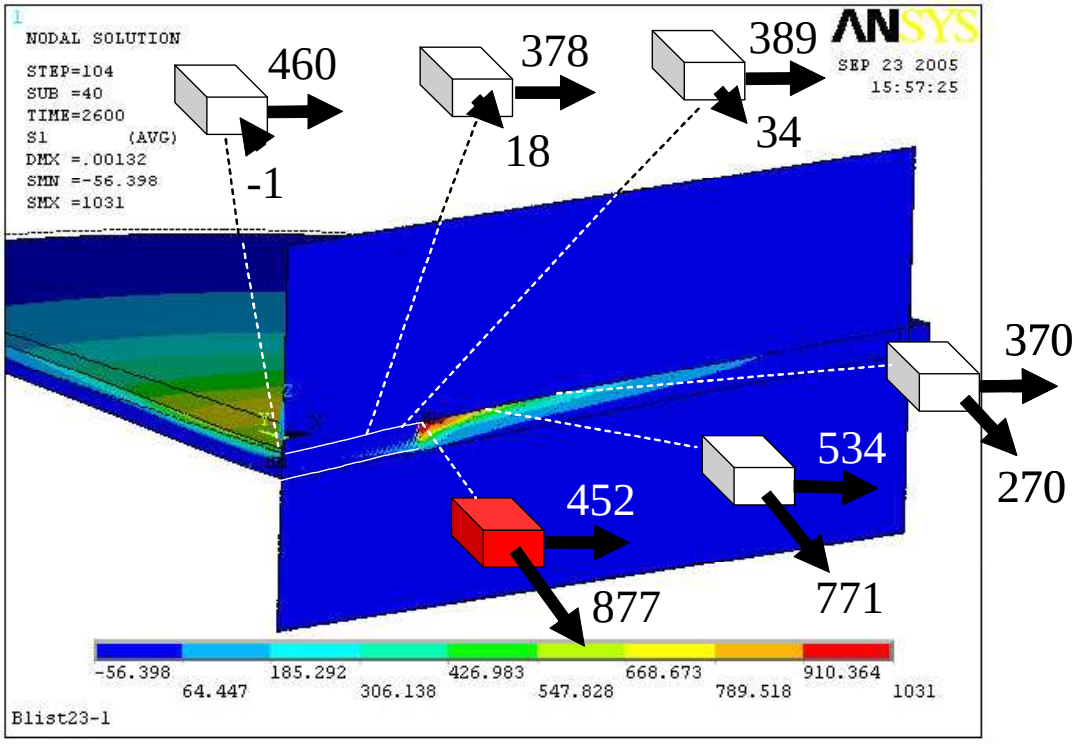

Figure A.7 Model stresses along the top surface along the crack path when crack length is 8.89 mm, showing high radial stresses and low tangential stresses in the wake of the crack.

In Figures A.8 and A.9 complete the crack extension images for cracks of length 13.3 and 17.78 mm, respectively. The trends previously noted only continue.

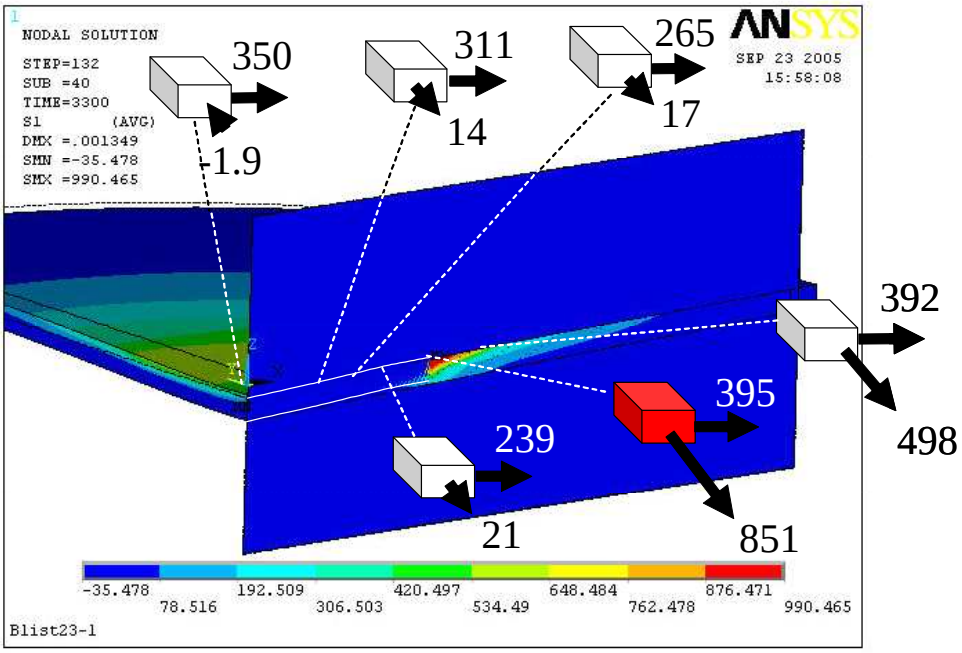

Figure A.8 Model stresses along the top surface along the crack path when crack length is 13.32 mm.

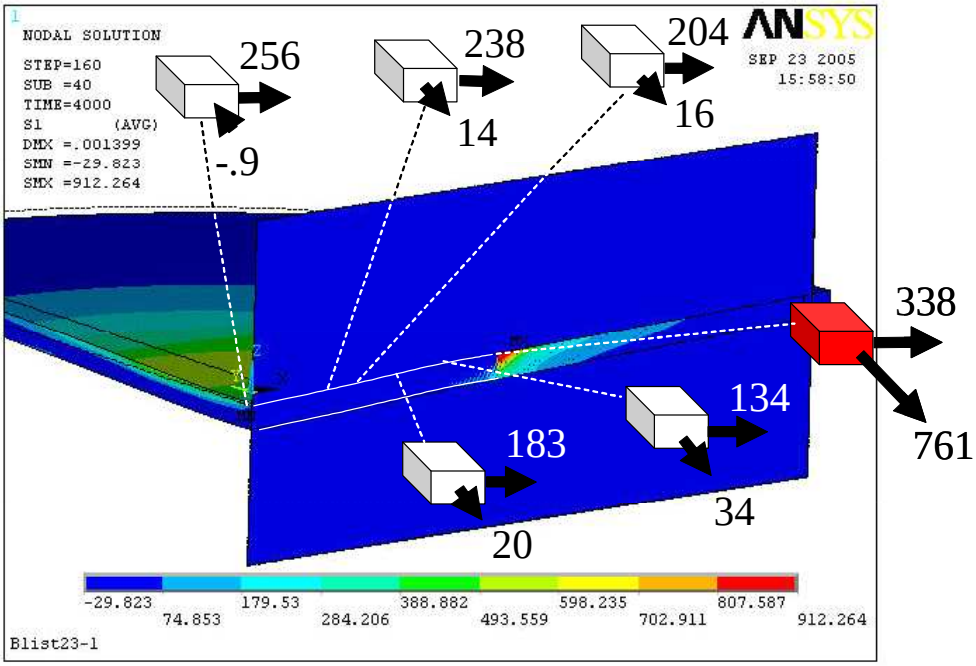

Figure A.9 Model stresses along the top surface along the crack path when crack length is 17.78 mm. This is average crack length of the two major cracks when they experimentally arrested.

A.3 Crack Branching Direction

This in-plane stress overview offers the mechanical potential for a branched crack along a crack path as well as an explanation for why the crack may branch at a specific location. The reason for the specific branch direction may also be shown from the FEA results.

The 1st principal stress distribution across the top surface when the crack is 5.7 mm long is shown in Figure A.10. This figure shows the axisymmetric nature of the maximum tensile stress field in-plane, showing the highest stresses at the crack tip. However, note the orientation of those stresses above the crack tip. Instead of the half-cartioid shape being completely orthogonal to the crack surface, it “curves” around in the tangential direction. Again, this is due to the axisymmetric nature of the stress state.

With this stress distribution, a crack beginning to branch at or close to the crack tip at the top surface would be expected to grow normal to the direction of the 1st principal stress in that area. This direction, again, would be radial in nature. Figure A.11 further illustrates this point. Shown here is a vector plot of the principal stress field with the direction of the 1st principal stress being shown as the darkest arrows.

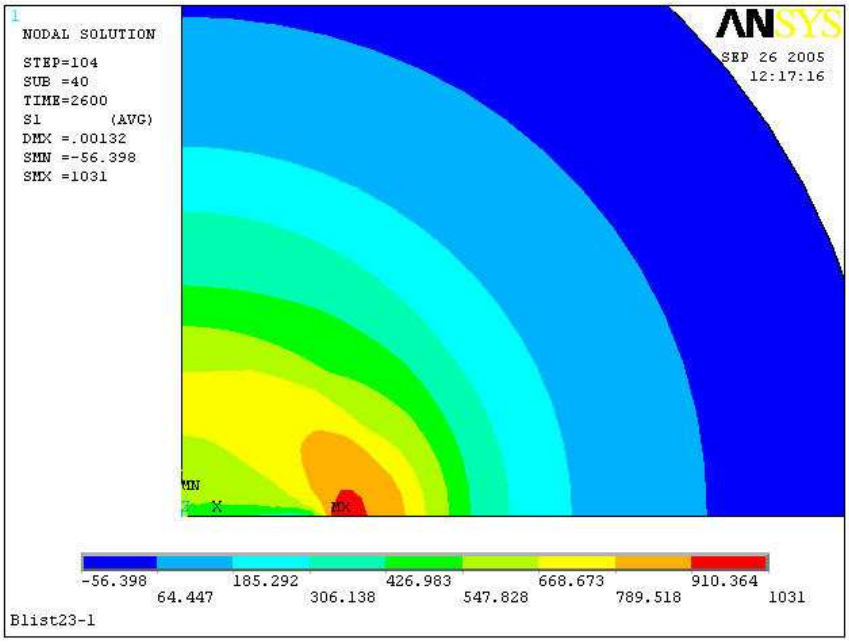

Figure A.10 A plot of the 1st principal stresses when the crack is 5.7 mm. "MX" denotes the crack tip location and the max principal stress at 1031 MPa.

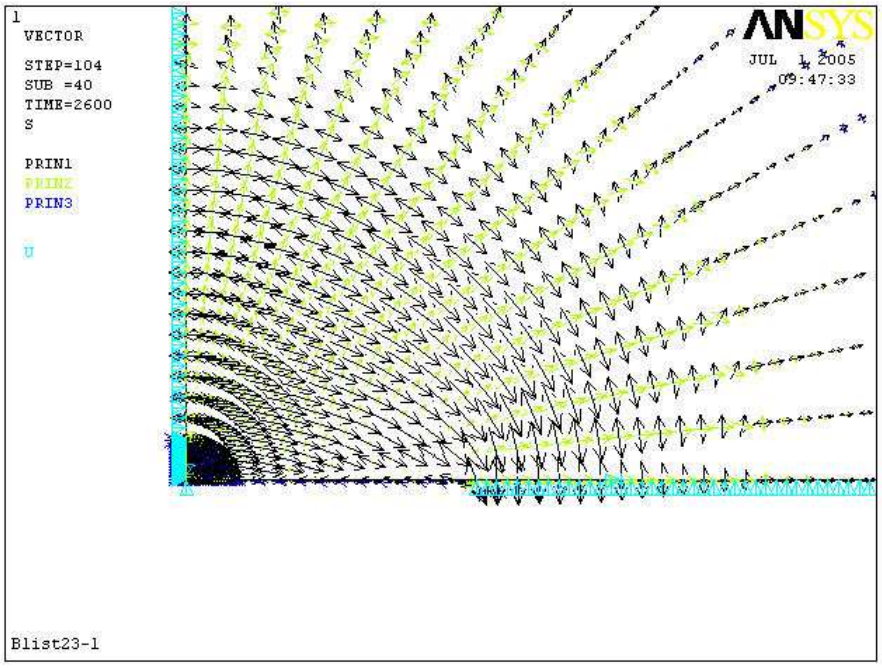

Figure A.11 A vector plot of the principal stress distribution showing the max principal stress with the dark arrows (the length corresponding to relative magnitude.

While these graphs explain the branching behavior of the experimental blister test, an important point should be made in reference to the actual in service liner and its hot spots. As has been pointed out, typical liners are perforated with many cooling holes through the thickness. These cooling holes could not only serve a “waypoints” along the crack path, it is likely that a crack branching scenario would emanate from a hole itself. A biaxial stress state that is commonly found near a branching vertex could easily (depending on the hole location) redistribute stresses around a hole creating the potential for two cracks to initiate. Therefore, as crack branching patterns are studied, the advent of holes in a structure may alter the probable location and direction crack branches would grow.

APPENDIX B: HOLE EFFECTS IN AN UNCRACKED MODEL

As was mentioned at the conclusion of Appendix A, cooling holes could play a significant role in the crack branching behavior of either a blister specimen or an actual combustor liner. These holes would also have an impact on the overall blister behavior during thermal cycling before cracks initiate and grow. This appendix section discusses that changed behavior in a brief analysis.

B.1 Effective Hole Behavior

Cooling holes perforating a blister type specimen would affect the stresses and strains resulting from the hot spot and thermal cycling. Holes, depending on their size and distribution, would serve to increase the compliance of the in-plane constitutive response of the specimen in much the same way a crack increases the compliance in the direction orthogonal to the cracking direction. If the holes were uniform and evenly distributed, they would allow the specimen to expand and contract in a less stiff manner.

To model such behavior, the contributions of two groups of investigators developed a way to approximate the mechanical response of a component perforated with evenly distributed uniform holes by merely altering the basic material properties. Uragami and colleagues [117] and Nakamura et al. [118] developed equations that modified the modulus, tangent modulus, and creep properties based on the geometry of the repeated hole patterns in a plate of material. Their work assumed a unit cell that represented this repeated pattern of circular holes that are oriented in triangular shape. Shown in Figure B.1, this perforated unit cell is defined by two main distances, h, and P. The h dimension is the distance between the edges of two holes, while P is the representative distance between the centers of two holes which are closest together. The authors dub the ratio of these two parameters as the “efficiency ratio” which equals h/P.

With this ratio, the modulus, tangent modulus, and the coefficient in the Norton secondary creep equation are modified. Each of these modified equations is shown in Equations B.1, B.2, and B.3.

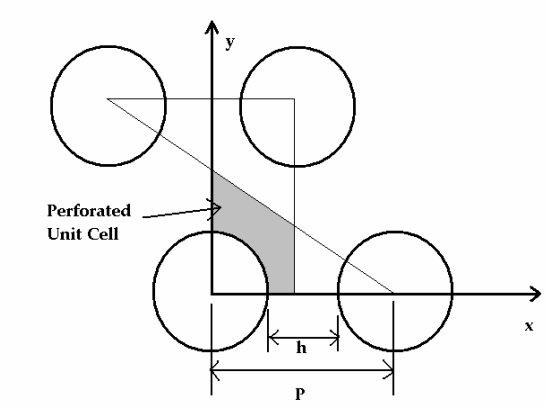

Figure B.1 The perforated unit cell geometry for determining the efficiency factor of mechanical structures.

B.2 Modeling the Effective Hole Behavior

Using these equations, a set of material properties representative of B-1900+Hf were modified, and thermal cycling was modeled for a blister specimen in much the same way as before. The new properties as altered by an efficiency factor of 0.833 and the formuls for the alteration are shown in Table B.1. And with these properties, the results of the change in the stress in the model center, at the top surface are shown in Figure B.2 after ten thermal cycles. Two point-to-point curves are shown, one being the baseline material with no modification and the other approximating “equivalent” holes.

Table B.1 Equivalent Hole Formulas

Property	Effective Hole Formula
Efficiency factor (η)	h/P
Modulus (E)	$E\,\eta$
Yield Strength (Sy)	$Sy\,(1.12\eta - .01)$
Tangent Modulus (α)	$\alpha\,(1.23\eta - .08)$
Norton Creep Coefficient (C_1)	$C_1\,\eta^{-1.1}$

The figure shows the vertical dashed lines, indicating the end of each of the ten thermal cycles. Much like the previous analysis, this is the cool-down stage of each cycle when the stresses are tensile at the top surface of the model. The two curves indicate this same tensile behavior, though the stress magnitudes are less for the model assuming equivalent holes as one would expect. This is most true at particularly high magnitudes of nominal stress. At the each trough of the curves (when the specimen is at heat up) the stresses are less in magnitude and thereby, the difference between the non-holed curve and the equivalent holed curve is minimized here.

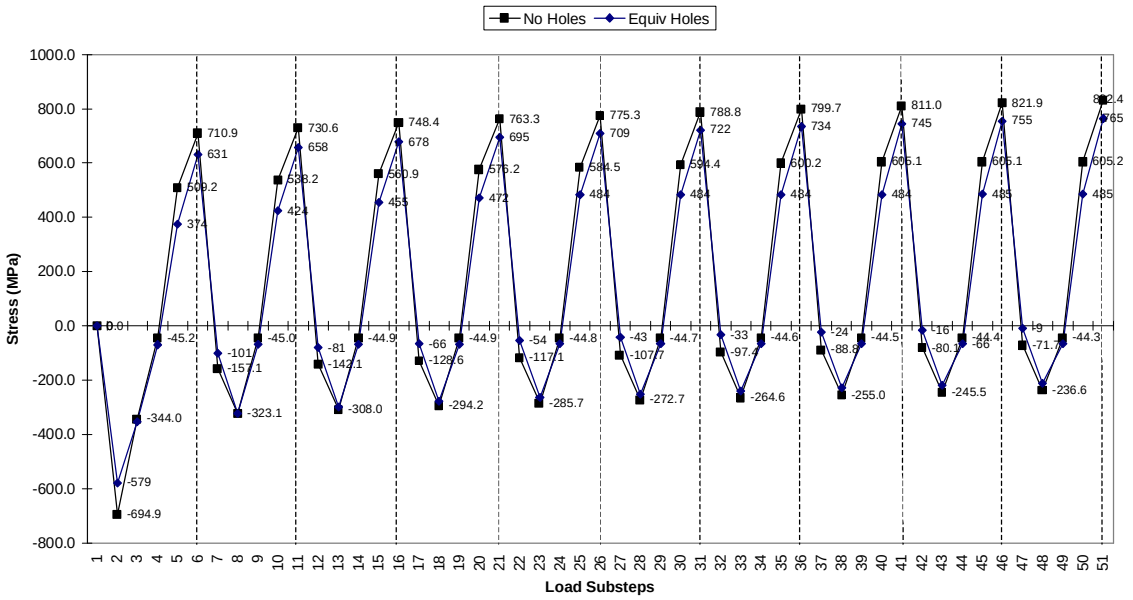

Figure B.2 Effective hole vs. non-holed response comparison showing the change in the top, center node stress of the model over ten cycles

While the effect of these holes over the entire response at the component level can be approximated with this current method, it would not be effective for modeling stress and constitutive response at the smaller (crack dimension) level. The loads and displacements needed for the response of the nodes surrounding the crack tip would have to be the virgin material properties for holes at the mm scale.

APPENDIX C: POTENTIAL FOR "COOLED LIP"

Another study that was investigated was that involving a "cooled lip" scenario for a combustor liner crack. With the advent of cracking in a hot spot in an actual liner, a potential for a second thermal gradient could exist within the hot spot itself. As has been discussed, the cooling holes in a combustor liner are named so because they pull bypass air that has not been heated into the inner liner wall to serve as a cooling film that help keeps the liner cooled. A possibility, then exists where a crack in the combustor liner could serve as an unintentional cooling hole, bringing in cooler air to the combustion side of the liner. And if this occurs in a hot spot crack, there would be a significant chance that the cooler air entering the center of the hot spot might create a cooler temperature gradient within the spot surrounding the crack. This cooler region around the crack, dubbed a "cool lip", could create a completely different stress field and mechanical response of a hot spot. The potential for this scenario was investigated.

During the thermal cycling of the cracked model when the crack length is 17.78 mm, the y-displacement (away from the x-z symmetry plane) of the crack face was monitored during a complete thermal cycle. A higher crack length is more likely to have the greatest crack face opening over a greater distance, and therefore the potential for cooling to occur would be highest. The data was recorded for two radial locations along the crack length (at the model and crack center and halfway along the crack length). At these two positions, three displacements were measured through the thickness, the top surface, bottom surface, and at the midplane. Figure C.1 shows an overall isometric view of where the y-displacements were recorded for a given model solution.

The displacements were recorded at the end of the 39th thermal cycle when the crack length was 17.145 mm and the blister was cooled. The crack face displacements are shown in Figure C.2 from a view along the x-z plane looking down at an angle for an "end view" of the crack face movements. Figure

C.2 shows that the crack (at a cooled down state) is open along the entire length, albeit to very small distances. The greatest opening is at the top, corresponding to the tensile side of bending.

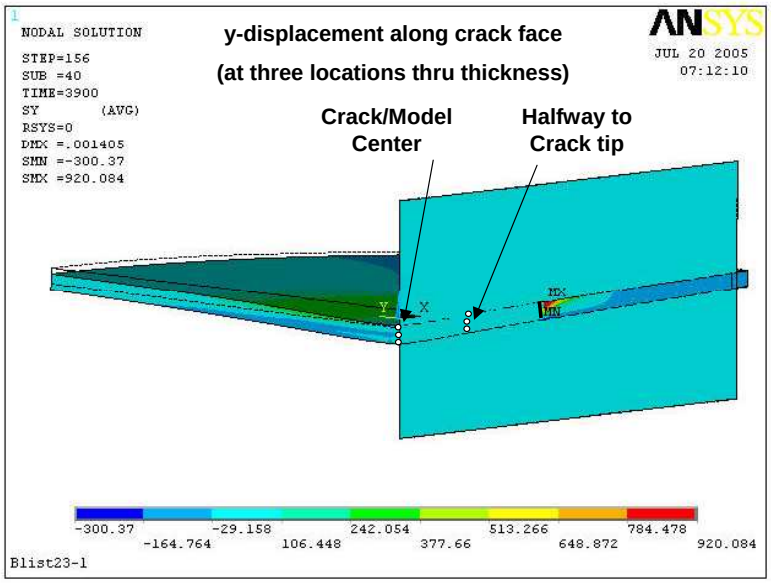

Figure C.1 Isometric view of a model solution of stress in the y-direction when the crack is 17.14 mm long, showing locations along the crack face where y-displacements are recorded.

Figure C.3 shows this same model in the middle of heat up as the model center moves down while the mesh tries to expand. The result along the crack front is that it is closed along the entire length (NOTE: when closed is noted, the actual nodal displacements from the symmetry plane are negative, but within .015 mm, which was the gauss point penetration tolerance given as a constant. A reasonable penetration tolerance is needed to ensure solution convergence). The end of heat up is shown in Figure C.4. The schematic and distances indicate that the crack face is open along the bottom but is closed along the top.

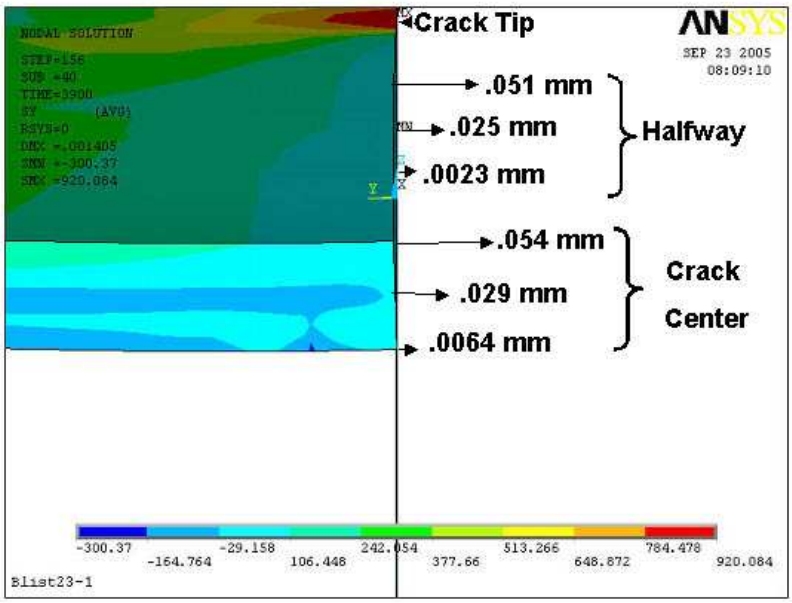

Figure C.2 View along x-z plane of a model solution of stress in the y-direction when the crack is 17.14 mm long at cool down. Crack face is open along the face with the greatest opening at the top.

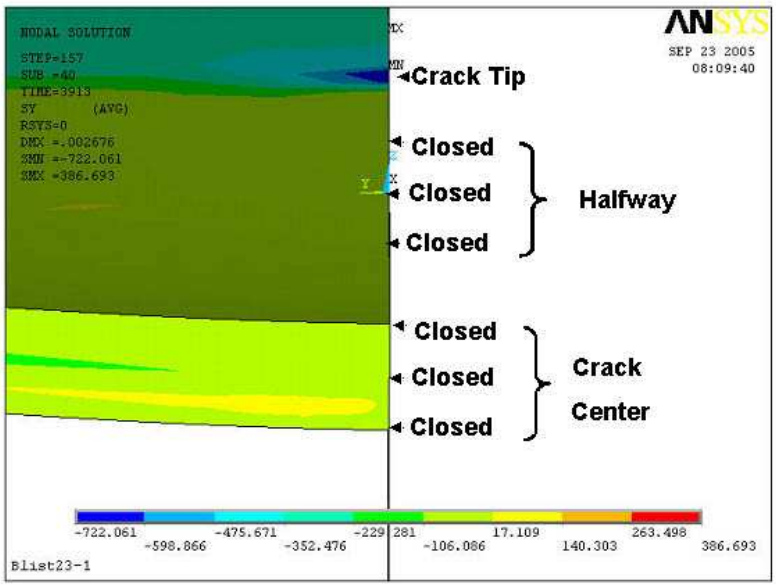

Figure C.3 View along x-z plane of a model solution of stress in the y-direction when the crack is 17.14 mm long during heat-up. Crack face is closed along entire length.

As C.5 and C.6 indicate, during and at the end of another cool down, respectively, the crack is only completely open at the end of cool down.

The fact that the crack is only open when temperatures are low is an extremely important point regarding the potential for these “cooled lips.” The only time that a cooled lip could occur is when the cooler air penetrates a liner crack when the hot spot and engine are at high temperature. However, as Figures C.3 – C.5 show, the crack is closed during these high temperature periods. Therefore, it would seem improbable, if not impossible, for a cooled lip scenario to occur.

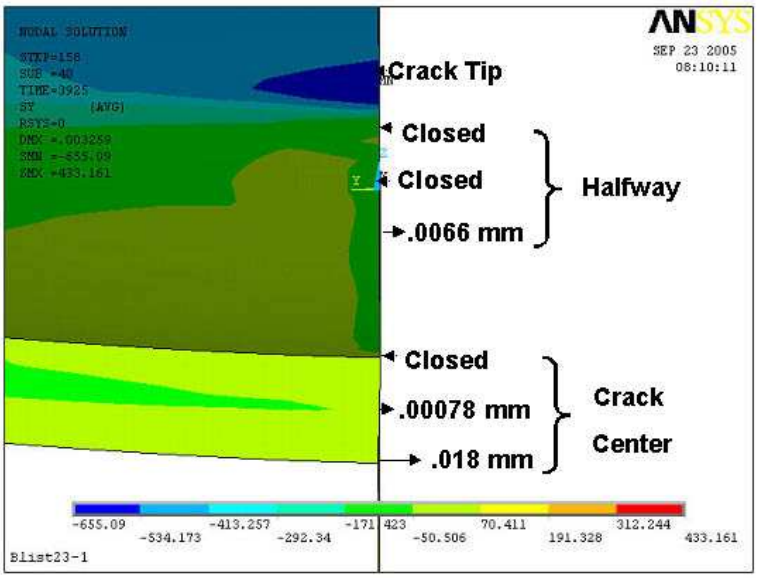

Figure C.4 View along x-z plane of a model solution of stress in the y-direction when the crack is 17.78 mm long at max heat-up. Crack face is open along the bottom and closed at the top.

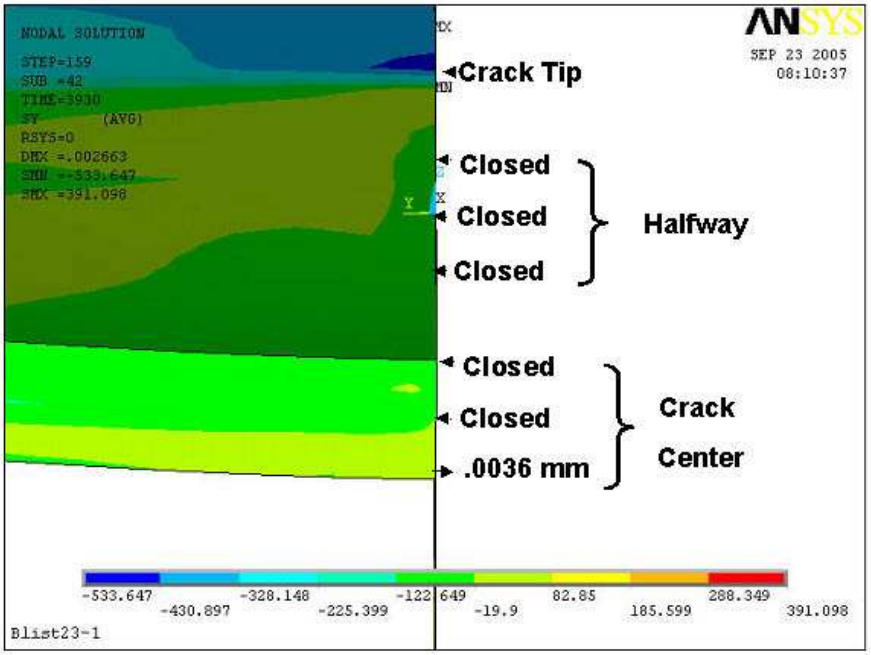

Figure C.5 View along x-z plane of a model solution of stress in the y-direction when the crack is 17.78 mm long during cool-down. Crack face is almost entirely closed

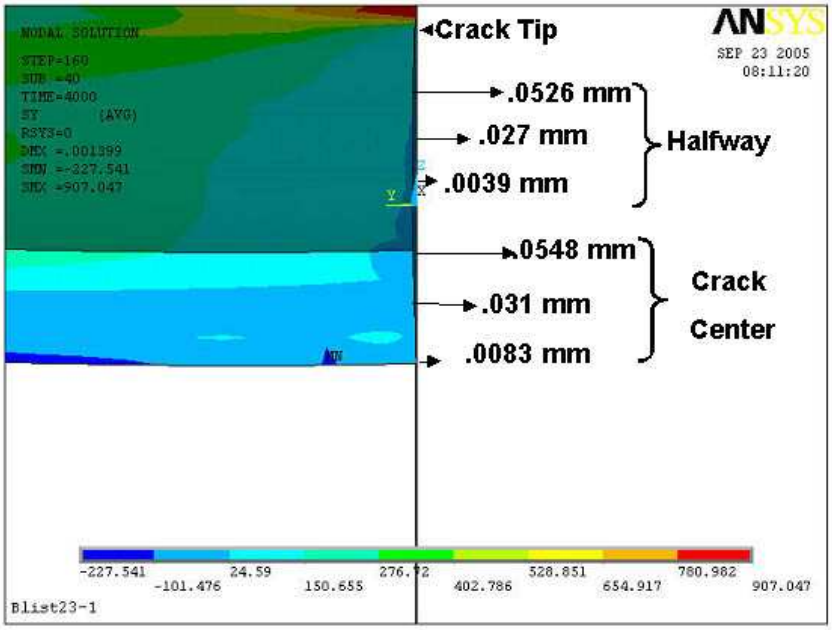

Figure C.6 View along x-z plane of a model solution of stress in the y-direction when the crack is 17.78 mm long at cool down. Crack face is open along the face with the greatest opening at the top.

As was seen in the post-test specimen inspection of the blister test, however, the crack front is not completely straight. On both the top and bottom surfaces, a somewhat jagged path at the thickness level is seen. As a result, the chance that the crack face is completely closed along its entire length is low. The irregular surfaces would prevent complete closure in some locations through the thickness, even at heat up. But these small regions, or pockets, of thru crack lengths would be far too small to permit substantial amounts of cooling air through the crack. Therefore, only small areas might experience this cooling effect. So it is most likely there could be very small “cold sores” on an otherwise “hot lip” that would not grossly effect the constitutive response of the hot spot.

REFERENCES

1. Basquin, O.H., "The Exponential Law of Endurance Tests". American Society for Testing and Material Processes, 1910. **10**: p. 625-630.

2. Coffin, L.F.J., "A Study of the Effects of Cyclic Thermal Stresses on a Ductile Metal". Transactions of the American Society of Mechanical Engineers, 1954. **76**.

3. Manson, S.S. "Behavior of Materials under Conditions of Thermal Stress". in *Heat Transfer Symposium*. 1953. University of Michigan Engnieering Research Institute.

4. Bannantine, J.A., Comer, J.J., and Handrock, J.L., *Fundamentals of Metal Fatigue Analysis*. 1990, Englewood Cliffs, NJ: Prentice-Hall.

5. Manson, S.S., Halford, G.R., Hirschberg, M.H. in *Symposium on Design for Elevated Temperature Analysis*. 1971: American Society of Mechanical Engineers.

6. Palmgren, A., "Durability of Ball Bearings". ZVDI, 1924. **68**(14): p. 339-341.

7. Miner, M.A., "Cumulative Damage in Fatigue". Transactions of the American Society of Mechanical Engineers, 1945. **67**: p. A159-164.

8. Ramberg, W., Osgood, W., "Description of Stress-Strain Curves by Three Parameters". NACA Tech. Note No. 902, 1943.

9. Hill, R., *The Mathematical Theory of Plasticity*. 1950, London: Oxford University Press. 24-25.

10. Bauschinger, J. (1886) "Mitt. Mech. Lab Munich (Yearly Report)". Munich.

11. Prager, W., "Recent Developments in the Mathematical Theory of Plasticity". Journal of Applied Physics, 1949. **20**: p. 235-241.

12. Khan, A.S., Huang, S., *Continuum Theory of Plasticity*. 1995, New York: Wiley-Interscience.

13. Dafalais, Y.F., Popov, E.P., "Plastic internal variables formalism of cyclic plasticity". Journal of Applied Mechanics, 1976. **98**(645).

14. Armstrong, P.J., Frederick, C.O., "A Mathematical Representation of the Multiaxial Bauschinger Effect". G.E.G.B. Report RD / B / N, 1966(731).

15. Lemaitre, J., Chaboche, J-L, *Mechanics of Solid Materials*. 1990, Cambridge, UK: Cambridge University Press.

16. Valanis, K.E., "A Theory of Viscoplasticity without a Yield Surface". Arch. Mech., 1971. **23**(517).

17. Watanabe, O., Atluri, S.N., "Internal Time, General Internal Variable, and Multiyield-Surface Theories of Plasticity and Creep: A Unification of Concepts". International Journal of Plasticity, 1986. **2**(37).

18. Duhamel, J.M.C., Memoires de l'Institut de France, 1838. **5**: p. 440.

19. Winkelmann, A.S., O., Annalen der Physikalischen Chemie, 1894. **51**: p. 730.

20. Schmid, E., Boas, W. "Kristallplastizitaet". in *Verlag Julius Springer*. 1935. Berlin.

21. Bollenrath, F.C., H., and Bungardt, W., Jahrbuch der Deutschen Luftfahrforschung, 1938. **II**: p. 326-338.

22. Millenson, M.B., Manson, S.S., "Investigation of Rim Cracking in Turbine Wheels with Welded Blades". 1947.

23. Sehitoglu, H., "Material Behavior under Thermal Loading". Journal of Pressure Vessel Technology, Transactions of ASME, 1986. **108**(1): p. 113-119.

24. Neu, R.W., Sehitoglu, H., "Thermomechanical Fatigue, Oxidation, and Creep, Part 1. Damage Mechanisms". Metallurgical Transactions, 1989. **20A**(9): p. 1755-1767.

25. Remy, L., Bernard, H., Malpertu, J.L., and Rezai-Aria, R., ed. "Fatigue Life Prediction Under Thermomechanical Loading in a Nickel-Based Superalloy". Thermomechanical Fatigue Behavior of Materials, ASTM STP 1186, ed. H. Sehitoglu. 1993, American Society for Testing and Materials: Philadelphia. 3-16.

26. Marchand, N.J., L'Esperance, and Pelloux, R.M., ed. "Thermal-Mechanical Cyclic Stress-Strain Responses of Cast B-1900+Hf". Low Cycle Fatigue, ASTM STP 942, ed. H.D. Solomon. 1988, American Society for Testing and Materials: Philadelphia. 638-656.

27. Glenny, E., "A Technique for Thermal-Shock and Thermal Fatigue Testing Based on the use of Fluidized Solids". Joural for the Institute of Metals, 1958. **84**: p. 294.

28. Glenny, E. (1967) "Thermal and High Strain Fatigue". The Institute of Metals,

29. Rezai Aria, F., Francois, M., and Remy, L., "Thermal Fatigue of MAR-M509 Superalloy. I) The Influence of Specimen Geometery on the Thermal Fatigue Behaviour". Fatigue and Fracture of Engineering Materials, 1988. **11**: p. 277-289.

30. Rezai Aria, F., Dambrine, B., and Remy, L., "Thermal Fatigue of MAR-M509 Superalloy. II) Evolution and Life Prediction Models". Fatigue and Fracture of Engineering Materials, 1988. **11**: p. 291-302.

31. Engler-Pinto, C.C., "Etude de l'endommagement en fatigue thermo-mecanique de superalliages a base de nickel". 1996, Ecole Polytechnique Federale de Lausanne: Lausanne, France.

32. Meyer-Olbersleben, F., Engler-Pinto, C.C., and Rezai Aria, F., ed. "On Thermal Fatigue of Nickel-Based Superalloys". ASTM 1263. 1996, American Society for Testing and Materials. 41-55.

33. Ahuja, V., Jahedi, M.Z. "Heat Checking--A Comparison of Five Hot Work Tool Steels for Use in High Pressure Die Casting Dies". in *21st International Die Casting Congress and Exhibition*. 2001: North American Die Asssociation.

34. Jean, S., Miquel, B., Leroux, S., and Rezai Aria, F. "An Investigation on Heat Checking of Hot Work Tool Steels". in *5th International Tooling Conference*. 1999.

35. Suzuki, T., Ishihara, M. and Miyachi, H. "Residual Stress and Heat Checking in Die Casting Dies". in *Transactions of the 7th SDCE International Die Casting Congress*. 1972.

36. Prabu, M.S.S., Durvasula, S., "Thermal Buckling of Skew Plates". Canadian Aeronautics and Space Journal, 1974. **20**: p. 111-113.

37. Kanaka Raju, K., Venkateswara Rao, G, "Thermal-postbuckling of Circular Plates". Computers and Structures, 1984. **18**: p. 1179-1182.

38. Tani, J., "Thermal Buckling of an Annular Plate with Axisymetric Initial Deflection". Journal of Applied Mechanics, 1978. **45**: p. 693-695.

39. Tani, J., "Elastic Instability of a Heated Annular Plate Under Lateral Pressure". Journal of Applied Mechanics, 1981. **1981**: p. 399-403.

40. Morjaria, M., Mukherjee, S., "Finite element analysis of time-dependent inelastic deformation in the presence of thermal stresses". International Journal for Numerical Methods in Engineering, 1981. **17**: p. 909-921.

41. Providakis, C.P., Kourtakis, S.G., "Viscoplastic BEM Analysis of Creeping Metallic Structural Components in the Presence of Temperature Gradients". International Journal of Pressure Vessels and Piping, 2002. **79**: p. 309-317.

42. Law, M., Payten, W., Snowden, K., "Modelling creep of pressure vessels with thermal gradients using Theta projection data". International Journal of Pressure Vessels and Piping, 2002. **79**: p. 847-851.

43. Kim, J., Choi, J., Kim, Y., and Park, Y., "Investigation on constraint effect of reactor pressure vessel under pressurized thermal shock". Nuclear Engineering and Design, 2002. **219**: p. 197-206.

44. Inglis, C.E., "Stresses in a Plate Due to the Pressence of Cracks and Sharp Corners". Transactions of the Institute of Naval Architects, 1913. **55**: p. 219-241.

45. Griffith, A.A., "The Phenomena of Rupture and Flow in Solids". Philosophical Transactions, Series A, 1920. **221**: p. 163-198.

46. Irwin, G.R., *Fracture Dynamics*. Fracturing of Metals, American Society for Metals. 1948, Cleveland. 147-166.

47. Orowan, E., "Fracture and Strength of Solids". Reports on Progress in Physics, 1948. **XII**: p. 185-232.

48. Westergaard, H.M., "Bearing Pressures and Cracks". Journal of Applied Mechanics, 1939. **6**: p. 49-53.

49. Dugdale, D.S., "Yielding in Steel Sheets Containing Slits". Journal of Mechanics of Physical Solids, 1961. **8**: p. 100-104.

50. Paris, P.C., Gomez, M.P., and Anderson, W.P., "A Rational Analytic Theory of Fatigue". The Trend in Engineering, 1961. **13**: p. 9-14.

51. Hertzberg, R.W., *Deformation and Fracture Mechanics of Engineering Materials*. 3rd ed. 1989, New York: Wiley.

52. Forman, R.G., Kearney, V.E., and Engle, R.M., "Numerical Analysis of Crack Propagation in a Cyclic-Loaded Structure". Journal of Basic Engineering, Transactions of the ASME, 1967. **D89**(3): p. 459-464.

53. Walker, K., *The Effect of Stress Ratio During Crack Propagation and Fatigue for 2024-T3 and 7075-T6 Aluminum*. Effects of Environment and Complex Load History on Fatigue Life, ASTM STP 462. 1970, Philadelphia, Pa: American Society for Testing and Materials. 1-14.

54. Elber, W., "Fatigue Crack Closure under Cyclic Tension". Engineering Fracture Mechanics, 1970. **2**: p. 37-45.

55. Elber, W., *The Significance of Fatigue Crack Closure*. Damage Tolerance in Aircraft Structures, ASTM STP 486. 1971, Philadelphia, PA: American Society for Testing and Materials. 230-242.

56. Rau, C.A., Jr., Gemma, E.A., and Leverant, G.R., ed. "Thermal-Mechanical Fatigue Crack Propogation in Nickel- and Cobalt-Base Superalloys Under Various Strain-Temperature Cycles". Fatigue at Elevated Temperatures, ASTM STP 520, ed. A.E. Carden. 1973, American Society for Testing and Materials: Philadelphia.

57. Gemma, A.E., Ashland, F.X., and Masci, R.M., "The Effects of Stress Dwells and Varying Mean Strain on Crack Growth During Thermal Mechanical Fatigue". Journal of Testing and Evaluation, 1981. **9**(4): p. 209-215.

58. Rice, J.R., "A Path Independant Integral and Approximate Analysis of Strain Concentration by Notches and Cracks". Journal of Applied Mechanics, 1968. **35**: p. 379-386.

59. Hutchinson, J.W., "Singular Behavior at the End of a Tensile Crack Tip in a Hardening Material". Journal of Mechanics of Physical Solids, 1968. **16**: p. 13-21.

60. Rice, J.R., Rosengren, G.F., "Plane Strain Deformation near a Crack Tip in a Power Law Hardening Material". Journal of Mechanics of Physical Solids, 1968. **16**: p. 1-12.

61. Dowling, N.E., Begley, J.A., ed. "Fatigue Crack Growth during Gross Plasticity and the J-Integral". Mechanics of Crack Growth, ASTM STP 590. 1976, American Society for Testing and Materials: Philadelphia. 82-103.

62. Dover, W.D., "Fatigue Crack Growth under C.O.D. Cycling". Engineering Fracture Mechanics, 1973. **5**: p. 11-21.

63. McEvily, A.J., Beukelmann, D., and Tanaka, K. "On Large-Scale Plasticity Effects in Fatigue Crack Propogation". in *Mechanical Behavior of Materials: Proceedings of teh 1974 Symposium on Mechanical Behavior of Materials*. 1974. Kyoto, Japan: Society of Material Science.

64. Shih, C.F., "Relationships between the J-Integral and the Crack Opening Displacement for Stationary and Extending Cracks". Journal of Mechanics of Physical Solids, 1981. **29**(4): p. 305-326.

65. Skelton, R.P., "The Prediction of Crack Growth Rates from Total Endurances in High Strain Fatigue". Fatigue of Engineering Materials and Structures, 1979. **2**: p. 305.

66. Wareing, J., "Creep-Fatigue Interaction in Austenitic Stainless Steels". Metallurgical Transactions, 1977. **8A**: p. 711-721.

67. Landes, J.D., Begley, J.A., *A Fracture Mechanics Approach to Creep Crack Growth*. Mechanics of Crack Growth, ASTM STP 590. 1976, Philadelphia, Pa: American Society for Testing and Materials. 128-148.

68. Saxena, A. "Evaluation of C* for Characterization of Creep Crack Growth Behavior of 304 Stainless-Steel". in *12th Fracture Conference Proceedings, ASTM STP 590*. 1980. Philadelphia: American Society for Testing and Materials.

69. Blackburn, W.S., "Path-Independent Integrals to Predict the Onset of Crack Instability in an Elastic Material". International Journal of Fracture Mechanics, 1972. **8**: p. 343-346.

70. Kishimoto, K., Aoki, S., and Sakada, M., "On the Path-Independant Integral--J^". Engineering Fracture Mechanics, 1980. **13**: p. 841-850.

71. Orange, T.W., "Elevated Temperature Crack Propogation". Fatigue and Fracture of Aerospace Structural Materials, ASME, 1993. **36**: p. 177-188.

72. Atluri, S.N., Nishioka, T., and Nakagaki, M. (1983) "Incremental Path-Independent Integrals in Inelastic and Dynamic Fracture Mechanics". Georgia Institute of Technology, Atlanta, GA. GIT-CACM-SNA-83-27

73. Kim, K.S., Van Stone, R.H., "Hold Time Crack Growth Analysis at Elevated Temperatures". Engineering Fracture Mechanics, 1995. **52**: p. 433-444.

74. Kim, K.S., Van Stone, R.H., "Crack Growth Under Thermomechanical and Temperature Gradient Loads". Engineering Fracture Mechanics, 1997. **58**: p. 133-147.

75. ANSYS version 7.1, 2003, ANSYS, Inc..

76. Rybicki, E.F., Kanninen, M.F., "A Finite Element Calculation of Stress Intensity Factors by a Modified Crack Closure Integral". Engineering Fracture Mechanics, 1977. **9**: p. 931-938.

77. Byskov, E., "The Calculation of Stress Intensities Using the Finite-Element Method". International Journal of Fracture Mechanics, 1970. **6**(2): p. 159-167.

78. Benzley, S.E., "Representation of Singularities with Isoparametric Finite Element". International Journal for Numerical Methods in Engineering, 1974. **8**: p. 537-545.

79. Jordan, S., Padlog, J., Hopper, A.T., Rybicki, E.F., Hulbert, L.E., and Kanninen, M.F. (1973) "Development and Application of Improved Analytical Techniques for Fracture Analysis Using MAGIC-III". Air Force Flight Dynamics Laboratory, Wright-Patterson AFB, OH. AFFDL-TR-73-61

80. Irwin, G.R., "Fracture". Handbuch der Physik, 1958. **6**: p. 551.

81. Gallagher, R.H. "Survey and Evaluation of the Finite Element in Linear Fracture Mechanics Analysis". in *Conference on Structural Mechanics Reactor Technology*. 1971. Berlin.

82. Rice, J.R., Tracey, D.M., *Computational Fracture Mechanics*. Numerical and Computer Methods in Structural Mechanics. 1973, New York: Academic Press.

83. Jerram, K., Hellen, T.K. "Finite Element Techniques in Fracture Mechanics". in *International Conference in Welding Research*. 1972. Southampton.

84. Hellen, T.K., "On the Method of Virtual Crack Extensions". International Journal for Numerical Methods in Engineering, 1975. **9**: p. 187-207.

85. Parks, D.M., "A Stiffness Derivative Finite Element Technique for Determination of Crack Tip Stress Intensity Factors". International Journal of Fracture, 1974. **10**(4): p. 487-502.

86. Parks, D.M., "The Virtual Crack Extension Method for Nonlinear Material Behavior". Computer Methods in Applied Mechanics and Engineering, 1977. **12**: p. 353-364.

87. Singh, R., Carter, B.J., Wawrzynek, P.A., and Ingraffea, A.R., "Universal Crack Closure Integral for SIF Estimation". Engineering Fracture Mechanics, 1998. **60**(2): p. 133-146.

88. Singh, R., Patel, S.K., and Dattaguru, B., "Decomposed Crack Closure Integrals for Estimation of SIF Variations". Engineering Fracture Mechanics, 1999. **63**: p. 165-178.

89. Sehitoglu, H., "Crack Opening and Closure in Fatigue". Engineering Fracture Mechanics, 1985. **21**(2): p. 329-339.

90. Newman, J.C.J., Booth, B.C., and Shivakumar, K.N., ed. "An Elastic-Plastic Finite-Element Analysis of the J-Resistance Curve Using a CTOD Criterion". Fracture Mechanics: 18th Symposium, ASTM STP 945, ed. D.T. Read. 1988: Philadelphia.

91. Newman, J.C.J., Dawicke, D.S., Sutton, M.A., and Bigelow, C.A. "A Fracture Criterion For Wide Spread Cracking in Thin Sheet Aluminum Alloys". in *17th International Committee on Aeronautical Fatigue*. 1993. Stockholm, Sweden.

92. Carpenter, W.C., Read, D.T., and Dodds, R.H., Jr, "Comparison of Several Path-Independent Integrals Including Plasticity Effects". International Journal of Fracture, 1986. **31**(4): p. 303-323.

93. Wellman, G.W., Rolfe, S.T., and Dodds, R.H., Jr. "Three-Dimensional Elastic-Plastic Finite Element Analysis of Three-Point Bend Specimens". in *Fracture Mechanics: Sixteenth Symposium, ASTM STP 868*. 1985. Philadelphia: American Society for Testing and Materials.

94. Dodds, R.H., Jr., Carpenter, W.C., and Sorem, W.A., "Numerical Evaluation of a 3-D J-Integral and Comparison with Experimental Results for a 3-point Bend Specimen". Engineering Fracture Mechanics, 1988. **29**(3): p. 275-285.

95. Sorem, W.A., Rolfe, S.T., and Dodds, R.H., Jr. (1990) "Effects of Crack Depth on Elastic-Plastic CTOD Fracture Toughness". Welding Research Council Bulletin,

96. Dodds, R.H., Jr., Read, D.T., "Experimental and Numerical Studies of the J-Integral for a Surface Flaw". International Journal of Fracture, 1990. **43**(1): p. 47-67.

97. Dodds, R.H., Jr., Anderson, T.L., and Kirk, M.L., "A Framework to Correlate a/W Ratio Effects on Elastic-Plastic Fracture Toughness, J_c". International Journal of Fracture, 1991. **48**(1): p. 1-22.

98. Gallerud, A.S., Dodds, R.H., Jr., Hampton, R.W., and Dawicke, D.S., "Three-Dimensional Modeling of Ductile Crack Growth in Thin Sheet Metals: Computational Aspects and Validation". Engineering Fracture Mechanics, 1999. **63**: p. 347-374.

99. Cahn, R.W., Evans A.G., and McLean, M., *High-temperature Structural Materials*. 1996: Chapman & Hall. 1.

100. 10th Ed. ed. Metals Handbook, ed. A.I.H. Committee. Vol. 1. 1990, ASM International: Materials Park, OH.

101. Bodner, S.R., Chan, K.S., "Modeling of Continuum Damage for Application in Elastic-Vistoplastic Constitutive Equations". Engineering Fracture Mechanics, 1986. **25**: p. 705-712.

102. Chan, K.S., Bodner, S.R., Walker, K.P., and Lindholm, U.S. "A Survey of Unified Constitutive Theories". in *Proceedings of Second Symposium on Nonlinear Constitutive Relations for High Temperature Applications*. 1984. Cleveland, OH.

103. Chan, K.S., Lindholm, U.S., and Bodner, S.R. (1988) "Constitutive Modeling for Isotropic Materials". Southwest Research Institute, San Antonio, TX. SwRI Project No. 06-7576

104. Chan, K.S., Bodner, S.R., and Lindholm, U.S., "Phenomenological Modeling of Hardening and Thermal Recovery in Metals". Journal of Engineering Materials and Technology, 1988. **110**: p. 1-8.

105. Chan, K.S., Page, R.A., "Inelastic Deformation and Dislocation Structure of Nickel Alloy: Effects of Deformation and Thermal Histories". Metallurgical Transactions A, 1988. **19A**: p. 2477-2486.

106. Chan, K.S., Lindholm, U.S., Bodner, S.R., and Walker, K.P., "High Temperature Inelastic Deformation Under Uniaxial Loading: Theory and Experiment". Journal of Engineering Materials and Technology, 1989. **111**: p. 345-353.

107. Chan, K.S., Lindholm, U.S., Bodner, S.R., and Nagy, A., "High Temperature Inelastic Deformation of the B-1900+Hf Alloy Under Multiaxial Loading: Theory and Experiment". Journal of Engineering Materials and Technology, 1990. **112**: p. 7-14.

108. Moreno, V., Nissley, D.M., and Lin, L.S. (1984) "Creep Fatigue Life Prediction For Engine Hot Section Materials (Isotropic), 2nd. Annual Report". NASA Lewis Research Center, Cleveland. NASA CR-174844

109. Whittenberger, J.D., "Elevated Temperature Mechanical Properties and Residual Tensile Properties of Two Cast Superalloys and Several Nickel-base Oxide Dispersion Strengthened Alloys". Metallurgical Transactions A, 1981. **12A**(2): p. 193-206.

110. Whittenberger, J.D. (1981) "Creep and Residual Mechanical Properties of Cast Superalloys and Oxide Dispersion Strengthened Alloys". NASA Lewis Research Center, Cleveland. NASA TP 1781

111. Bird, J.E., Mukherjee, A.K., and Dorn, J.E., "A Qualitative Relation Between Properties and Microstructure". Israel University Press, 1969: p. 255.

112. Norton, F.H., *The Creep of Steel at High Temperature*. 1929, New York: McGraw-Hill.

113. Almroth, P., Hasselqvist, M., Simonsson, K., and Sjostrom, S., "Viscoplastic-plastic modeling of IN792". Computational Materials Science, 2004. **29**: p. 437-445.

114. Sinha, N.K., "Power-Law Breakdown--An Examination Using Strain Relaxation and Recovery Tests on a Nickel-Base Superalloy, IN-738LC". Journal of Materials Science Letters, 2002. **21**: p. 871-875.

115. Marchand, N.J., Pelloux, R.M., "High Strain Fatigue Crack Growth in Nickel-base Alloys". Res Mechanica, 1989. **27**: p. 285-308.

116. Wellman, G.W., Rolfe, S.T., *Three-Dimensional Elastic-Plastic Finite Element Analysis of Three-Point Bend Specimens*. Welding Research Council Bulletin 299. Vol. Part I. 1984. 15-25.

117. Uragami, K., Nakamura, K., and Asada, K., "Inelastic Analysis of Perforated Plates Using Equivalent Solid Plates". Transactions of the International Conference on Structural Mechanics in Reactor Technology, 1981: p. 1-9.

118. Nakamura, K., Takenaka, M., and Muto, T., "Inelastic Behavior of Perforated Plates Subjected to Bending". Transactions of the International Conference on Structural Mechanics in Reactor Technology, 1983: p. 607-615.

VITA

Donald W. Rhymer

Donald William Rhymer was born in Columbus, OH, to the son of Peter James and Donna Sue Rhymer. He attended public schools throughout the United States until his father retired from the U.S. Air Force as a Major and settled his family in Vienna, WV. Following graduation from Parkersburg H.S., Don attended the U.S. Air Force Academy where he received his B.S. in Engineering Mechanics and commission as a 2Lt in 1995. Most importantly he met Jesus Christ and then Dawn Grover, class of 1997, there. After a three-year assignment as an engineer at the National Air Intelligence Center at Wright-Patterson AFB, OH, he was blessed with the opportunity to pursue a path of academia within the Air Force, as he was sponsored for full-time graduate study at Georgia Tech under Dr. Steve Johnson. After receiving his M.S. in Mechanical Engineering in 1999, Don fulfilled a calling to teach by instructing back at the Academy in the Department of Engineering Mechanics. During his assignment, the Lord confirmed his call to the classroom and as well as blossomed his friendship with Dawn into marriage in July 2000. Donald will return to WPAFB return to with an assignment to the Propulsion Directorate at the A.F. Research Laboratory. Aside from the degree, the Lord has blessed him during his Georgia Tech stay with a promotion to Major and two lovely children. Following the AFRL assignment, Don is in the pipeline to teach, once again, at the Academy.